# SMIP05

SMIP05 SEMINAR ON
UTILIZATION OF STRONG-MOTION DATA

Los Angeles, California
May 10, 2005

PROCEEDINGS

Edited by

Moh Huang

Sponsored by

California Strong Motion Instrumentation Program
California Geological Survey
California Department of Conservation

Co-Sponsors

California Seismic Safety Commission
California Office of Emergency Services
California Department of Transportation
Office of Statewide Health Planning and Development

# PREFACE

The California Strong Motion Instrumentation Program (CSMIP) in the California Geological Survey (previously known as the Division of Mines and Geology) of the California Department of Conservation established a Data Interpretation Project in 1989. Each year the CSMIP funds several data interpretation contracts for the analysis and utilization of strong-motion data. The primary objectives of the Data Interpretation Project are to further the understanding of strong ground shaking and the response of structures, and to increase the utilization of strong-motion data in improving post-earthquake response, seismic code provisions and design practices.

As part of the Data Interpretation Project, CSMIP holds annual seminars to transfer recent research findings on strong-motion data to practicing seismic design professionals, earth scientists and post-earthquake response personnel. The purpose of the annual seminar is to provide information that will be useful immediately in seismic design practice and post-earthquake response, and in the longer term, in the improvement of seismic design codes and practices. The SMIP05 Seminar is the sixteenth in this series of annual seminars.

The SMIP05 Seminar is divided into four sessions. Session I includes strong-motion data from the 2004 Parkfield earthquake and animation of earthquake ground motions. Session II will include ShakeMap uncertainty and visualization of the seismic response of an interchange bridge. Session III will include two presentations on various methodologies for post-earthquake damage assessment of instrumented buildings using recorded building response data. In Session IV, there are four invited presentations on the ground motions of the recent Sumatra earthquakes, engineering aspects of the Sumatra mainshock, and tsunami preparedness and response in California. The Seminar will end with a field trip to the Los Angeles City Hall. Before the field trip, Nabih Youssef will discuss the design and new structural system for strengthening the Los Angeles City Hall. CSMIP extends its appreciation to staff of the City of Los Angeles, especially Jim Treadaway and Y.C. Wang, who have cooperated in the installation of strong-motion equipment in the City Hall.

The seminar includes presentations by investigators of four CMIP-funded projects. These four projects are scheduled to be completed by the summer 2005 and the final results will be published in their final reports.

Moh J. Huang
Data Interpretation Project Manager

# Members of the Strong Motion Instrumentation Advisory Committee

**Main Committee**

Chris Poland, Chair, Degenkolb Engineers
Bruce Bolt, UC Berkeley
Anil Chopra, UC Berkeley
Bruce Clark, Seismic Safety Commission, Leighton & Associates
C. Allin Cornell, Stanford University
Wilfred Iwan, California Institute of Technology
Jerve Jones, Jones & Jones
Michael Keever, Caltrans
Vern Persson, DWR Division of Safety of Dams (retired)
Daniel Shapiro, Seismic Safety Commission, SOHA Engineers
Edward Bortugno (ex-officio), Office of Emergency Services
Robert Anderson (ex-officio), Seismic Safety Commission

**Ground Response Subcommittee**

Bruce Bolt, Chair, UC Berkeley
Yousef Bozorgnia, Pacific Earthquake Engineering Research Center
Brian Chiou, Caltrans
Marshall Lew, Law/Crandall
Geoffrey Martin, Univ. of Southern California
Maurice Power, Geomatrix Consultants

**Buildings Subcommittee**

Chris Poland, Chair, Degenkolb Engineers
Kenneth Honda, URS Corporation
Donald Jephcott, Structural Engineer
Jerve Jones, Jones & Jones
Jack Meehan, Structural Engineer
Farzad Naeim, John A. Martin & Associates
John Robb, Structural Engineer
Daniel Shapiro, SOHA Engineers
Chia-Ming Uang, UC San Diego

**Lifelines Subcommittee**

Vern Persson, Chair, DWR Division of Safety of Dams (retired)
Martin Eskijian, California State Lands Commission
David Gutierrez, DWR Division of Safety of Dams
Michael Keever, Caltrans Division of Engineering Services
LeVal Lund, Civil Engineer
Edward Matsuda, BART

**Data Utilization Subcommittee**

Wilfred Iwan, Chair, California Institute of Technology
Representatives from each Subcommittee

# TABLE OF CONTENTS

# SMIP05 SEMINAR ON UTILIZATION OF STRONG-MOTION DATA

Omni Hotel, Los Angeles, California
May 10, 2005

**FINAL PROGRAM**

8:00 am **REGISTRATION**

9:00 am **WELCOMING REMARKS**
*Chris Poland,* Chair, Strong Motion Instrumentation Advisory Committee (SMIAC)
*John Parrish,* State Geologist, California Geological Survey
*Anthony Shakal,* Program Manager, Strong Motion Instrumentation Program

**INTRODUCTION**
*Moh Huang,* Strong Motion Instrumentation Program

## *SESSION I*

Moderator: *Bruce Bolt,* UC Berkeley, SMIAC

9:15 am **Strong-Motion Data from the M6.0 Parkfield Earthquake of September 28, 2004**
*Anthony Shakal,* Vladimir Graizer, Moh Huang, Hamid Haddadi and Kuo-wan Lin, CSMIP

9:40 am **Animation of Ground Shaking for California Earthquakes**
*Timothy Mote* and John Egan, Geomatrix Consultants

10:05 am **Questions and Answers for Session I**

10:15 am Break

## *SESSION II*

Moderator: *Vern Persson,* SMIAC

10:35 am **Quantifying CISN ShakeMap Uncertainty**
*Kuo-wan Lin,* CSMIP, David Wald, Bruce Worden, U.S. Geological Survey, and Anthony Shakal, CSMIP

11:00 am **Visualization of Nonlinear Seismic Behavior of the Interstate 5/14 North Connector Bridge**
*Robert Dowell,* San Diego State University

11:25 am **Questions and Answers for Session II**

11:35 am **LUNCH**

## *SESSION III*

Moderator: *Chris Poland*, Degenkolb Engineers, SMIAC

12:45 pm **Automated Post-Earthquake Damage Assessment and Safety Evaluation of Instrumented Buildings**
*Farzad Naeim*, Scott Hagie, Arzhang Alimoradi, John A. Martin & Associates
and Eduardo Miranda, Stanford University

1:10 pm **A Data Driven Methodology for Assessing Impact of Earthquakes on the Health of Building Structural Systems**
*Dionisio Bernal*, and Eric Hernandez, Northeastern University

1:35 pm **Questions and Answers for Session III**

1:45 pm Break

## *SESSION IV*

Moderator: *Michael Keever*, Caltrans, SMIAC

2:00 pm **Ground Motions of the Sumatra Earthquakes of 2004 and 2005**
*Paul Somerville*, Hong Thio and Gene Ichinose, URS Corporation

2:10 pm **Engineering Aspects of the Indonesia Earthquake and Tsunami**
*Martin Johnson*, ABS Consulting

2:25 pm **State Role in Tsunami Preparedness and Response**
*Richard Eisner*, Governor's Office of Emergency Services

2:45 pm **Possible Local Tsunami Sources Impacting California**
*Mike Reichle* and Don Hoirup, California Geological Survey

2:55 pm **Questions and Answers for Session IV**

3:05 pm **Seismic Retrofit and Instrumentation of Los Angeles City Hall**
*Nabih Youssef* and Owen Hata, Nabih Youssef & Associates

3:25 pm Field Trip to **Los Angeles City Hall**

# STRONG-MOTION DATA FROM THE M6.0 PARKFIELD EARTHQUAKE OF SEPTEMBER 28, 2004

Anthony Shakal, Vladimir Graizer, Moh Huang,
Hamid Haddadi and Kuo-wan Lin

California Strong Motion Instrumentation Program
California Geological Survey, Sacramento, CA

## Abstract

The M6.0 Parkfield earthquake of September 28, 2004 that occurred on the San Andreas fault near the town of Parkfield in central California produced the most extensive and dense set of near-fault strong motion recordings ever obtained in California. As a result of a widely accepted likelihood of an earthquake in the area, a large number of strong motion stations had been deployed in the area. The arrays and the resultant strong-motion measurements of the earthquake, as well as preliminary observations are described here. The data includes very high variability in the near fault motion and accelerations as high as 2.5g.

## Introduction

The Parkfield earthquake occurred along the same segment of the San Andreas fault that ruptured during the 1966 Parkfield earthquake, resulting in a unique set of strong motion measurements by arrays specifically designed to record an event on this fault segment. The data and arrays are described more comprehensively in Shakal et al. (2005), and more general seismological results are described in Langbein et al. (2005).

A total of 56 three-component strong-motion recordings of acceleration were obtained within 20 km of the fault, with 49 of these being within 10 km of the fault. The strong motion measurements in the near fault region are highly varied, with significant variations occurring over relatively short distances. A map of near fault peak acceleration (Figure 1) shows striking variations over only a few km. The map also shows concentrations of strong shaking at both ends of the fault.

Peak accelerations in the near fault region range from 0.13 g to over 2.5 g (perhaps the highest acceleration recorded to date). The largest acceleration occurred near the northwest end of the inferred rupture zone, consistent with a model in which the strongest asperities on the fault occurred along this segment of the fault. These motions are consistent with directivity due to a fault rupturing from the hypocenter near Gold Hill to the northwest. However, accelerations up to 0.8g were also observed at the south end of the Cholame Valley near Hwy 46. These values are consistent with bilateral rupture to the southeast of the hypocenter, as included in the source modeling of Liu et al. (2005). The town of Parkfield itself had relatively low ground acceleration, only a fraction of that at stations within 2 km. However, the ground displacement at Parkfield was not small, dominated by periods between 0.6 and 1 second.

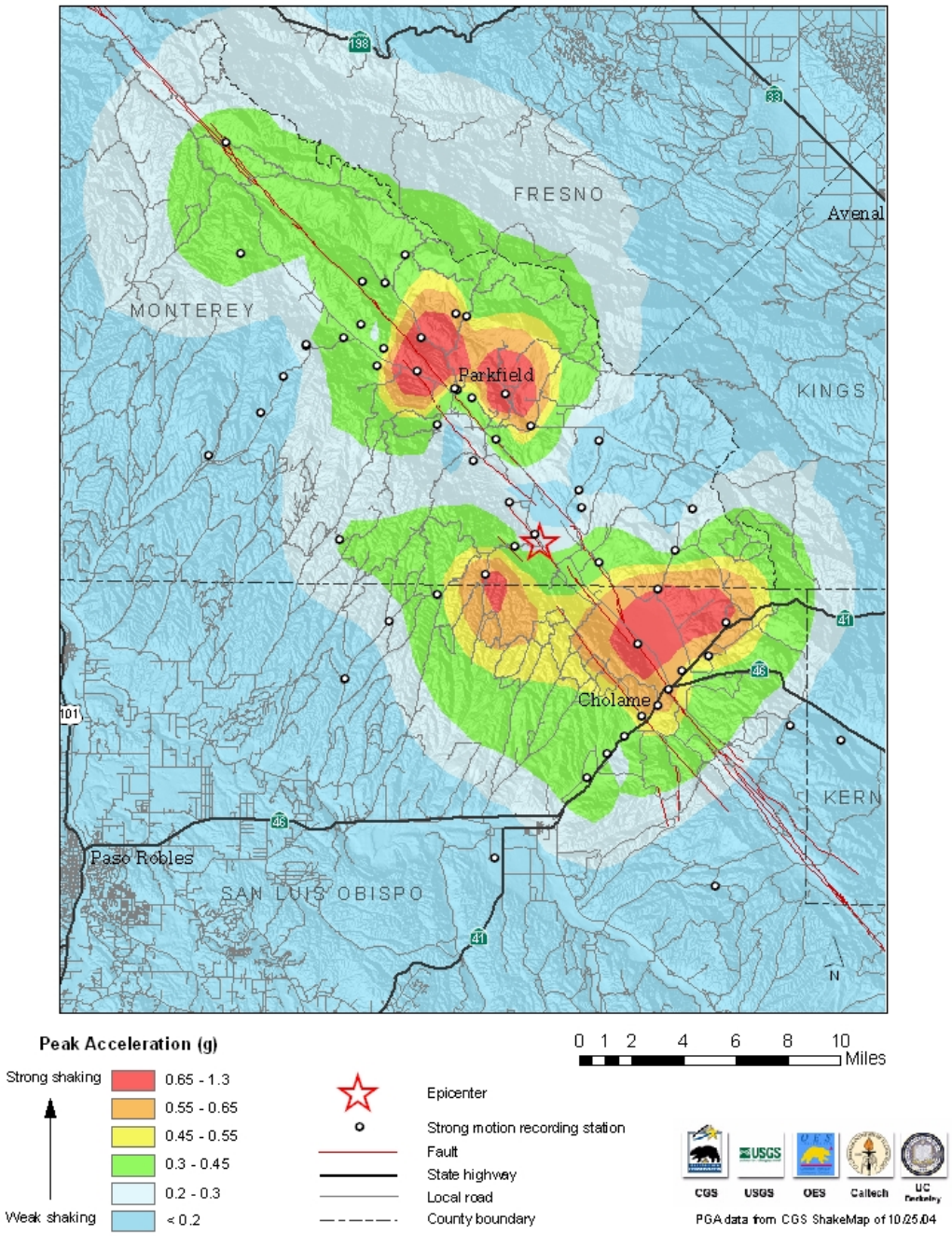


Figure 1. Contour map of near-fault peak ground accelerations. Locations of stations (CGS and USGS) are indicated. Areas of high amplitude shaking at the northwest and southeast end are clear, with low accelerations in the central segment near the epicenter (star).

## The Parkfield Strong Motion Array

The Parkfield strong motion array was designed to measure ground shaking close to a fault. Shown in Figure 2, the array includes instruments installed and maintained by both the California Geological Survey (CGS) and the U.S. Geological Survey (USGS). The CGS Parkfield strong motion array (McJunkin and Shakal, 1983) was installed during the early 1980s and consists of a network of 45 primarily analog strong motion recorders. Shortly after installation the array recorded an important set of records during the 6.5 $M_L$ 1983 Coalinga earthquake (Shakal and McJunkin, 1983). This data is important for comparison with the new data from the same stations to help understand site effects. The largest acceleration from that earthquake, which occurred 35 km north of the array, was 0.28g at Fault Zone 14; the rest of the stations had accelerations in the .05 - .20g range.

Complementing the initial set of recorders, after the Parkfield earthquake prediction experiment was initiated (Bakun and McEvilly, 1984) a network of 12 high-resolution GEOS recorders designed to provide on-scale broad-band measurements of earthquake shaking was installed by the USGS (Borcherdt et al., 1985; Borcherdt and Johnson, 1988). The GEOS stations include short period high-resolution measurements from collocated accelerometers and velocity transducers that provide a recording range extending from seismic background noise levels to 2g in acceleration. In addition, several sites include collocated volumetric strain sensors. The GEOS instruments obtained strong motion records at 11 sites. The values they recorded are very similar to values obtained from nearby classic strong motion recorders. The 180 dB dynamic resolution of the recordings will allow much more detailed analysis than analog film instruments, or digital instruments with less resolution.

Volumetric strain recordings (Borcherdt et al., 2004) were obtained at four of the GEOS sites and are among the first such recordings obtained in the near source region of an earthquake this large. They extend the bandwidth and dynamic range for near source motions to periods longer than possible from accelerometer measurements alone.

## Geologic Setting

Parkfield is at the northwestern end of the Cholame Valley, which extends from the vicinity of Parkfield to the southeast, where Hwy 46 crosses the valley (Figure 2). The valley lies between the Cholame Hills to the west and the southern Diablo Range to the east. The San Andreas Fault forms the boundary between the Salinian block on the west and the southern Diablo Range on the east. The geologic structure is complex to the east of the fault, where mostly metamorphic sedimentary and metamorphic rocks are exposed. The geologic structure is less complex to the west, with sedimentary deposits of late Cenozoic age over more complex Mesozoic bedrock of the Salinian block (Dickinsen, 1966; Dibblee, 1973; Jennings, 1977; McJunkin and Shakal, 1983).

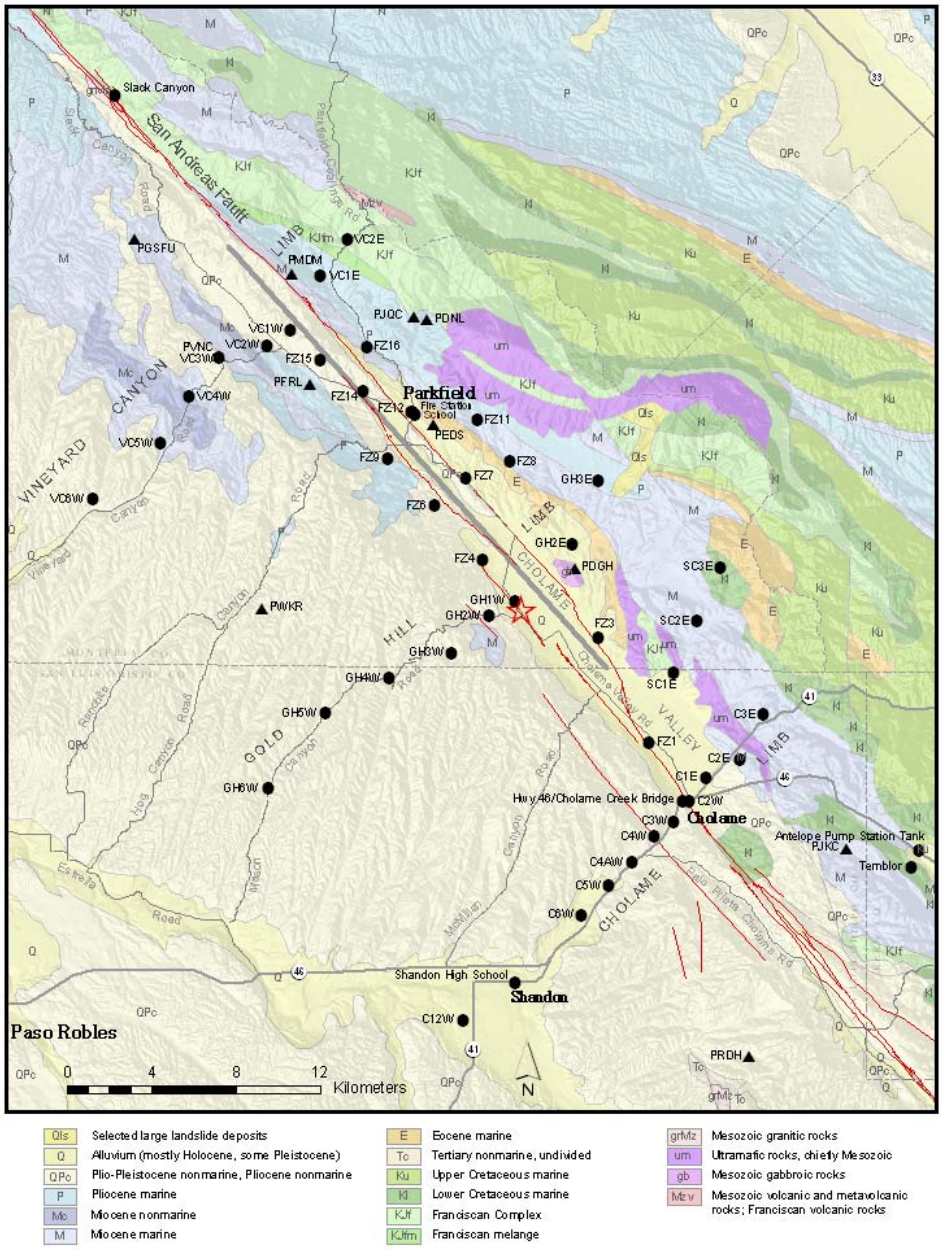


Figure 2. Stations in the Parkfield array plotted on a map of the regional geology (Jennings, 1977). Circles are CGS (mostly analog) strong motion stations; triangles are USGS high-resolution GEOS stations. The main strands of the San Andreas Fault and the earthquake epicenter (star) are shown. East of the alluvial Cholame Valley the geology of the Diablo Range is highly complex. The geologic structure is less complex to the west, with late Cenozoic sedimentary deposits. The earthquake surface faulting extends from near the epicenter northwest to Middle Mountain, northwest of Parkfield (Langbein et al., 2005). The line source model of Dreger (2004) is shown for reference. Codes for the CGS stations reflect the naming system (VC for Vineyard Canyon stations, GH for Gold Hill, C for Cholame, SC for Stone Corral, and FZ for Fault Zone).

## Array Configuration

The Parkfield strong motion array was designed to meet several measurement objectives. A major goal was to provide near-fault ground motion data complete enough that details of the rupture propagation process could be resolved. The configuration of the array, shown in Figure 2, reflects compromises between idealized objectives and practical aspects of logistics, field access, and site conditions. The array has the shape of a backward 'E', with three branches extending to the west, and a central near-fault pattern of stations paralleling the fault (called fault zone stations).

The three alignments, or limbs, of stations extending to the southwest, perpendicular to the fault, are called the Cholame, Gold Hill and Vineyard Canyon limbs. They allow study of attenuation with distance at near-fault distances. They extend to the west because the underlying formation is more uniform than the geologic structure to the east. The topography of the Diablo Range to the east also makes access more difficult; a general goal was to site the array stations to be accessible from normally passable roads.

The stations of the three limbs are sequentially numbered outward from the fault for each limb, starting from 1W for stations to the west, and 1E for stations to the east. The central set of stations are called the Fault Zone stations, and are sequentially numbered from Fault Zone 1 on the south end, near Hwy 46, to Fault Zone 16, north of Parkfield.

Several of the CGS stations in the Cholame limb along Highway 46 correspond to stations of the original 1966 array (Cloud and Perez, 1967). As installed in 1982, the array shared 4 locations with the 1966 set (Cholame 2WA, 5W, 8W and 12W). The reality of property owner issues compromised this set since, however. Station 8W was removed at the property owner's request, and 5W was moved about 1 km to the west. The location of 2WA approximately corresponds to the location of the Station 2 site of 1966. Only 12W is at the same location as the 1966 station.

The CGS stations are augmented by 12 high-resolution GEOS stations interspersed in the above pattern, installed by the USGS, with accelerometers and velocity transducers, and four have borehole volumetric strain dilatometers (Borcherdt et al., 2004). These sensors yielded some of the first measurements of strain during strong earthquake shaking.

## Peak Acceleration vs Distance

A comparison of the peak accelerations for this event with those predicted by standard relationships is useful. A plot of peak acceleration versus distance to the fault for the available set of 92 records is shown in Figure 3. The distances range from less than 0.5 km to 170 km from the fault. An important feature that makes this data set very important is the large number of recordings obtained within 10 km of the fault zone, which provide a rare opportunity for testing hypotheses about near-fault ground motion.

Five attenuation relationships for a strike slip fault are shown in Figure 3, including Boore-Joyner-Fumal (BJF97, Boore et al. 1997), Sadigh et al. (1997), Abrahamson and Silva (1997), Idriss (1993) and Campbell (1997). (For BJF97 an average shallow Vs of 350 m/sec was used, and the Sadigh et al. and Campbell relationships for soft soil sites were used, as most of the array sites are on alluvium). These attenuation relationships were developed for distances less than 100 km. Recordings from modern digital instruments provide data that is precise to low shaking levels. The data for this event, and other recently recorded earthquakes (e.g., M7.3 Hector Mine and M6.5 San Simeon; Graizer and Shakal, 2005) provide information needed to extend the existing attenuation relationships beyond previous limitations (80-100 km) out to distances of 200 km, important for larger earthquakes.

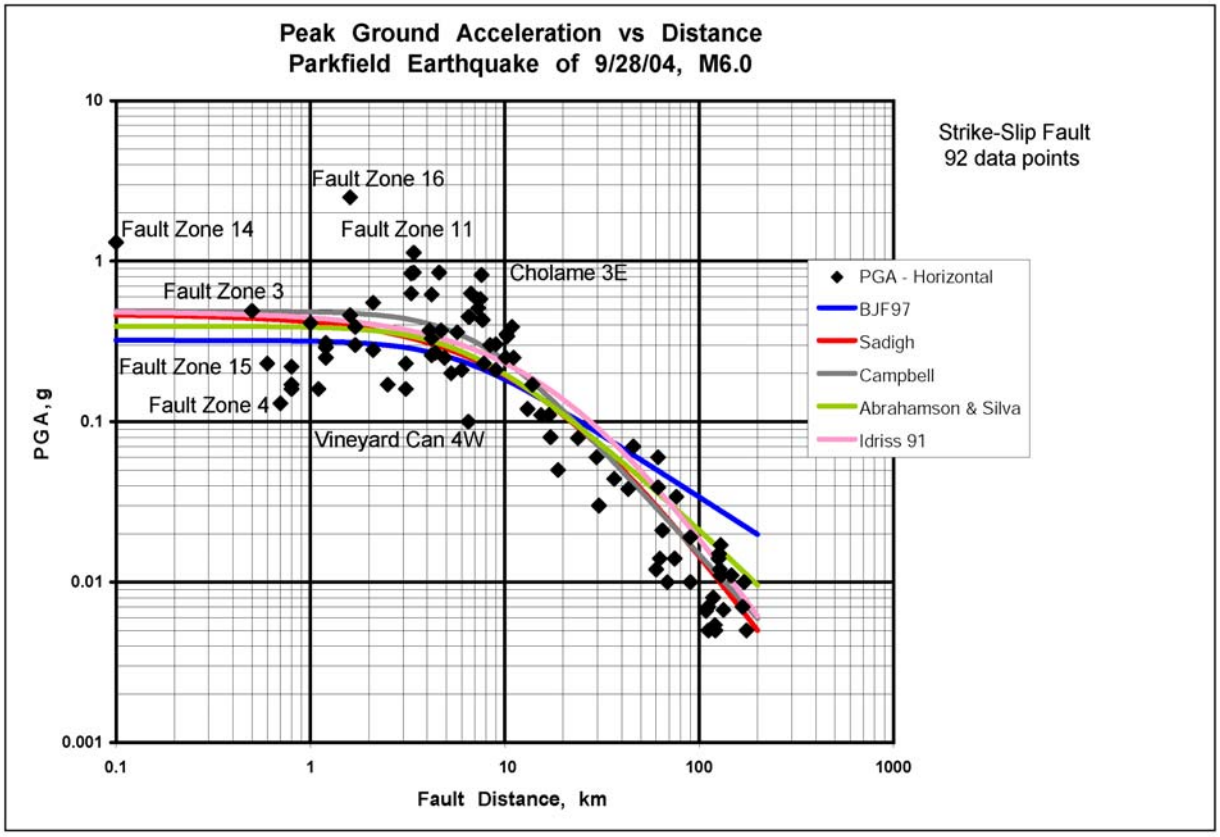


Figure 3. Horizontal uncorrected peak ground acceleration versus distance to the fault for data from the Parkfield earthquake of September 28, 2004. The attenuation relationship of Boore, Joyner and Fumal (1997; BJF97) is shown as well as the relationships of Sadigh et al. (1997), Campbell (1997), Abrahamson and Silva (1997) and Idriss (1993). The peak ground acceleration observations drop off more rapidly with distance than most of the curves. The largest peak accelerations are plotted here though strictly some (Sadigh, Campbell, Idriss) use the geometric mean of the two horizontals (which typically reduces the plotted value by 10%). All five relationships are extrapolated beyond 80 or 100 km. (Here and in subsequent plots the peak acceleration for Fault Zone 16, though known to be over 2.5g, is plotted at 2.5g.)

## Directivity in Peak Acceleration and Velocity

To study the effect of unilateral rupture directivity on peak ground acceleration the data set was split into two groups: stations located in the forward direction from the epicenter and in the backward direction. This grouping is based on the preliminary source modeling of unilateral rupture propagating from the epicenter to the northwest. In the resulting plot (Figure 4), directivity effects are not apparent in the near fault acceleration data for distances less than 10 km from the fault. At greater distances some differences in forward and backward directivity stations are suggested. The PGA data in the forward direction appears to attenuate slightly more slowly than in the backward direction.

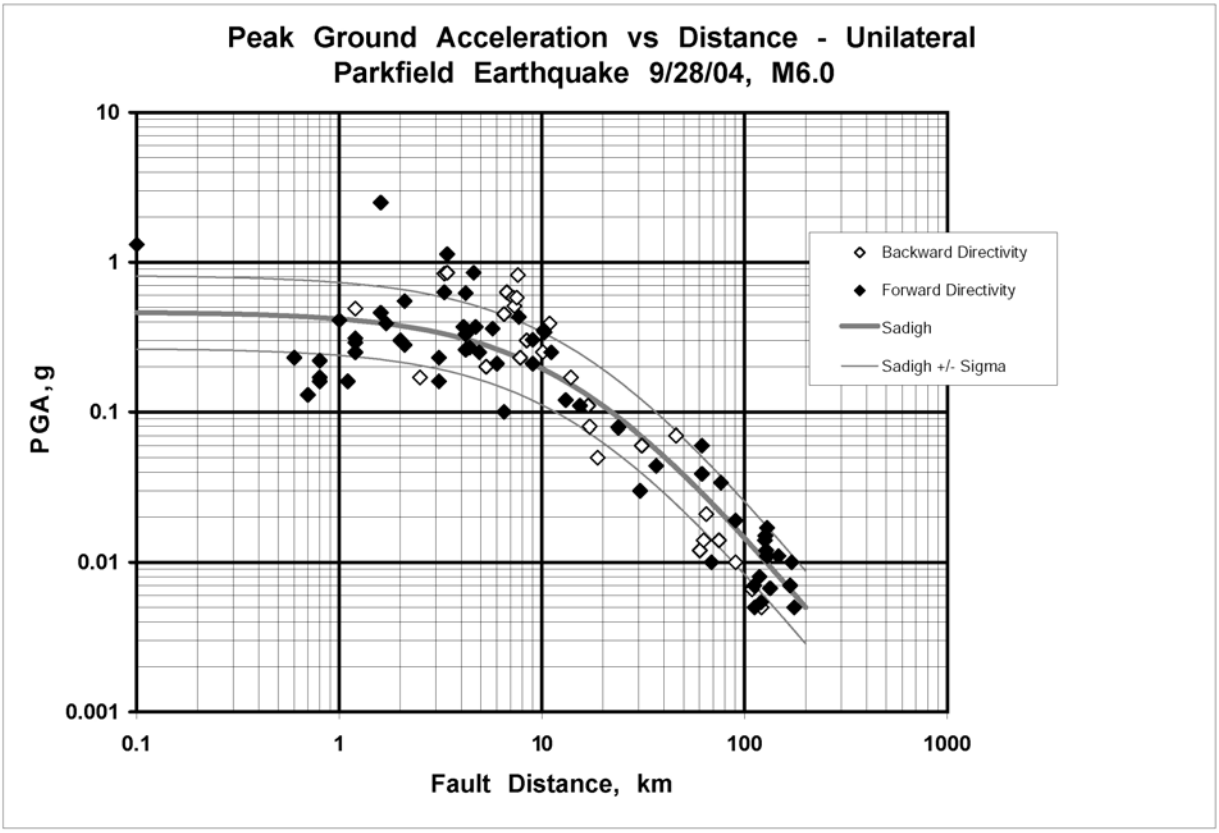


Figure 4. Peak ground acceleration considered as a function of simple directivity and unilateral rupture. The symbols are identified as either forward directivity or backward directivity according to the station locations either north or south of a northeast-southwest line passing through the epicenter, perpendicular to the fault. The Sadigh curve from Figure 3 is shown for reference. No difference is observable in the near-fault zone within 10 km of the fault.

The effect of bilateral rupture may be explored: some early modeling suggests bilateral rupture, with the southeast termination of the rupture located approximately 5 km southeast of the epicenter. In this model, the rupture starts at the hypocenter and propagates 5 km to the southeast and 20 km to the northwest. With this model in mind

the data were split into a group that were within ±45 degrees of the fault orientation, in either direction, and another group that were outside these regions. The resulting plot (Figure 5) shows more separation of the forward directivity stations than that shown in Figure 4. Figure 6 shows a similar plot of peak ground velocity, and the directivity effect is more apparent.

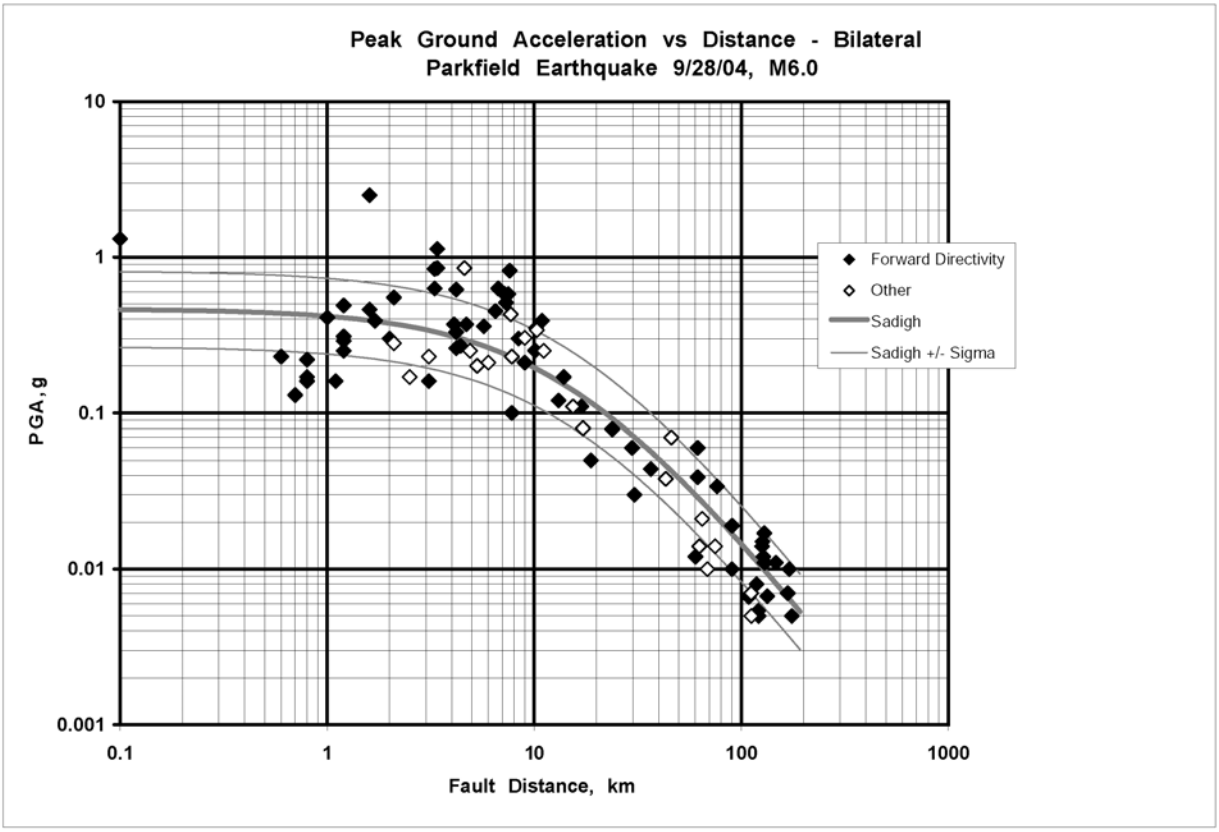


Figure 5. Peak acceleration versus distance data separated according to forward directivity in the case of bilateral rupture propagation, as described in the text. The Sadigh curve from Figure 3 is again shown for reference.

## Near-Fault Ground Motions

The strong motions in the near fault region are highly varied, with significant variations over relatively short distances, as reflected in the map of Figure 1. The map also shows concentrations of strong shaking at both ends of the fault. Peak ground acceleration in the near-fault region ranges from 0.13 g at Fault Zone 4, to 1.31 g at Fault Zone 14, ten times larger, to over 2.5 g at Fault Zone 16 (where the motion exceeded the instrument capacity). The largest PGA values along the fault zone occurred at stations within about 2 km of the town of Parkfield. The PGA in Parkfield is only 0.30 g, however, a fraction of the value at the surrounding stations. The reason for this difference is not yet clear.

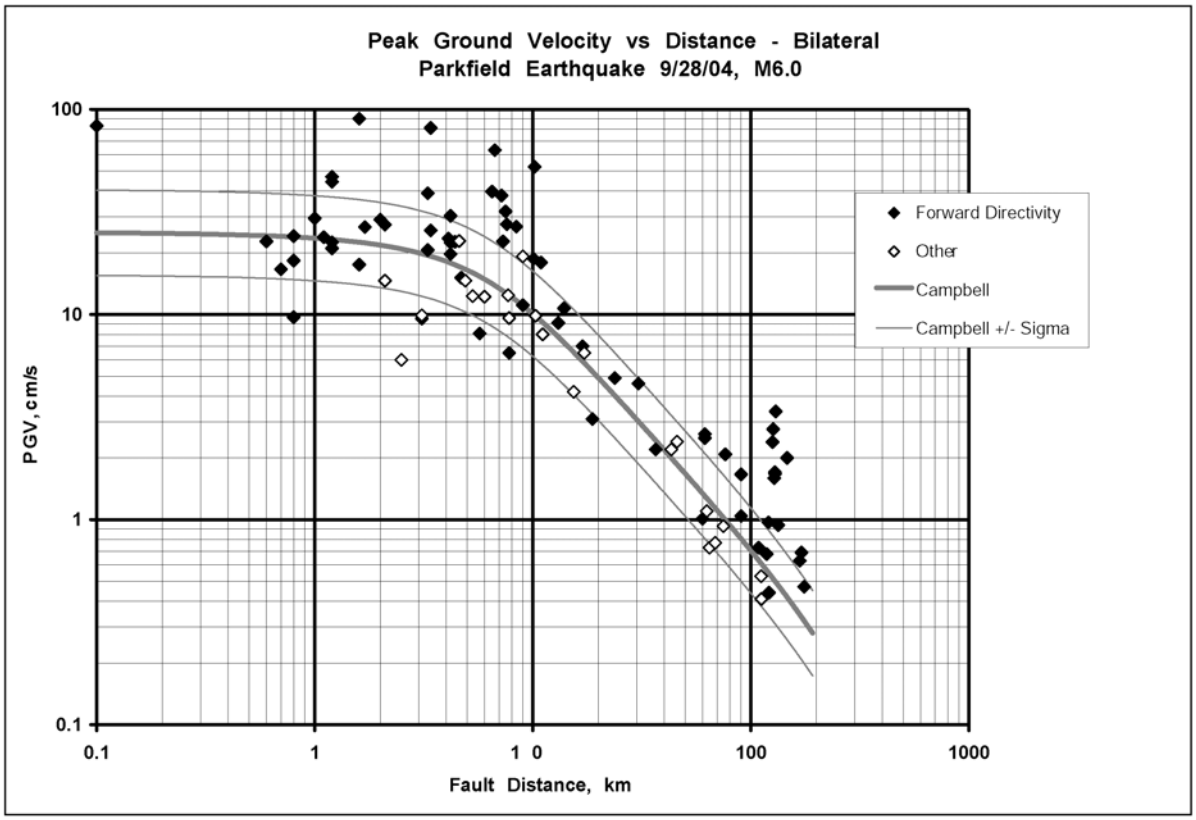


Figure 6. Peak velocity versus distance data separated according to forward directivity in the case of bilateral rupture propagation, similar to Figure 5.

Although several records have accelerations over 1 g, and one station, Fault Zone 16 is over 2.5 g, the largest well-recorded peak velocity is about 80 cm/sec (Fault Zone 15). This PGV is well below the largest values recorded in the 1994 M6.8 Northridge earthquake (150 cm/sec) and the values recorded in the 1999 M7.4 Taiwan Chi-Chi earthquake (300 cm/sec).

Some of the near-field records clearly reflect details of a complex rupture process. The displacement computed from the Fault Zone 15 record shows two pulses separated by about 3 seconds (Figure 7). This signal is so unusual that it might appear that there is a problem with a sensor or the processing. However the nearby stations Vineyard Canyon 1W and 2W also show this two-pulse signal, but with slightly different time separation. Thus, this shape is inferred to reflect radiation from the source, perhaps associated with local starting and stopping phases.

Several of the stations are ideally placed to record near-fault displacements, including the permanent offset. Unfortunately, two aspects work against the recovery of offsets from strong motion in this event. First, the event has relatively low slip (average slip of 15 cm, Langbein et al., 2005), and some of the actual visible slip at the fault did not occur until more than one hour after the event (i.e., the dynamic displacement signal occurred at the surface at the time of the rupture, but the static, permanent surface offset only occurred after near-surface soils yielded to the underlying motion to produce the

offset later). The second aspect is that the near-fault instruments are all film instruments, for which digitization limitations can easily lead to an uncertainty of several cm in the displacements at the period of a few seconds (e.g., Shakal et al., 2003). It may be possible to extract permanent displacements from some records, although even the dynamic displacement is only few cm at the stations near and over the rupture.

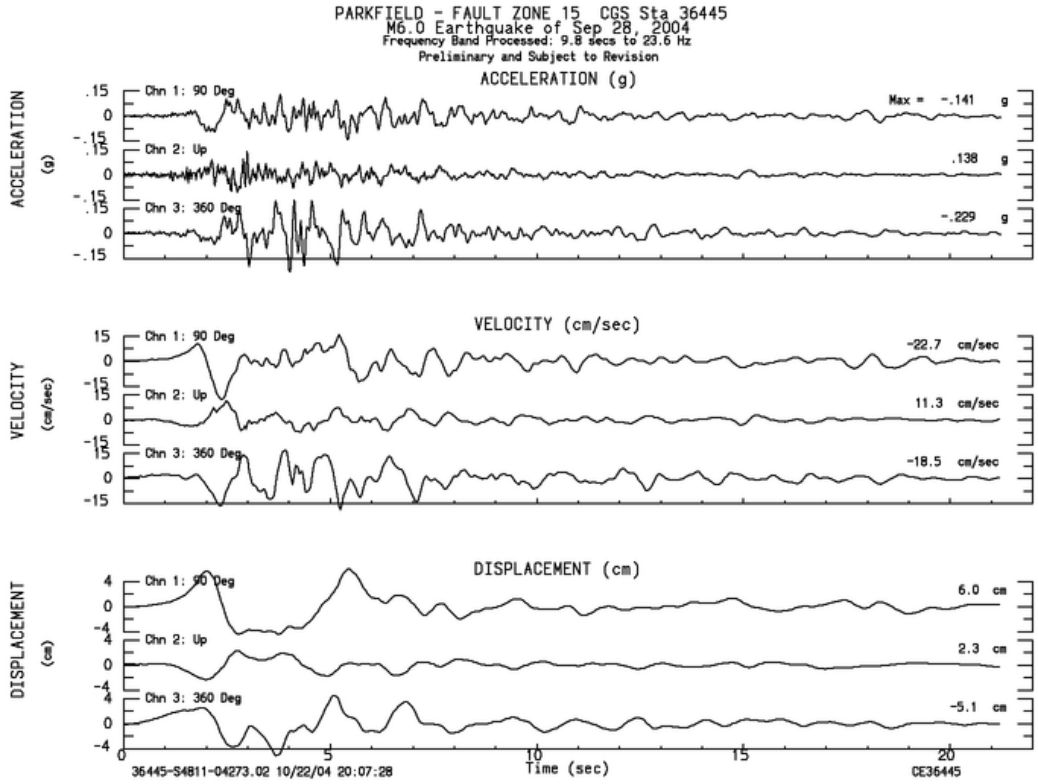


Figure 7. Acceleration, velocity and displacement at the Fault Zone 15 station, near Middle Mountain. The displacement shows two pulses separated by about 3 seconds, inferred to be associated with starting and stopping phases of rupture. Nearby stations (Vineyard Canyon 1W and 2W) also show these pulses.

## Particle Motions in the Near-Fault Region

Even though the near-fault motion is very complex, there are clear fault-normal pulses at stations near the ends of the rupture. These are shown on a map on which the displacement particle motions are plotted at the station locations (Figure 8). The stations at the southern end of Cholame Valley have the greatest displacement, mostly normal to the fault. The greatest amplitude is at Fault Zone 1, about 12 cm, perpendicular to the

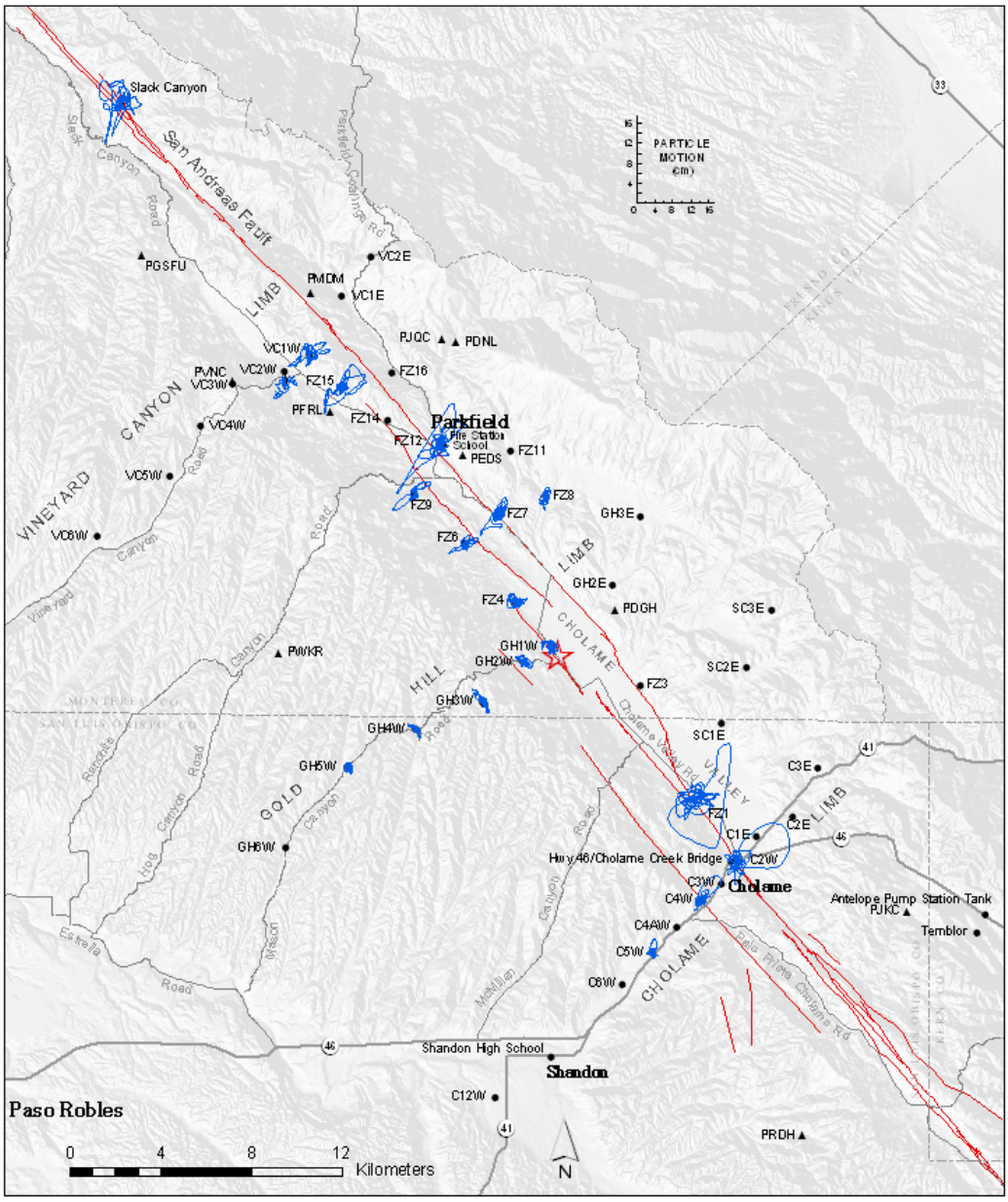


Figure 8. Horizontal displacement particle motions at stations in the near-fault region. The displacements obtained from integrating and processing the accelerograms are plotted at the corresponding locations of the stations. The fault-normal motions at stations near the ends of the fault are the largest amplitude displacements observed.

fault. Stations at the northern end of the fault also have significant fault-normal motions. The greatest is at Parkfield itself (Fault Zone12), where a displacement of ~10 cm occurs, almost exactly perpendicular to the fault. The motion at Fault Zone 16, not included in this figure, was almost perpendicular to the fault before the traces exceeded the instrument's recording capacity.

Two observations can be made for this set of near-fault measurements regarding the fault-normal motion. First, this motion is significant predominantly at the two ends of the fault. At intermediate stations in the central part of the fault, the fault-normal pulse is absent or small. Second, the amplitude of this pulse decays relatively rapidly away from the fault. The fault-normal pulse can be seen at stations of the Cholame limb, but it is smaller at 3W, and much smaller at 5W.

## Ratios of Vertical to Horizontal Motion

The ratio of vertical to horizontal peak ground acceleration, usually called the V/H ratio, is an important parameter in some engineering applications. For the Parkfield earthquake data, the average V/H ratio is 0.49 (log normal, with +/- sigma variations from 0.33 to 0.72). An attempt was made to identify any differences in the V/H ratio with distance to the fault, especially for the near-fault region, and it was found that the

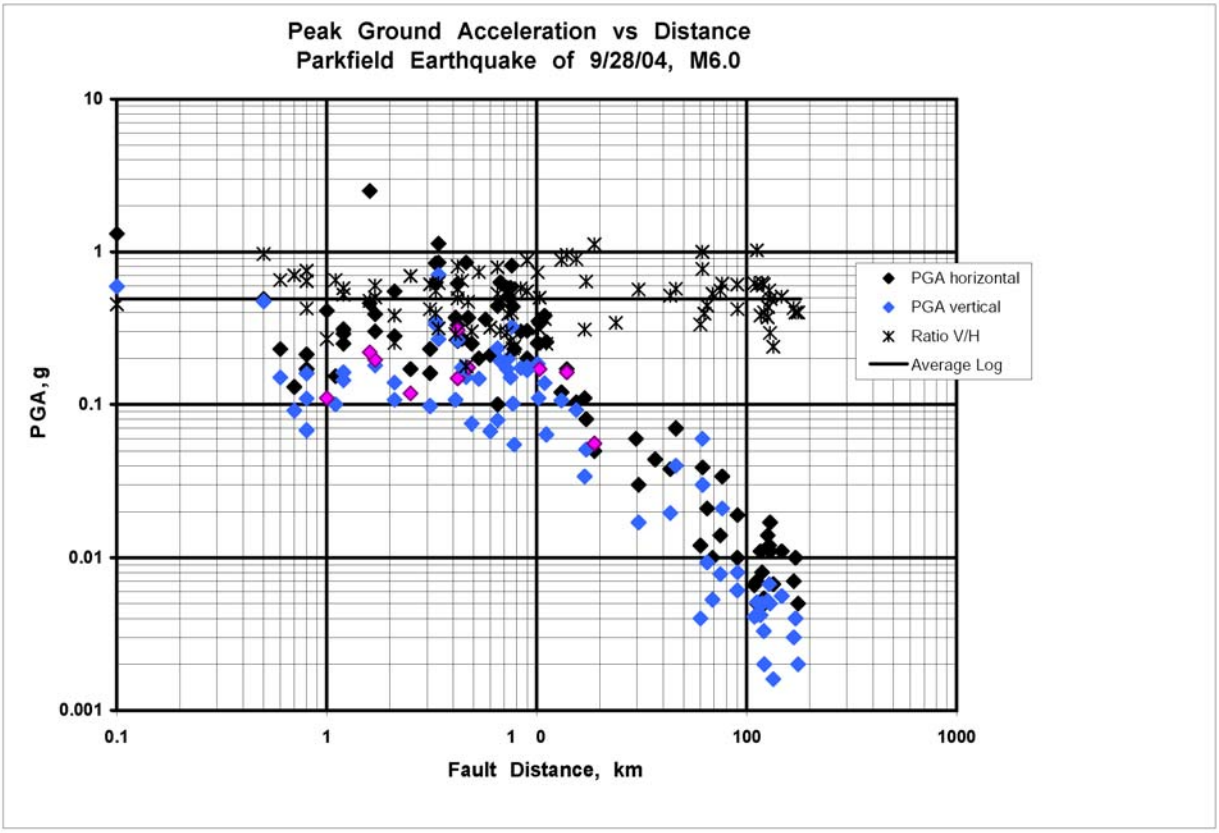


Figure 9. Comparison of the vertical and horizontal peak ground accelerations, and V/H ratios, for the Parkfield earthquake. The average V/H ratio for Parkfield is 0.49, similar to an overall ratio of 0.47 derived from 18 Californian earthquakes.

variations were insignificant. The investigation was extended to include strong motion data from 18 earthquakes of M > 5.5 (820 records). Based on this set of data Graizer and Shakal (2005) found that the V/H ratio is best described by log normal distribution, with an overall average ratio of about 0.47. The average ranges from 0.29 up to 0.69 for different earthquakes.

## Response Spectra in the Near-Fault Region

The response spectra of four stations in the fault zone area are plotted in Figure 10. They show that several records have predominantly high frequency spectral accelerations, as expected. However, several records also have high motions at periods near 1 second, which are potentially more damaging to many structures. The motion in Parkfield, though it has low peak acceleration, has significant energy at longer periods.

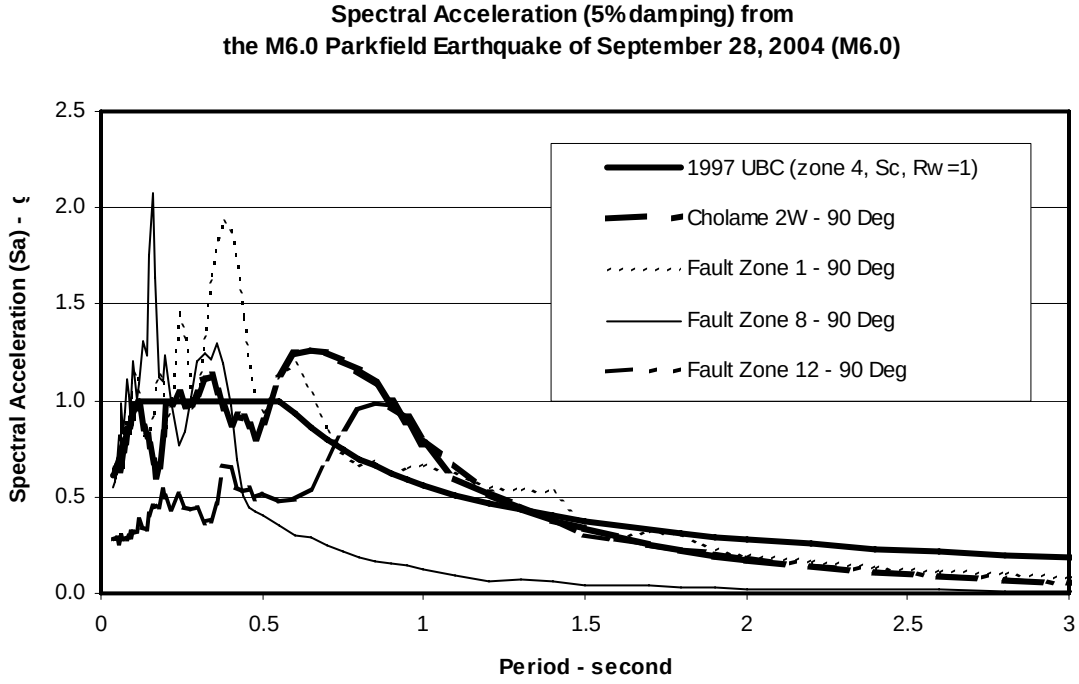


Figure 10. Comparison of acceleration response spectra at stations in the near-fault region. High frequency motion is seen at most stations, except Fault Zone 12. Stations near the ends of the rupture (Fault Zone 1, Cholame 2W, Fault Zone 12) have significant energy at periods near 1 second also.

## Strong-Motion Records from Structures

Although there were not many structures affected by the Parkfield earthquake, significant records were obtained from a Caltrans bridge on Highway 46 and two buildings at Parkfield. Post-earthquake inspection indicated that these structures did not suffer any structural damage.

The Cholame Creek bridge on Highway 46 is located about 150m (500 ft) west of the San Andreas Fault and 90 m (290 ft) west of the ground response station Cholame

2W. The bridge (128.5' long 32.5' wide) was built in 1954 and widened to 43.5' in 1979. The bridge is a five-span concrete structure supported on concrete pile bents and abutments. The west abutment is monolithic with the pile foundation, while the east abutment is monolithic with the new foundation but is seated on the old foundation.

Acceleration records were obtained from the six sensors on the bridge (Figure 11). The records show that a sharp peak of about 1 g occurred at the east abutment in both the bridge longitudinal and transverse directions. Only 0.67g was recorded at the west abutment in the transverse direction, and 0.48g at the center of the bridge. This difference may be due to the fact that the east abutment is more flexible than the fully monolithic west abutment. Cracks were observed on the roadway asphalt near both abutments, but the structural integrity of the bridge was not compromised.

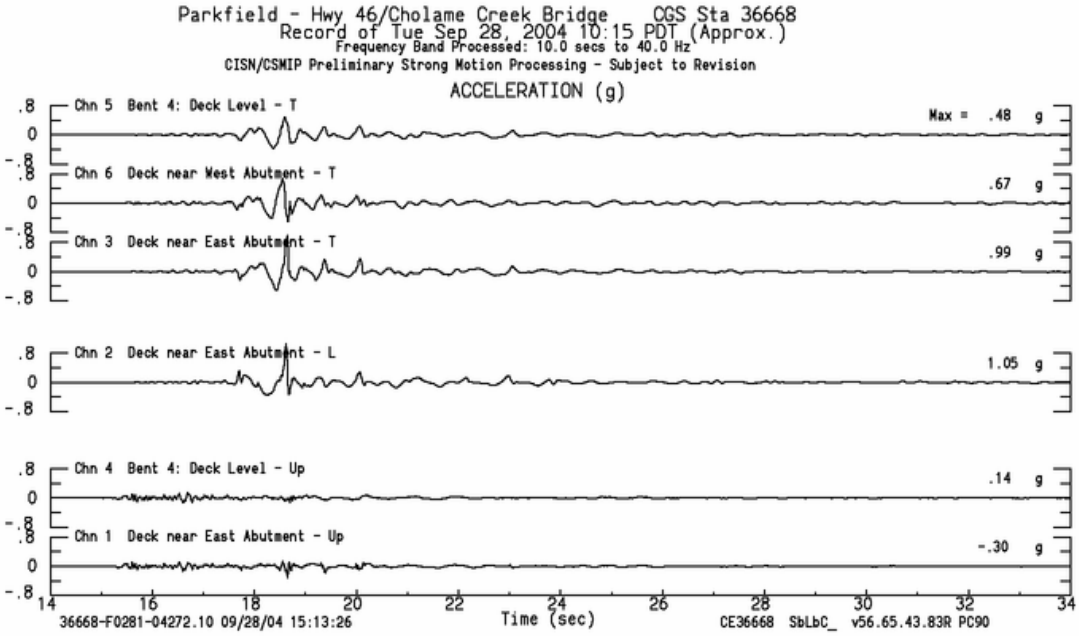


Figure 11. Acceleration records from the Cholame Creek Bridge at Highway 46. A large acceleration of about 1 g was recorded at the east abutment in both horizontal directions (channels 2 and 3). The motion recorded at the bridge is consistent with that at Station Cholame 2W, about 300 ft to the east. Despite this acceleration, the bridge did not suffer any structural damage.

The Parkfield Elementary School building is a 1-story wood frame structure built in 1949. The building has a plan dimension of 48 by 30 feet and a height of 13 feet. Accelerations records were obtained from the six sensors installed in the building (Figure 12). The maximum acceleration on the ground floor was 0.28 g in the N-S direction and 0.23g in the E-W direction, consistent with the motion recorded at the nearby ground response station Fault Zone 12, about 65 m (200 ft) from the school. The maximum acceleration recorded on the roof was 0.35g. Analyses of the displacements and response spectra of the records shows that the building period is about 0.2 second. With

this level of shaking, the building basically moved with the ground, with very little deformation.

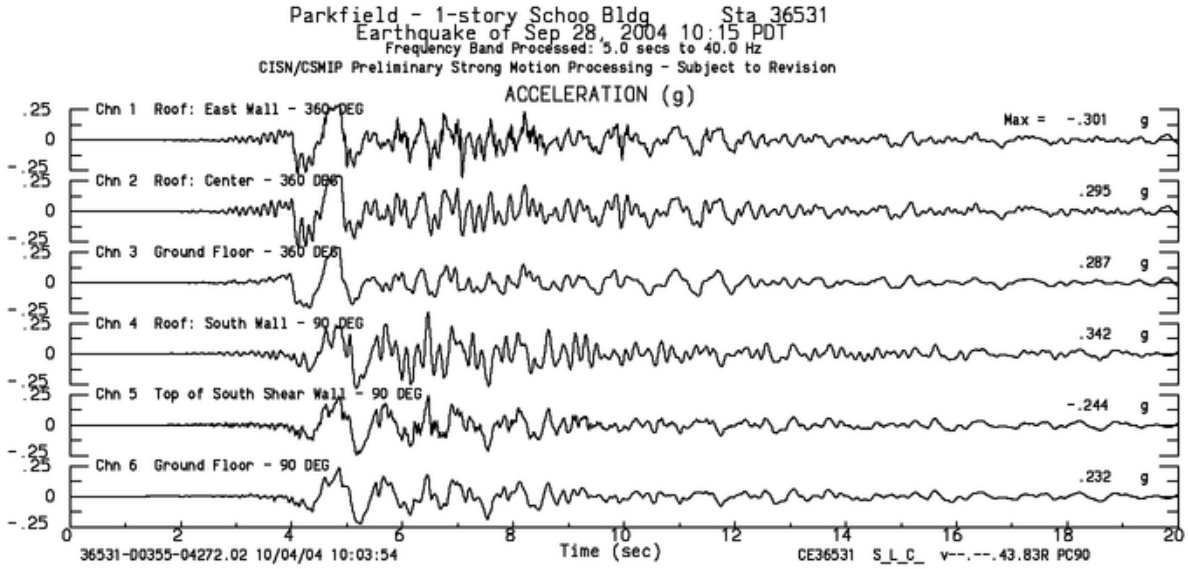


Figure 12. Acceleration records from the 1-story Parkfield Elementary School building. The recorded motions on the ground floor of the building are similar to those recorded at station Fault Zone 12, about 200 ft to the west. For this motion, the building moved with the ground, with very little deformation, and the building did not suffer any structural damage.

## Turkey Flat Experiment

In anticipation of the Parkfield earthquake, the CGS established a test area in a sedimentary valley at Turkey Flat, east of Parkfield, California in the late 1980s (Real and Tucker, 1987). The test site was instrumented with a strong motion array by CSMIP, and CGS partnered with the IASPEI/IAEE Joint Working Group on Effects of Surface Geology on Seismic Motion, as well as members of the geotechnical community, to thoroughly characterize the geophysical properties of the site. The strong motion array consists of surface and downhole accelerometers, with surface instruments at the two valley edges, at one quarter of the valley width, and at the center of the small, shallow 24m (80 ft) stiff-soil sedimentary valley. The instruments at the valley center also include a downhole array, with instruments just below the rock interface and at mid-height in the sediments.

The Parkfield earthquake was well recorded throughout this array, providing the records necessary to conduct the long awaited blind prediction test. In this prediction experiment, acceleration time histories recorded on bedrock near one valley edge will be provided to participants, along with a “standard” model of the subsurface geotechnical properties at all recording sites. Participants will be asked to make predictions of the ground motions at the valley center and other recording locations for which, as part of a

long-term plan, records are not being made public until the predictions have been received and officially logged. A workshop at which predictions can be presented and comparisons made with the recorded motions is planned for late 2005. Details of the test area and the test procedure are available at http://www.quake.ca.gov/turkeyflat.htm.

## Data Access

All of the data discussed here is available through the California Integrated Seismic Network's (CISN) Engineering Data Center (EDC), a joint effort of the CGS California Strong Motion Instrumentation Program and the USGS National Strong Motion Program. The files for all records are available at http://www.cisn-edc.org, having gone through digitization (if necessary), processing, and error checking. Both the processed data and the raw data are available and can be downloaded.

The GEOS recordings are available from the Internet at several locations as well as the CISN EDC. They are available from the Web site maintained by the National Strong-Motion Program in COSMOS format at http://nsmp.wr.usgs.gov/, linked to the COSMOS Virtual Data Center at http://www.cosmos-eq.org.

## Summary

The Parkfield 2004 earthquake yielded the most extensive set of strong-motion data in the near source region of a magnitude 6 earthquake yet obtained. The spatial density of the measurements along the fault zone and in the linear arrays perpendicular to the fault provides an exceptional opportunity to develop improved models of the rupture process. The closely spaced measurements help infer the temporal and spatial distribution of the rupture process at much higher resolution than previously possible.

The peak acceleration data vary significantly along the rupture zone, from 0.13 g to over 2.5 g, with the largest values concentrated at the two ends. Particle motions at the near-fault stations are consistent with bilateral rupture. Fault-normal pulses similar to those observed in recent strike-slip earthquakes are apparent at several of the stations. The attenuation of peak ground acceleration with distance is more rapid than that indicated by some standard relationships. Evidence for directivity in the peak acceleration data is not strong, but it is clearer in the peak velocity data. Several stations very near, or over, the rupturing fault recorded relatively low accelerations. These recordings may provide a quantitative basis to understand observations of low near-fault shaking damage that has been reported in strike slip earthquakes.

## Acknowledgements

Station siting permission from property owners in the Parkfield area made the instrument arrays possible. Installation the CGS stations was performed or overseen by Marvin Huston. Marvin, Tom Shipman and Ron Ayala performed most of the field data recovery; Bill Thompson maintained the stations carefully for the last 10 years, and Christopher Dietel maintained the USGS GEOS stations for years. Maintenance of

stations in remote areas like Parkfield, where neither power nor ready communication is available and access may be difficult, is a particularly difficult and tedious challenge; the success in recording data in this event depended on the diligent work of the individuals mentioned above. Pete Roffers generated the graphics that very effectively show the stations, geology and faults.

## References


Abrahamson, N.A. and W.J. Silva (1997). Empirical response spectral attenuation relations for shallow crustal earthquakes, *Seismological Research Letters* **68**, 94-127.

Bakun, W.H. and T.V. McEvilly (1984). Recurrence models and Parkfield, California, earthquakes, *Journal Geophys. Research*, **89**, 3051-3058.

Boore, D.M., W.B. Joyner, and T.E. Fumal (1997). Equations for estimating horizontal response spectra and peak acceleration from western North American earthquakes: A summary of recent work, *Seismological Research Letters* **68**, 128-153.

Borcherdt, R.D. and M.J.S. Johnston (1988). A broadband, wide dynamic range, strong-motion network near Parkfield, California USA for measurement of acceleration and volumetric strain: *Proc. Ninth World Conference on Earthquake Engineering*, **VIII**, 125-130.

Borcherdt, R.D., J.B. Fletcher, E.G. Jensen, G.L. Maxwell, J.R. Van Schaack, R.E. Warrick, E. Cranswick, M.J.S. Johnston, and R. McClearn (1985). A general earthquake observation system (GEOS): *Bulletin of the Seismological Society of America* **75**, 1783-1825.

Borcherdt, R.D., M.J.S. Johnston, C. Dietel, G. Glassmoyer, G. Myren, and C. Stephens (2004). Acceleration and Volumetric Strain Generated by the Parkfield 2004 Earthquake on the GEOS Strong-Motion Array near Parkfield, CA, *US Geological Survey Open File Report* **2004-1376**, 75pp.

Campbell, K.W. (1997). Empirical near-source attenuation relationships for horizontal and vertical components of peak ground acceleration, peak ground velocity, and pseudo-absolute acceleration response spectra, *Seismological Research Letters* **68**, 154-179.

Cloud, W.K. and V. Perez (1967). Accelerograms – Parkfield Earthquakes, *Bulletin of the Seismological Society of America* **57**, 1179-1192.

Dibblee, T.W., Jr. (1973). Regional geologic map of San Andreas and related faults in Carrizo Plain, Temblor, Caliente, and La Panza ranges and vicinity, California, *U.S. Geological Survey Misc. Geologic Investigations Map* **1-757**, scale1:125,000.

Dickinson, W.R. (1966). Structural relations of San Andreas fault system, Cholame Valley and Castle Mountain Range, California: *Geological Society of America Bulletin*, **77**, 707-725.

Dreger, D. (2004). 09/28/2004 Preliminary slip model. *CISN website*: www.cisn.org/special/evt.04.09.28/finite.dreger.html

Graizer, V.G. and A.F. Shakal (2005). Attenuation of peak ground motion and V/H ratios for three recent California earthquakes (abs.), *Seismological Research Letters* **76**, 237.

Idriss, I.M. (1993). Procedures for selecting earthquake ground motions at rock sites, NIST Report GCR 93-625.

Jennings, C.W. (compiler) (1977). Geologic Map of California, Geologic Data Map Series No. 2, California Department of Conservation, California Geological Survey.

Langbein, J., R.D. Borcherdt, D. Dreger, J. Fletcher, J.L. Hardebeck, M. Hellweg, C. Ji, M. Johnston, J.R. Murray, R. Nadeau, M. Rymer and J. Treiman (2005). Preliminary report on the 28 September 2004, M 6.0 Parkfield, California earthquake, *Seismological Research Letters* **78**, 10-26.

Liu, P., S. Custodio and R. Archuleta (2005). Finite-fault model of the 2004 Mw6.0 Parkfield earthquake from inversion of strong-motion data (abs.), *Seismological Research Letters* **76**, 210.

McJunkin, R.D. and A. F. Shakal (1983) The Parkfield Strong-Motion Array, *California Geology* **36**, 27-34.

Real, C.R. and B.E. Tucker (1987). Ground Motion Site Effects Test Area at Turkey Flat, California: *EOS, Transactions American Geophysical Union* **68**, 1350.

Sadigh K., C.-Y. Chang, J.E. Egan, F. Makdisi and R.R. Youngs (1997). Attenuation relationships for shallow crustal earthquakes based on California Strong Motion Data, *Seismological Research Letters* **68**, 180-189.

Shakal, A.F. and R.D. McJunkin (1983). Preliminary summary of CDMG strong-motion records from the 2 May 1983 Coalinga, California, earthquake, Calif. Dept. Conservation, Office of Strong Motion Studies, OSMS **83-5.2**, 49p.

Shakal, A.F., M.J. Huang and V.M Graizer (2003). Strong motion data processing, p. 967-981 *in* Intl. Handbook on Earthquake and Engineering Seismology, W.H.K. Lee, H. Kanamori, P.C. Jennings and C. Kisslinger, eds., Academic Press.

Shakal, A.F., V. Graizer, M. Huang, R. Borcherdt, H. Haddadi, K. Lin, C. Stephens and P. Roffers (2005). Preliminary analysis of strong-motion recordings from the 28 September 2004 Parkfield, California earthquake, *Seismological Research Letters* **76**, 27-39.

# ANIMATION OF GROUND SHAKING FOR CALIFORNIA EARTHQUAKES

Timothy I. Mote and John A. Egan

Geomatrix Consultants
2101 Webster St. 13th, Oakland, CA 94612

## Abstract

An animation tool for visualizing ground shaking amplitude, oscillations, and duration using existing strong-motion datasets was developed to help interpretation and understanding of strong-motion propagation and attenuation. The system uses readily available strong-motion datasets, seismic velocities, and the ShakeMap model to interpolate ground motions by time-shifting and amplitude-scaling proximal records across a study area. The animation system essentially adds a temporal dimension to the ShakeMap model. Five significant historical California earthquake animations were developed with this system (1999 Hector Mine, 1992 Landers, 1989 Loma Prieta, 1994 Northridge, and 2004 Parkfield earthquakes) and are available on the Web at www.gmxwebsolutions.com/eq_animations.

## Introduction

Ground shaking from earthquakes varies spatially across a region based on the distance from the fault rupture (i.e. attenuation), seismic wave propagation velocities (P-Waves and S-Waves), attenuation relationships, and bedrock geology. At any snapshot in time following nucleation of an earthquake, a given location within that region will be in the midst of either strong ground shaking, no ground shaking as the seismic waves will have yet to arrive, or subsiding ground shaking as the seismic waves will have passed and ceased. The behavior of shaking during earthquakes is of interest to a broad spectrum of people from the general public to the earthquake engineering community. A ground shaking animation tool that can visualize ground shaking amplitudes, oscillations, and duration using existing strong-motion datasets from recent earthquakes can be a powerful educational tool, as well as help interpretation and understanding of strong-motion propagation and attenuation.

The prevalent and accepted standard visual representation of shaking across an entire region affected by an earthquake is the CISN Rapid Instrumental Intensity Map or ShakeMap. ShakeMap, developed by CSMIP and USGS, takes applicable records and calculates peak ground motion parameters (peak ground acceleration (PGA), peak velocity (PGV), peak displacement (PGD)) at constant grid spacing across the study area. While ShakeMap provides an excellent representation of ground motion for a specific event, it is a static view of the motion and does not describe what each of us feels or

observes during an earthquake, the time history effects of seismic wave arrival, amplitude oscillations, and shaking duration.

Digital, free-field strong-motion station records typically report values for acceleration, velocity, and displacement recorded from 3 channels (2 horizontal and 1 vertical). This produces a total of 9 variables (3 channels x 3 parameters) per time interval (commonly 0.02 seconds) to characterize earthquake ground shaking at that station. With the current network of digital strong-motion recording stations across California, we can obtain a spatially diverse set of detailed time-history records describing the ground shaking for a specific earthquake. This equates to approximately 200,000 values describing motion per station or on the order of 10,000,000 values for an entire event from every station recording. This plethora of data and the desire to temporally visualize ground shaking amplitude, oscillations and duration using existing strong-motion datasets leads the impetus for this study.

If the distribution of stations throughout the study region was dense and regularly distributed (stations on a 1km grid), then creating these animations would be simply synchronizing the records into a GIS system and extracting time-slices without interpolation. To create an animation based on the existing network of irregularly and far-spaced stations, we have developed an interpolation methodology to derive ground shaking time histories for areas away from the existing stations. The derivation of ground shaking history must take into account proximal strong-motion data, seismic velocities, geologic conditions, distance from the earthquake source and appropriate attenuation relationships. The tool uses readily available strong-motion datasets, seismic velocities, and the ShakeMap model to interpolate shaking by time-shifting and amplitude-scaling ground motions across a study area at any specified time-step. The animation system essentially adds the temporal dimension to the ShakeMap model.

Initial animations were based on available strong-motion data from the 1999 Hector Mine, 1992 Landers, 1989 Loma Prieta, 1994 Northridge, and 2004 Parkfield earthquakes. The process developed will also be used to readily produce animations of future earthquakes. These animations will help educate a broad spectrum of people, as wells as aid in interpretation and understanding of strong-motion propagation on the ground surface.

## Data Acquisition and Pre-Processing

### Strong Motion Data

Available digital, free-field strong-motion station records for all five designated earthquakes were acquired (Figures 1a, 1b, 1c). Records acquired from CSMIP generally had complete digital headers, including trigger times, and were easily parsed into the model database (Access) with an automated script. Supplemental records from other sources (e.g. USGS, USC) were acquired and integrated into the database manually where there were significant spatial gaps in the model.

Data records were processed and parsed into a database-ready format via a customized automated parsing script. The free-field records report values for acceleration, velocity, and displacement recorded from 3 channels (2 horizontal and 1 vertical). This produces a total of 9 variables (3 channels x 3 parameters) per time interval.

In addition to the strong-motion time histories, station parameters from the record header were also parsed into the model database. Station parameters include station-id, location (latitude and longitude), PGA, PGV, channel orientations, trigger time, and record time interval. The lack of consistent and complete headers (e.g., no trigger times) of the other data sources proved time-consuming to manually process. The station-to-epicenter distance was calculated using a standard GIS functionality for each record.

To simplify the visualization of ground motions, we use an absolute horizontal acceleration by taking both horizontal acceleration channels and calculating one absolute value using the square root sum of squares algorithm. The ground shaking animations presented here visualize this absolute horizontal acceleration. Future modeling efforts can isolate individual directional channels or the other ground motion parameters (velocity and displacement).

### ShakeMap Data

ShakeMap model values for all five designated earthquakes were acquired via the CSMIP Web site and imported into the model database (Figures 1a, 1b, 1c). The ShakeMap model provides peak ground motion parameters (PGA, PGV, PGD) at constant grid spacing across the study area. We use the inherent ShakeMap grid spacing to define the animation model grid. The cell-to-epicenter distance was calculated using standard GIS functionality for every model cell.

## Interpolation Methodology

We have developed an interpolation methodology that models shaking for any cell in the model using proximal strong motion records, seismic velocities, and ShakeMap to estimate ground motion time histories. The interpolation methodology can be summarized as follows:

For any model cell:

- **Search** the existing stations to find the three most appropriate records from which to extract values.

- **Shift** the time of each of the three records by a time interval derived from the difference in distance between the model cell-to-epicenter and station-to-epicenter distance divided by the characteristic seismic velocity.

- **Scale** the amplitude of each of the three records based on a ratio between the ShakeMap-derived PGA at the model cell and the station.

- **Interpolate** values from the three shifted and scaled records into one value with the Inverse Distance Weighted algorithm using the three respective cell-to-station distances.

- **Normalize** the interpolated time histories to the ShakeMap.

Details of these modeling components are discussed below.

**Search**

Integral to our interpolation methodology is the selection of the three most appropriate stations from which to extract strong-motion records when estimating ground motion at any grid cell in our model. Selecting the three closest (cell-to-station distance) stations is the most simplistic solution, but it might not be the best when approximating ground motions. Ideally, the three stations should have a radial distance from the epicenter similar to the cell being modeled. This would support a better estimation of records, as attenuation and seismic wave arrival times are theoretically similar. In parts of the model where stations are sparse, this selection criterion becomes more important. For example, in the Parkfield model, grid cells 70km east of the rupture are closest to near-field stations, due to a lack of stations east of the rupture (Figure 1c). Extrapolating the shorter and stronger near-field records eastward to 70km is a greater and probably inappropriate extrapolation compared to using the stations 70km west of the rupture, even though these stations are 140km from each other and in opposite directions from the epicenter.

We developed criteria to select the three most appropriate stations to use when modeling any grid cell. The criteria are based on both closest cell-to-station distance and similar cell-to-epicenter and station-to-epicenter radial distances. Initially the algorithm selects all stations with cell-to-station distances less than 1/3 of the cell-to-epicenter radial distance. If more than three cells fall within this zone, the algorithm selects the closest three. If less than three stations meet this criterion, the algorithm then selects stations with station-to-epicenter radial distances within 1/3 of the cell-to-epicenter radial distance (Figure 2). To remove bias in the Inverse Distance Weighting algorithm used by the interpolation methodology to equate ground motion, the stations selected by the radial distance criterion are assigned a cell-to-station distance of 1/3 the cell-to-epicenter distance. For earthquake animations where the spatial station distribution is sparse (i.e., Hector Mine; Figure 1a) the 1/3 search ratio was increased to ½.

**Shift**

To interpolate a ground shaking time-history from a station to any model cell, we must shift the selected proximal records to accommodate for travel times of seismic

waves through the geologic medium. In order to shift these ground motion records two characteristic seismic velocities are needed.

### *Calculate Seismic Velocities*

To derive the seismic velocities (P-Wave and S-Wave) for the five designated earthquakes, we plot the seismic wave arrival times versus the station-to-epicenter distance for each record. Seismic wave arrival times, for both P- and S-Waves, were manually chosen from visual inspection of the original time history. Fitting a line to the data allows us to derive the seismic velocity from the slope of the line. We assume that seismic velocities are constant within the study area for each earthquake. Figures 3a, 3b, and 3c show the distance versus arrival time for all five of the designated earthquakes.

### *Evaluate Trigger Times*

Critical to the calculation of the characteristic seismic velocities and shifting the time histories is synchronization of the records to the earthquake origin time by trigger time. Ideally, trigger times are included in the record header, but occasionally these times are either missing or erroneous. These records are problematic and must be manually evaluated. Using the arrival times versus station-to-epicenter distance plots (Figures 3a, 3b, and 3c) we can manually assign trigger times to missing records and correct erroneous ones. CSMIP records from the more recent earthquakes report correct and complete trigger times more consistently than older and non-CSMIP records.

### *Limited Record Length Adjustment*

The duration (total time) of the time histories vary from station to station. This variation does not appear to be based on station-to-epicenter distance or amplitude. For example, neighboring (<10km apart) Parkfield near-field stations have record lengths of 25 and 80 seconds. This variation in duration of recorded data is accommodated in the model to ensure that the most appropriate data for the longest time interval are used. During the estimation modeling, if an appropriate station is being used at a time-step beyond its record length, then the algorithm will step to the next appropriate station selected in the search algorithm detailed above.

### *P-Wave and S-Wave Velocity Shift*

The interpolation methodology uses the three most appropriate station records to estimate ground motion at any arbitrary grid cell in the model. Strong-motion records from these three stations are time-shifted to account for the difference in spatial distance between the grid cell and station. The time-shift is based on the distance between the grid cell and the station converted into time by the seismic velocity. To accommodate both P-Wave and S-Wave arrival components of the records, we apply different time-shifts based on the distinct arrival times of the two waves. Initially, this time-shift is based on P-Wave seismic velocity. As the model time progresses and the arrival of the S-Wave occurs, the time-shift is based on the S-Wave seismic velocity. This methodology

essentially separates the wave components to synchronize the arrival of both the P-Wave and S-Wave throughout the model.

### Scale

To interpolate shaking amplitude from distance records to any model cell, we scale the selected record to attenuate the shaking amplitude as the seismic waves travel through the geologic medium. The records are scaled by the ratio of ShakeMap-modeled PGA at the model cell to the recording station. ShakeMap provides a model structure where attenuation relationships and geology have been included in algorithms to estimate peak ground motion parameters (PGA, PGV, PGD). Since the ShakeMap PGA model generally decreases away from the epicenter, using this ratio will dampen or heighten amplitudes as you move away or closer to the epicenter, respectively, across a model area (Figures 1a, 1b, 1c). Using the ShakeMap model integrates these attenuation relationships into the animation tool.

### Interpolation

With the three most appropriate records selected, shifted, and scaled to account for attenuation and seismic velocity travel times, we calculate a new time history for every model grid. At every time interval, we take the three shifted and scaled values and use the Inverse Distance Weighting algorithm with the respective cell-to-station distances to calculate an instantaneous ground motion. Iteration of this process through the desired time duration on a cell-by-cell basis generates complete time histories for every cell in the model.

### Normalization to ShakeMap

To honor the ShakeMap PGA model grid, every modeled cell time history is normalized to ShakeMap PGA after the completion of the interpolation methodology. For example, if the interpolation algorithm estimates a record for a grid cell with a peak or maximum modeled acceleration of 0.70g at a location where ShakeMap models a PGA of 0.77g, the normalization algorithm will scale the record by 110 percent. The opposite also applies, where the normalization algorithm can scale down an interpolated record to match ShakeMap.

## Model Validation

A validation step was completed to compare the modeled strong motion time history for arbitrary grid cells versus the observed (recorded) data in proximal locations. Modeled ground motions for areas far away from stations were also examined. To check the validity of our interpolation algorithm, the modeled ground motion time histories for specific cells in the model were plotted against the actual station strong-motion recordings. Validation of the model includes comparing the amplitude, duration, and inflection points of the modeled curve to the observed curve.

The first check looks at a model cell spatially coincident with a recording station. We looked at station 47232 and model grid cell 4108, which are <1 km away from each other and both ~80km away from the epicenter (Figure 2). Comparison of the two graphs shows that their overall shape, magnitude, and duration are fairly consistent (Figure 4). The inflection points (P-Wave, S-Wave, PGA, and motion decrease) are all fairly equivalent. The similarity of these two graphs (modeled and observed) is expected, as our interpolation algorithm gives the greatest weight to the closest of the three most appropriate stations. The close spatial proximity of the station 47232 to model grid cell 4108 implies that the other two closest stations, although still included in the estimation, will have a significantly lesser weight.

Another critical check is to look at the overall wave form of a model cell far away from any stations. We looked at model grid cell 13672, which is 75km SSE of the rupture (Figure 2). While the closest stations to this cell are the Parkfield near-field cells ~50km away, the station search criteria chooses appropriate stations at a comparable epicenter radial distance. The overall wave form of model grid cell 13672 looks similar to station 47232 at similar approximate distances from the epicenter, 75km and 80km respectively. The initiation of strong ground motion begins at ~13 seconds, which corresponds to the modeled seismic velocity of 5,800 m/s (75,000 / 5,800 = 12.9 seconds) (Figure 5).

## Animations

Once the complete ground shaking time histories are interpolated for each model cell, we extract instantaneous values from these time histories and use the GIS (ArcGIS) to create a gridded surface of ground motion at that specific time. The gridded surface of instantaneous acceleration is visualized with a color scheme consistent with the ShakeMap ground shaking legend. This gridded surface is layered onto the GIS basemap (digital terrain model, roads, and station locations) to provide a spatial reference frame and then saved as an individual map still-frame. Iterating this process at a desired time interval creates a series of map still-frames. The sequential compilation of these map still-frames within an commercial animation generator (i.e. QuickTime) creates a Web-ready animation of ground shaking duration and amplitude radiating away from the epicenter (Figure 6).

Animations for all five designated earthquakes, at an interval of 0.5 seconds, were produced and can be found on the web at www.gmxwebsolutions.com/eq_animations.

## Discussion and Future Goals

This animation tool begins to take the copious amounts of digital free-field strong motion data and visualize the ground shaking amplitude, oscillation, and duration using existing strong-motion datasets in a temporal sense. The animation tool takes seismic velocities and existing time-histories to interpolate ground motion records across the study area. The tool also integrates attenuation and geologic conditions by using the ShakeMap model to scale ground shaking amplitudes. Validation of our interpolation methodology, by comparison of observed to modeled time-history curves, shows that we

can successfully create a ground motion time-history at any arbitrary location in the model.

The overall dynamics of the ground shaking animation captures the behavior of seismic waves traveling through the geologic medium. The earthquake animations show strong-motions proximal to the epicenter at the nucleation of the event and decreasing motions emanating away from the source with time. Both P-Wave and S-Wave can be recognized and tracked at their respective velocities in the animations. Attenuation relationships, integrated from ShakeMap, can also be recognized as well as the interaction between rock/alluvium surface geology and the shaking.

The animation model as currently implemented is limited to the amount and spatial distribution of existing CSMIP strong motion records and occasional supplemental records from other sources. While we have tried to include all readily available substantial datasets there are other datasets that exist for some of the earthquakes in this study (e.g. USGS, universities, utilities, private owners), which were not presently included in these models due to the time necessary to manually prepare individual recording to incorporate into the model.

With the completion of the animation system and interpolation methodology, future goals will include:

- Focusing the animation on isolating the nine other ground motion parameters.
- Focusing on near field-effects of the Parkfield dataset.
- Extending out beyond the existing ShakeMap grid and looking at far-field effects.
- Attempting to include a more robust geologic model.
- Modeling historic earthquakes such as the 1906 San Francisco earthquake that pre-date recording of strong ground motion.

## Acknowledgements

The authors are grateful to CSMIP for providing the funding for this project. Thanks go to Moh Huang, Tony Shakal, and Vladimir Graizer for providing support throughout this project. Execution of this study could not have been accomplished without support from Geomatrix staff including Dr. Shawn Chen, David O'Shea, Javier Chalini, Dr. CC Chin, and Donald Wells.

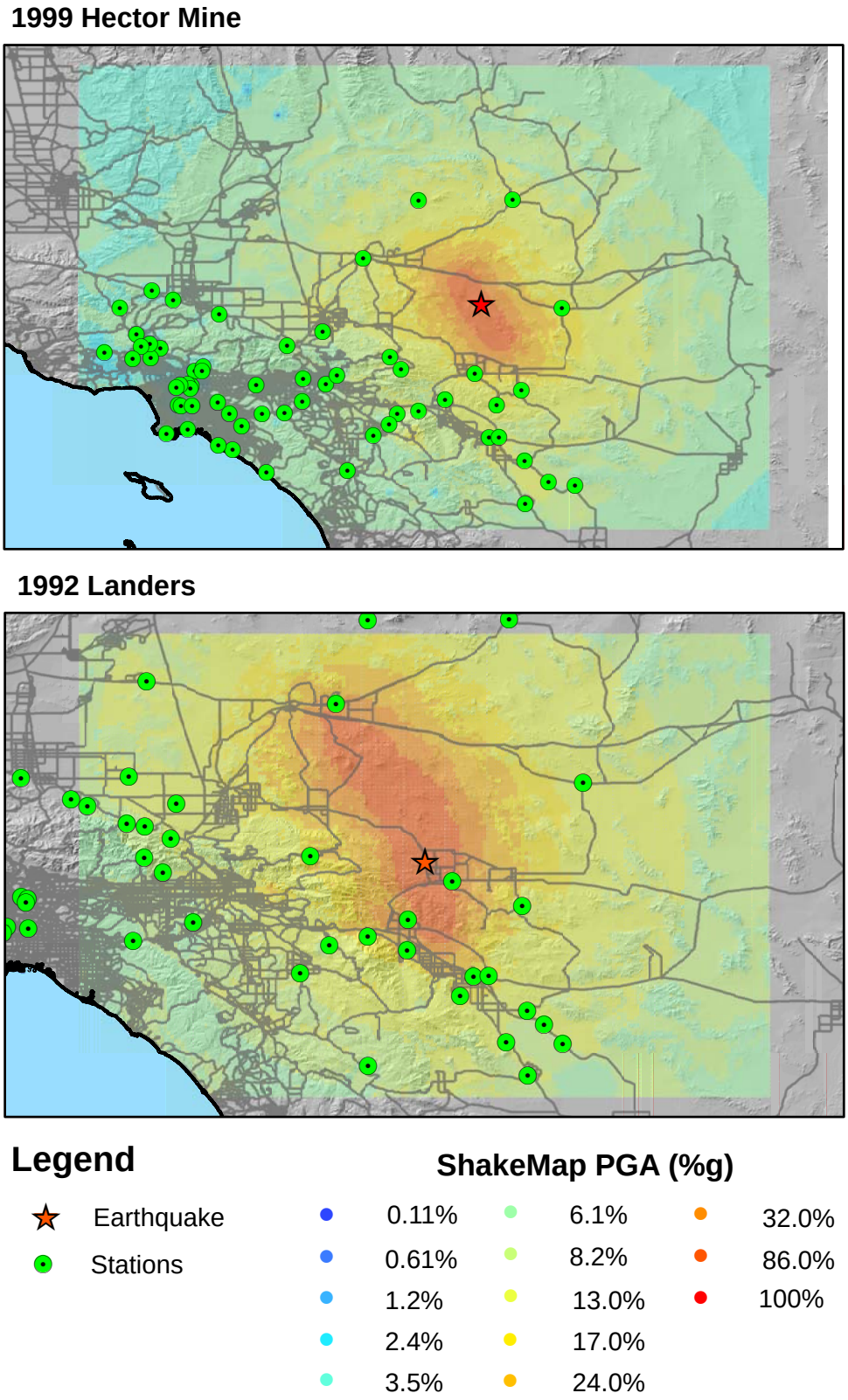


**Figure 1a.** Location of available strong motion recording stations and ShakeMap PGA models for the 1992 Hector Mine (top) and 1992 Landers (bottom) earthquakes.

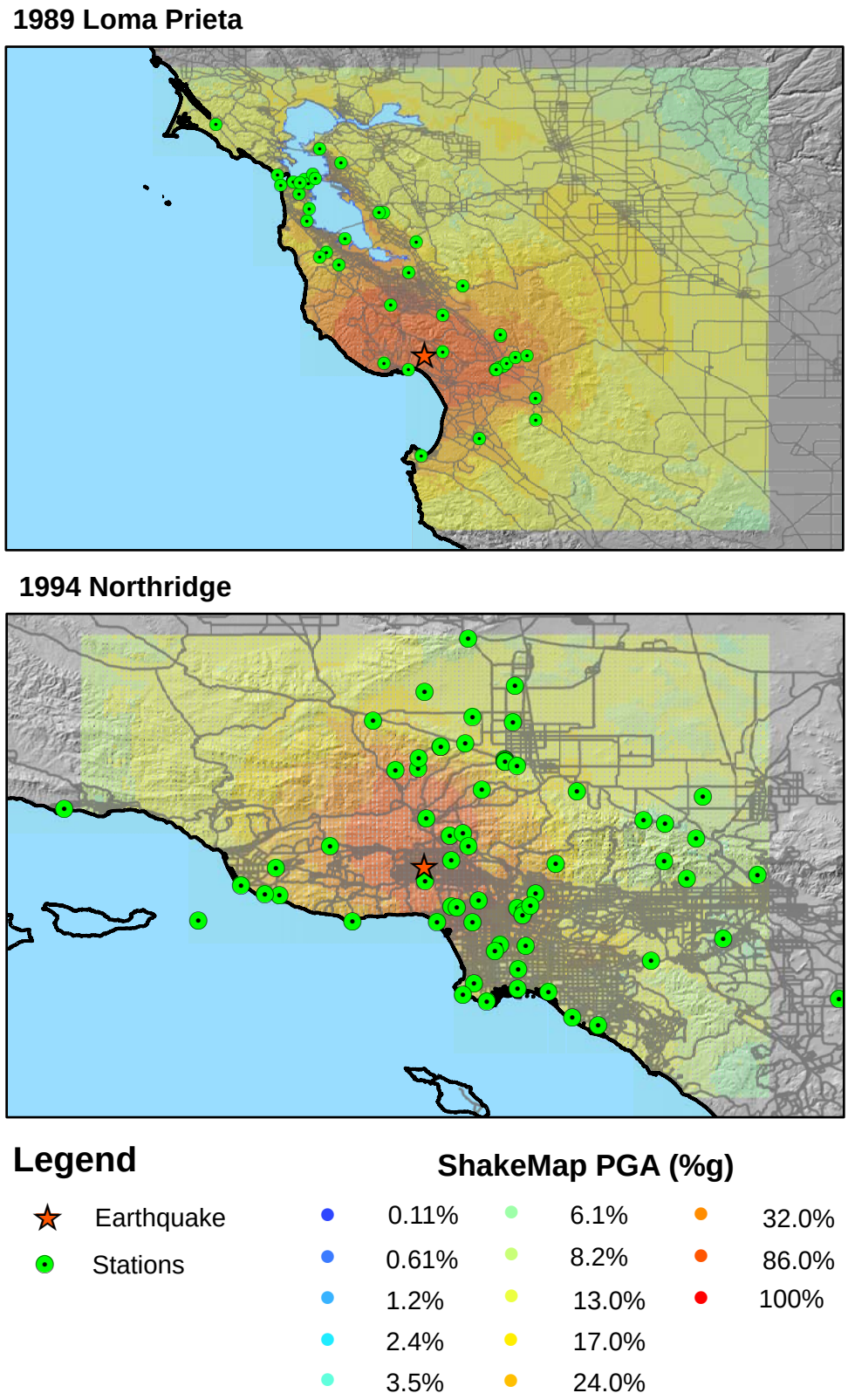


**Figure 1b.** Location of available strong motion recording stations and ShakeMap PGA models for the 1989 Loma Prieta (top) and 1992 Northridge (bottom) earthquakes.

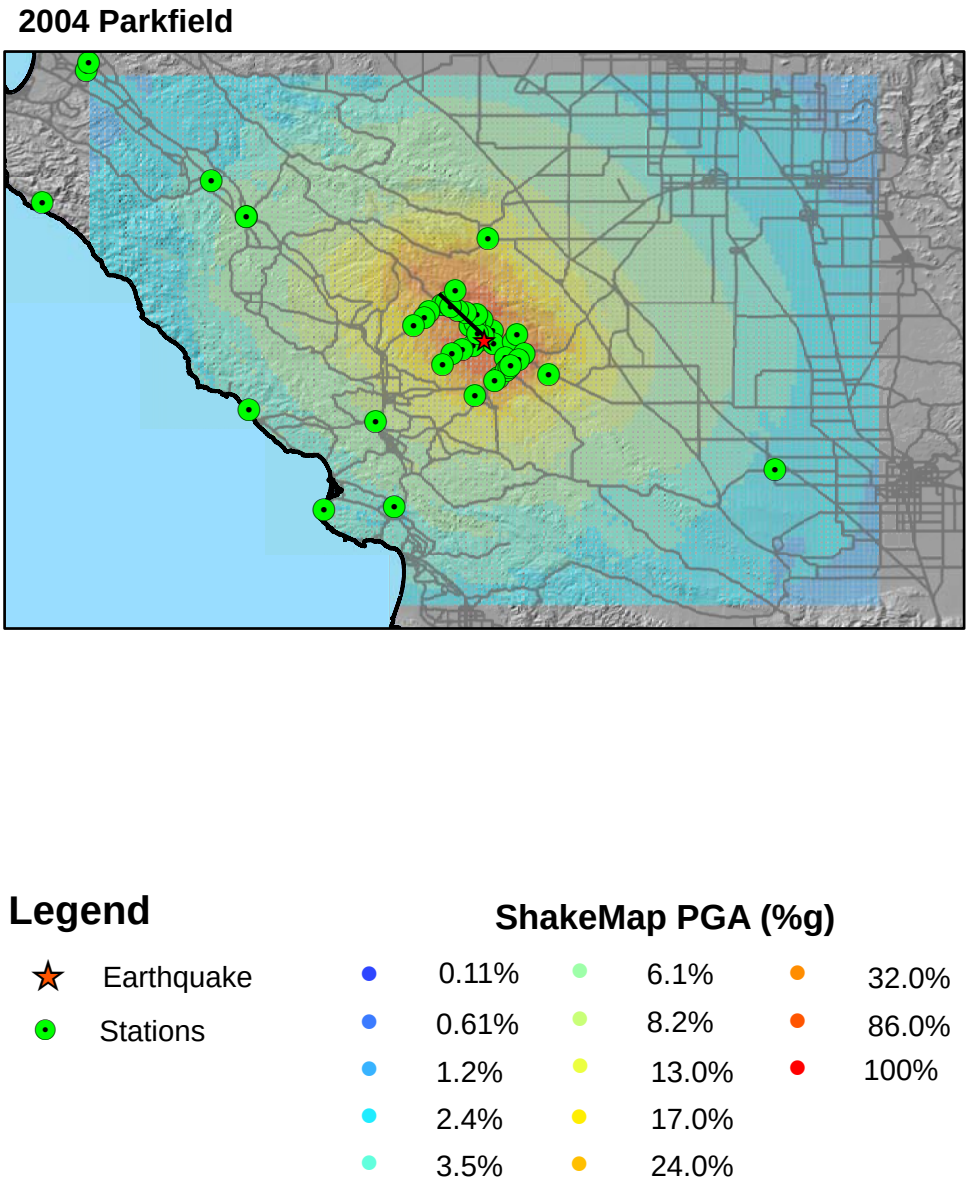


**Figure 1c.** Location of available strong motion recording stations and ShakeMap PGA models for the 2004 Parkfield earthquake.

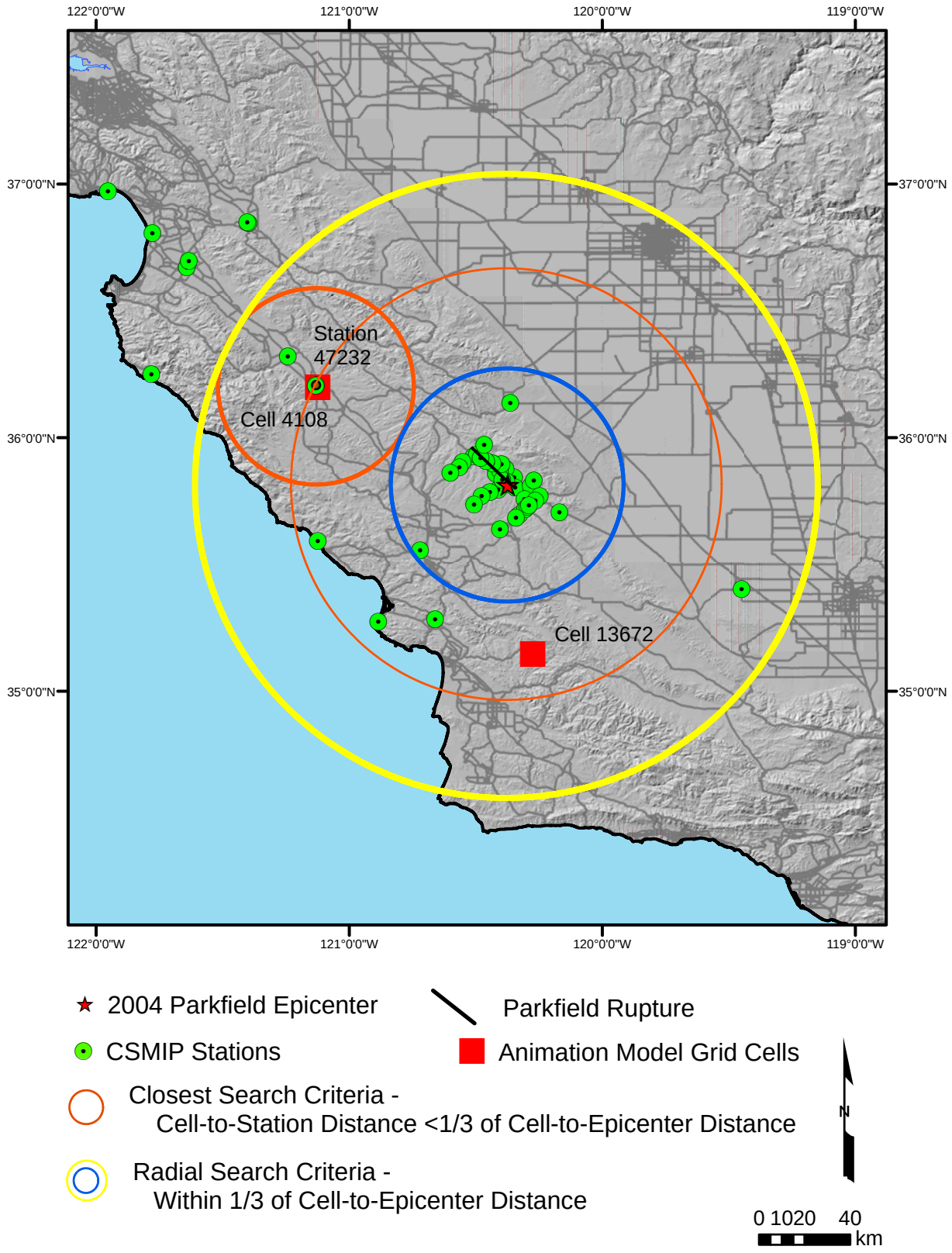


**Figure 2.** Schematic of 'Most Appropriate' Station Search Criteria

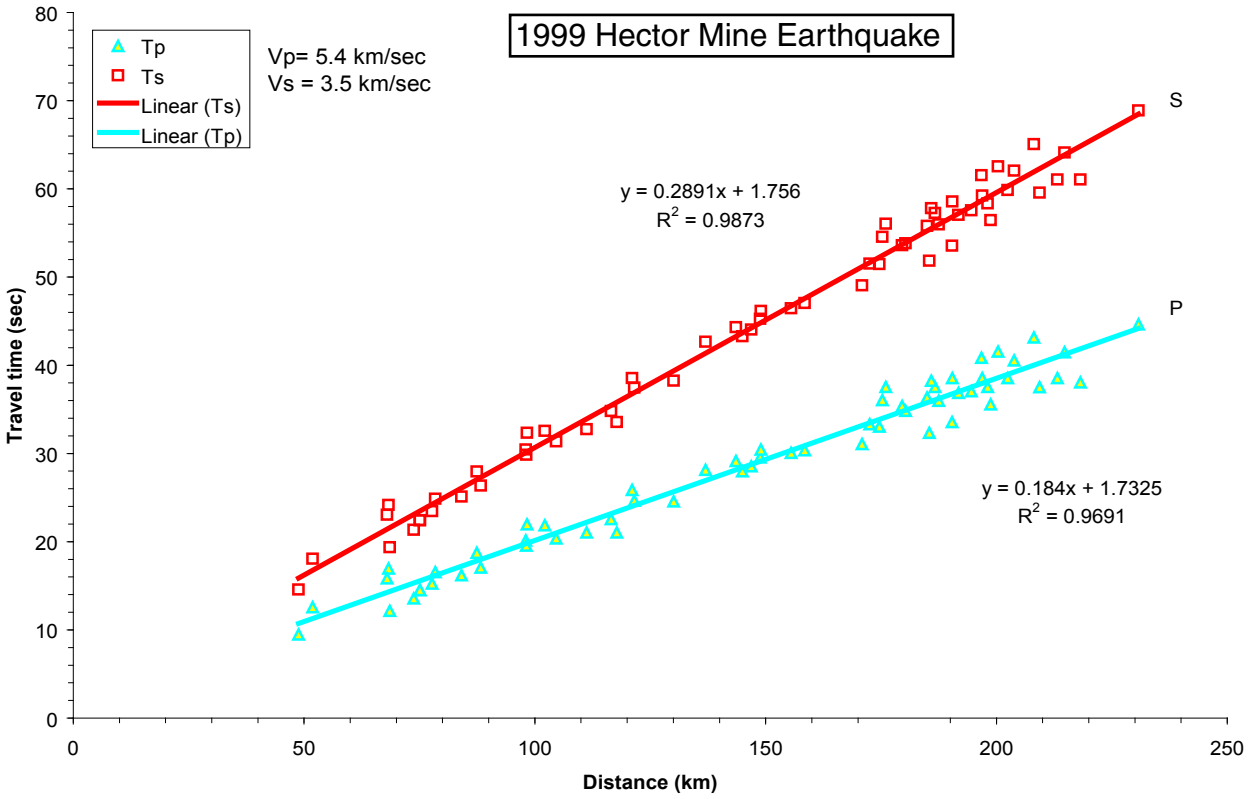


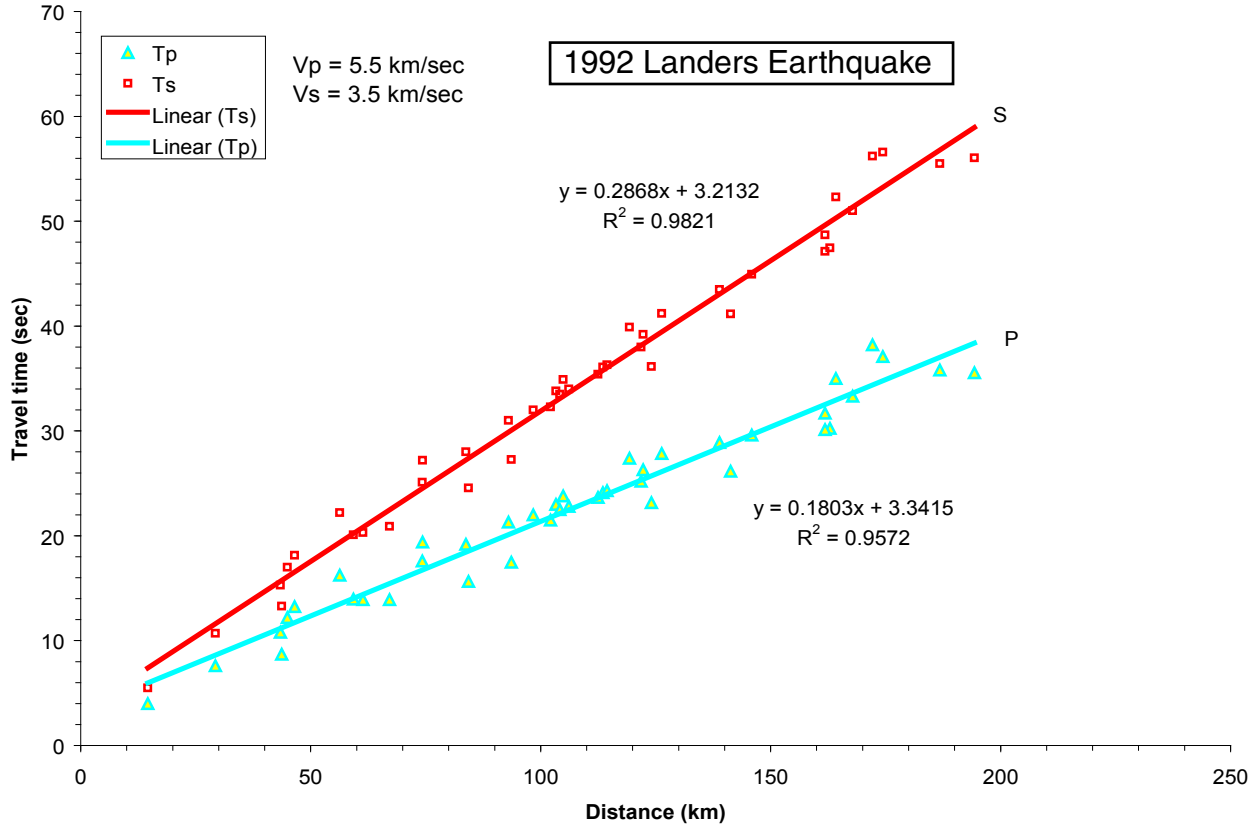


**Figure 3a.** P-wave and S-wave seismicity velocity travel times for the 1999 Hector Mine and 1992 Landers earthquakes

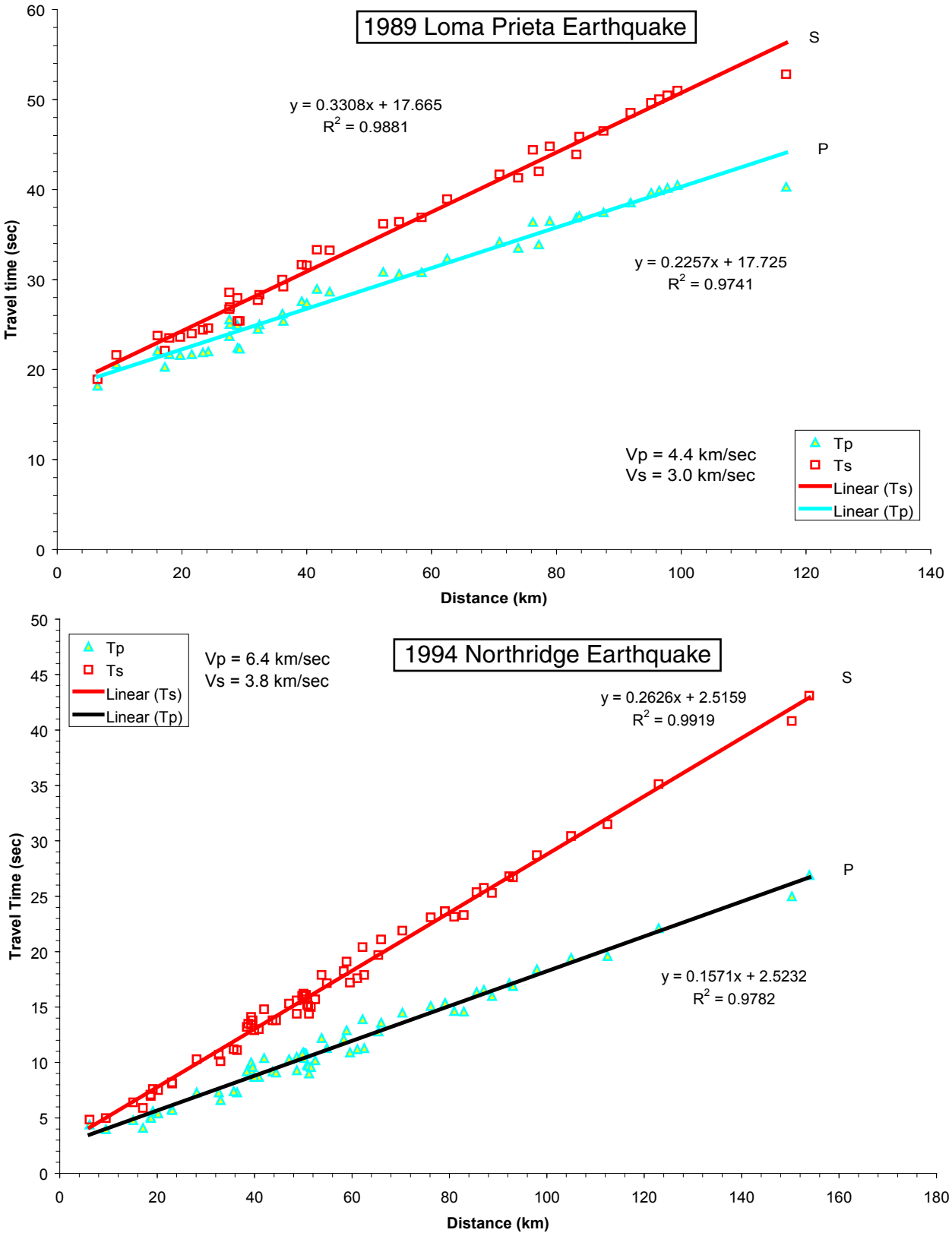


**Figure 3b.** P-wave and S-wave seismicity velocity travel times for the 1989 Loma Prieta and 1994 Northridge earthquakes

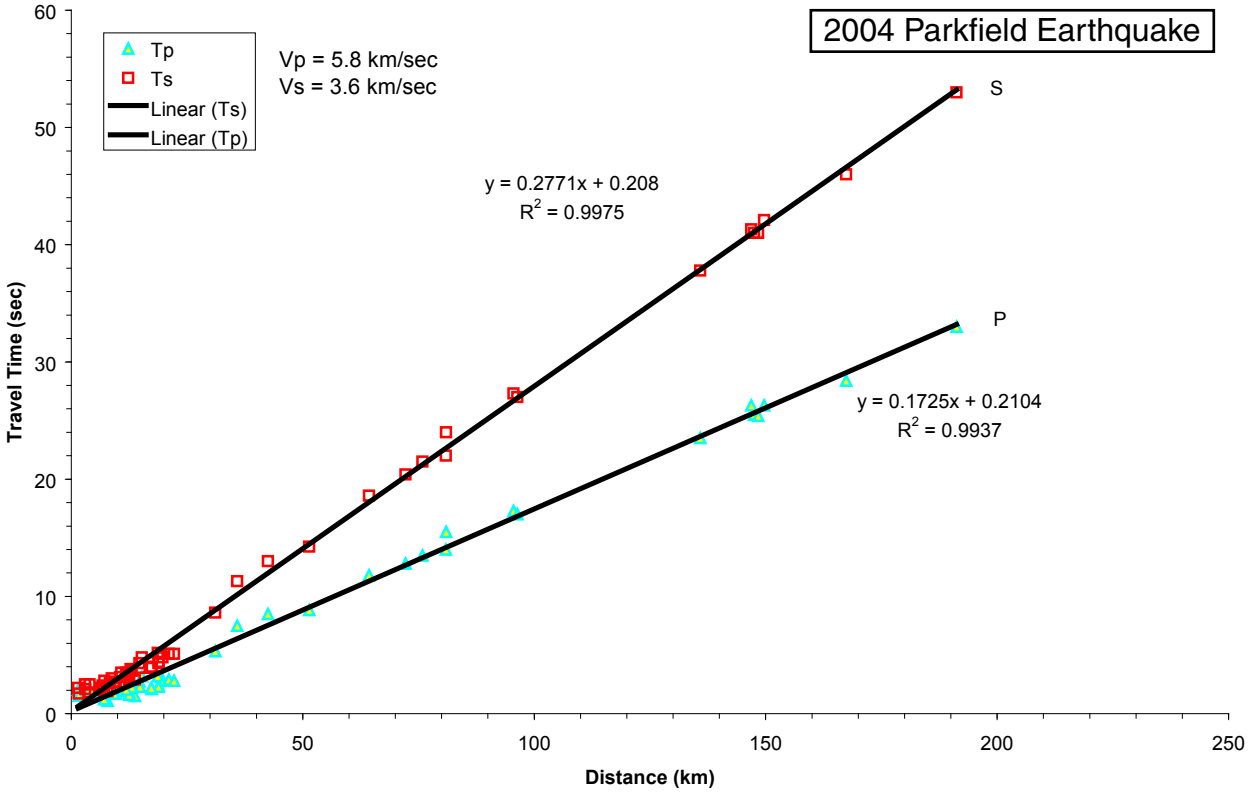


**Figure 3c.** P-wave and S-wave seismicity velocity travel times for the 2004 Parkfield earthquake

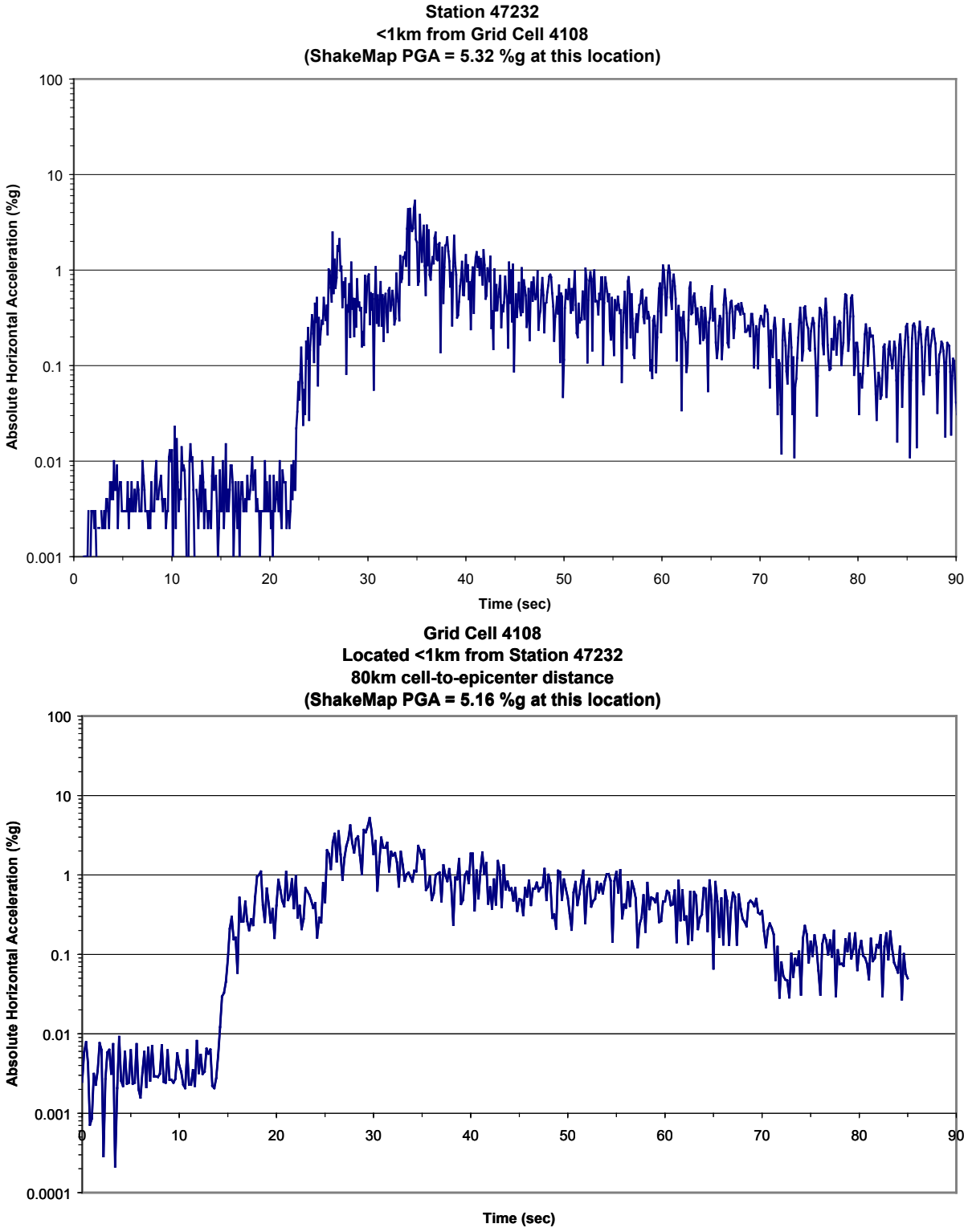


**Figure 4.** Comparison of recorded time history from Station 47232 to modeled time history for model grid cell 4108. (Refer to Figure 2 for locations)

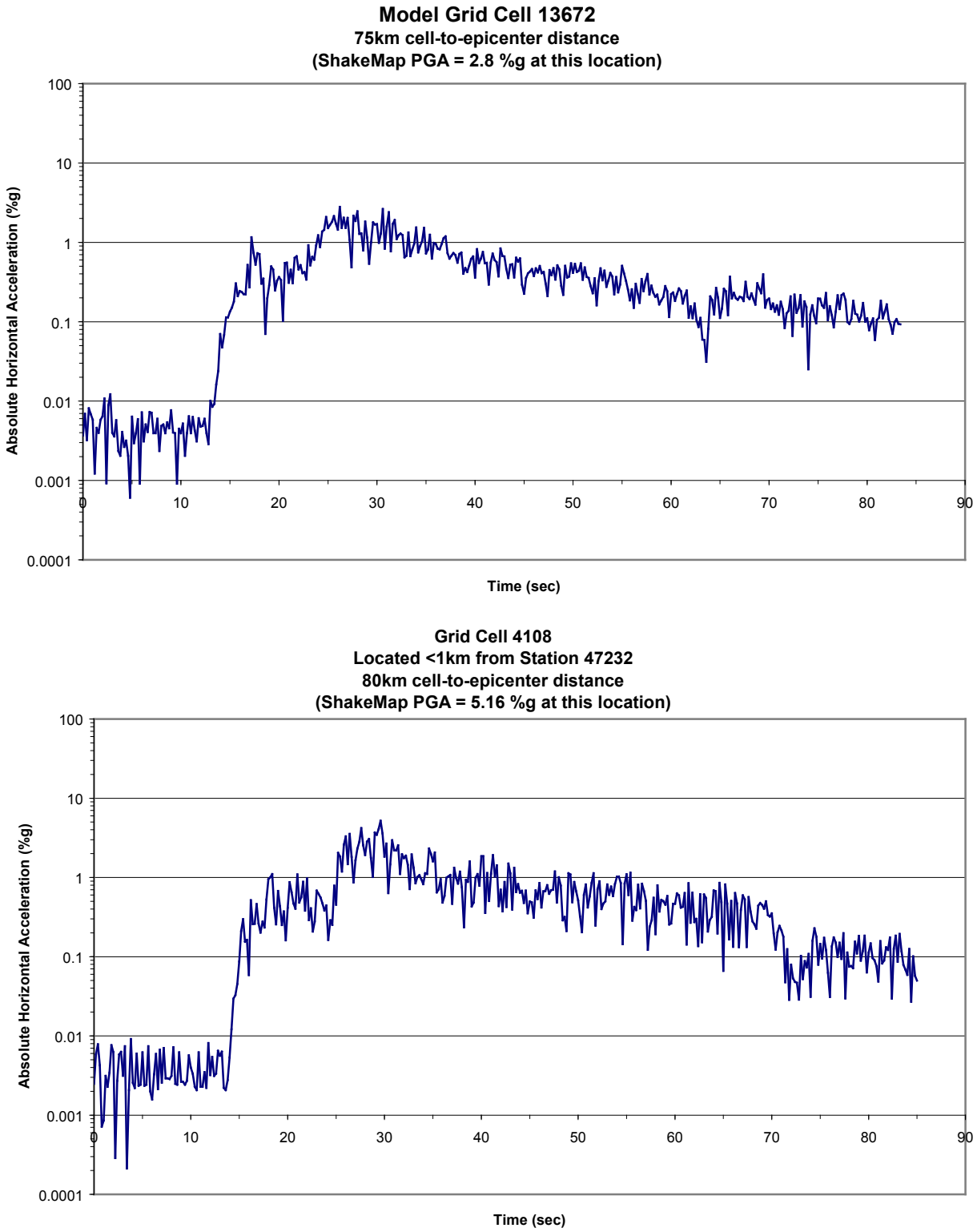


**Figure 5.** Comparison of modeled time histories for model grid cels 4108 and 13672. (Refer to Figure 2 for locations)

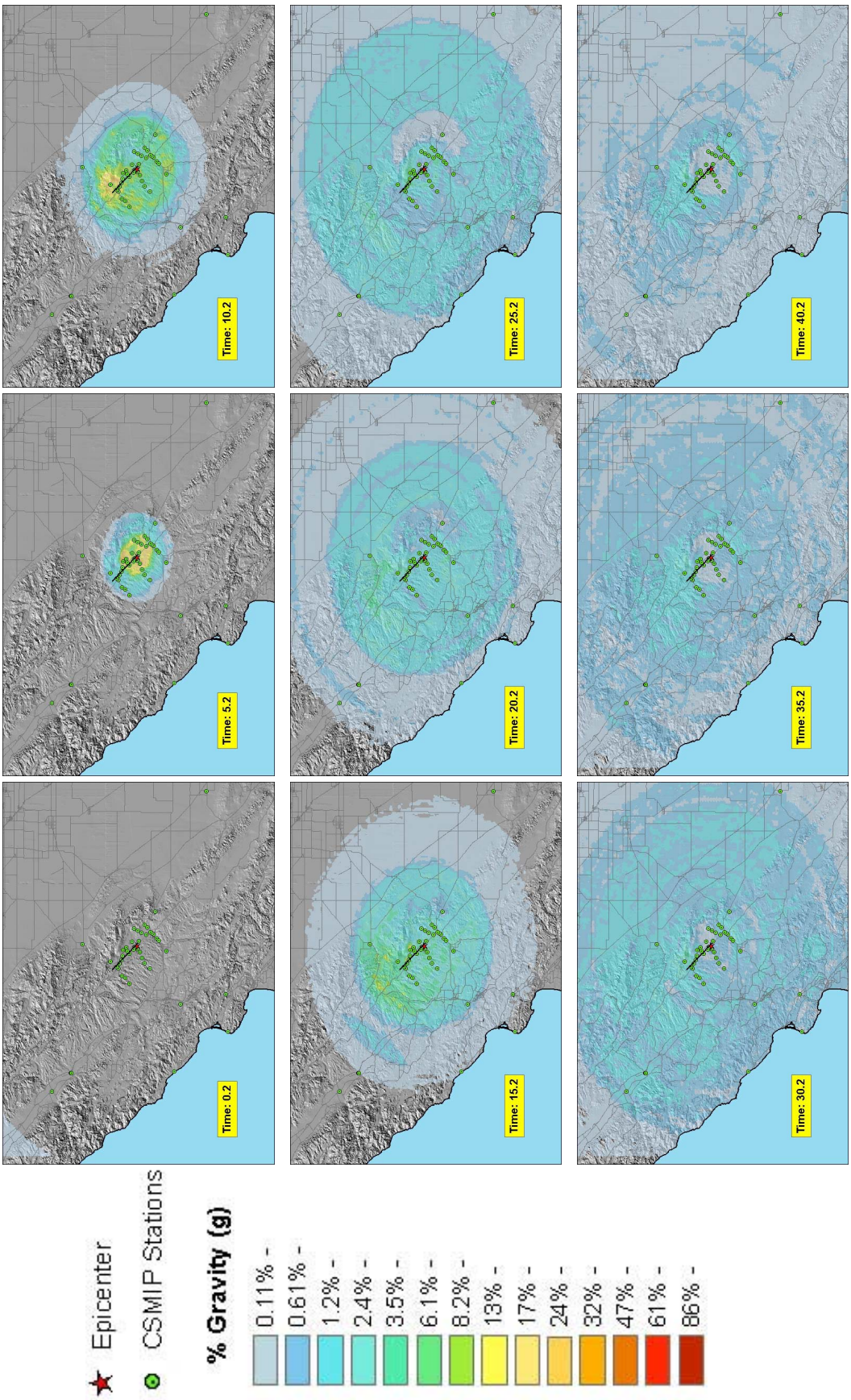


**Figure 6.** Time series of sequential map-still frames used to create the 2004 Parkfield animation.

# QUANTIFYING CISN SHAKEMAP UNCERTAINTY

Kuo-wan Lin[1], David J. Wald[2], Bruce Worden[3], and Anthony F. Shakal[1]

[1]California Geological Survey, Sacramento, CA
[2]U. S. Geological Survey, Golden, Colorado, CO
[3]U. S. Geological Survey, Pasadena, California, CO

## Abstract

Efforts underway to quantify uncertainties associated with ShakeMap ground motions through efforts by the California Integrated Seismic Network (CISN) ShakeMap Working Group are discussed. There are multiple sources of uncertainty in producing a ShakeMap, including sparse ground motion measurements, approximate representation of fault finiteness and directivity, empirical ground motion predictions, numerical interpolation, and site corrections. These ground motion uncertainty measures are critical for evaluating the range of possible losses and allow users to associate appropriate levels of confidence when using rapidly produced ShakeMaps as part of their post-earthquake critical decision making process. We quantify the uncertainties of the maps on a point-by-point basis, by combining the separate, but related, contributions of uncertainty for each ShakeMap parameter as a function of location on the map. Finally, we show examples of results of estimates of uncertainty for ShakeMap for earthquakes in California with/without defined fault traces. We discuss future developments and plans for integration of these uncertainty measures, both quantitative and qualitative, into the online system and user interfaces of ShakeMap.

## Introduction

The accuracy of a given ShakeMap varies spatially over the map area and depends on a number of contributing factors. However, it is usually dominated by two aspects: 1) spatial variability of peak ground motions near recording stations (and thus, station density), and 2) the aleatory uncertainty associated with empirical ground motion estimation relationships used to estimate the shaking between stations.

In this study, we consider these two sources of variability in estimating ShakeMap uncertainty. Spatial variability of peak ground motions can be generalized in the form of a rapidly increasing variability with increasing distance from the nearest station. Aleatory variability, in contrast, is more complicated and becomes more significant as the earthquake fault dimensions get larger (about M5.5 and greater), particularly when the fault location and dimensions are not yet ascertained. Without an accurate representation of the fault rupture geometry, the appropriate distance to a particular location—which is needed when using a forward ground motion prediction equation—is poorly constrained. Not knowing the true distance to the fault rupture contributes significant uncertainty, particularly in the near-fault region.

Our goal in quantifying ShakeMap uncertainty is to produce a grid of latitude and longitude pairs which contains not only the various peak ground motion parameters at each point, but also contains the variance at that point for each ground motion parameter. This grid could also be converted to an overall *qualitative* assignment of ShakeMap accuracy, an issue we will be addressing in the near future.

In the meantime, methods of estimating uncertainty in three end member cases are described for generating a map of ShakeMap uncertainty values at each grid point.

**Case 1. Small To Moderate Sized Earthquake, Suitable For A Point Source Representation**

When a grid point is near to a station (~10 km or less) uncertainty is controlled by proximity to that station and the variability can be quantified by the model of Boore et al. (2003):

$$\sigma^2_{\Delta \log Y} = \sigma^2_{indobs}(1+\frac{1}{N})F(\Delta)^2 \text{ and } F = 1 - e^{-\sqrt{0.6\Delta}}, \qquad (1)$$

where $\sigma_{\Delta \log Y}$ is the standard deviation of differences in the logarithm of the peak motion $Y$ (e.g., acceleration), $\sigma_{indobs}$ is the standard deviation of an individual observation about a regression, and $N$ is the number of recordings used in averaging the peak motion of a group of recordings in a small area. $F(\Delta)$ is a function that models the spatial correlation of the motion, where $\Delta$ is the distance between the two points. For this study we assume that $N$ is large enough so that the *1/N* term can be neglected. Thus, the predicted spatial variability in ground motion reduces to zero as the distance between a grid point and the nearest station decreases to zero as shown in Figure 1 (from Boore et al., 2003). With a large grid point to station distance, the spatial variability in ground motion approaches the standard deviation of the regression model. The cut-off distance for computing spatial variability in ground motion is set at 10 km in this study.

For greater distances than 10 km, we use the Boore et al. (1997) ground motion prediction equation's total aleatory uncertainty ($\sigma_{Aleatory}$).

$$\sigma_{Aleatory} = \sqrt{\sigma^2_{Interevent} + \sigma^2_{Intraevent}} \qquad (2)$$

With several ShakeMap data points (i.e., station amplitudes), we can remove a bias term between the ground motion predictions and the data, thereby removing the inter-event term. However, when no data are available, no event-specific bias correction can be made and both the intra- and inter-event terms contribute (Table 1).

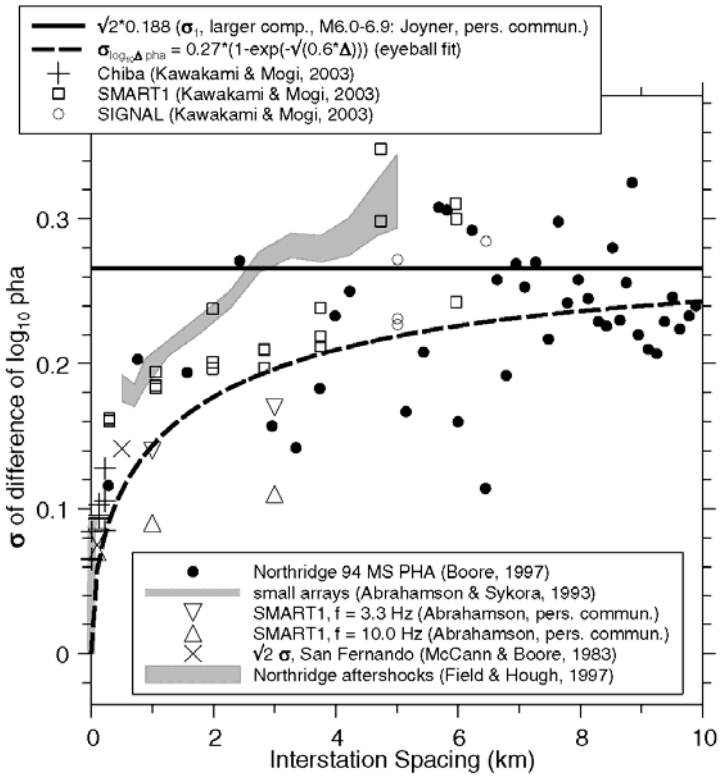


Figure 1. Standard deviation of difference of the largest peak horizontal acceleration as a function of interstation spacing. F(Δ) given in equation 1 is shown by the curve. Data include Northridge earthquake strong motions (Boore, 1997) and previous studies as indicated (figure from Boore et al., 2003).

### Case 2. Large Earthquake, And Fault Rupture Geometry And Dimensions Are Not Known

For earthquakes of magnitude 5.5 and larger, the fault dimension affects the measure of distance from the fault to the site of interest. When employing the Joyner-Boore distance measure used for forward ground motion estimation, the fault rupture dimension must be known, since the Joyner-Boore distance is defined as the closest distance from a site to the surface projection of the fault rupture.

If necessary, initial ShakeMaps are produced without knowledge of the rupture dimensions. Again, the uncertainty is generally low near the seismic stations, but at some distance from the stations it is constrained only by the predictions using a ground motion attenuation relationship. In this case, distance adjustments are made to convert the point source (epicentral) distance to the appropriate Joyner-Boore distance for the ground motion attenuation model used. We also must adjust the aleatory uncertainty. We adopt the results and the approach defined in EPRI (2003), in which the distance adjustment is determined for the case where the rupture orientation is assumed to be uniformly distributed in azimuth from 0 to 360 degrees and for a mixture of strike-slip and reverse ruptures using random epicenters. For each simulated rupture, EPRI (2003)

i) Computed the appropriate distance measure and corresponding median ground motion parameter,
ii) Considered the geometric mean of all these simulation values to be the median ground motion for that epicentral distance and magnitude,
iii) Inverted the median ground motion to find the distance that corresponds to that median ground motion value,
iv) Determined a distance adjustment factor for each epicentral distance, magnitude, and ground motion parameter, and
v) Fit these distance adjustment factors with a functional form, and provided the necessary coefficients in a series of look up tables.

Using the distance correction factor then simply entails employing these distance adjustment relationships (EPRI, 2003) that translate epicentral to the equivalent Joyner-Boore distance:

$$r_{Joyner-Boore} = r_{Epicentral} \times \{1 - 1/\cosh(C_1 + C_2(M-6) + C_3 \ln(r'))\}, \quad (3)$$

where $r' = \sqrt{r_{Epicentral}^2 + h^2}$ (4), and $h = e^{C_4 + C_5(M-6)}$, (5)

$r_{Joyner-Boore}$ is the Joyner-Boore distance, $r_{Epicentral}$ is the epicentral distance, $M$ is the magnitude of the earthquake, and $C_1$ to $C_5$ are model coefficients (which vary by ground motion model and seismic frequency) given in Table 2.

Hence, when the fault geometry and orientation is not known, a mean value of ground motion at each point is provided rather than the simple epicentral distance-based estimation. While the latter approach is currently used for ShakeMap, it tends to underestimate ground motions near a finite fault (since it is the maximum possible source-station distance) rather than providing a mean value based on random fault geometry and epicenter. Hence, we will be adopting these distance adjusted ground motions for ShakeMap calculations in the near future.

The variability associated with this approach is also derived in EPRI (2003). The variability in the median ground motion due to the randomness in epicenter location and rupture orientation was used to compute a ground motion standard deviation, and we employ their equations to compute the additional component of aleatory uncertainty:

$$\sigma_{AdditionalPointSource} = e^{C1+C2(M-6)+C3(M-6)^2} \times [1 - 1/\cosh(f_a)] \times 1/\cosh(f_b), \quad (6)$$

$$f_a = e^{C4+C5(M-6)} + e^{C6+C7(M-6)} \times r_{Epicentral}, \quad (7)$$

$$f_b = e^{C8+C9(M-6)} \times \ln(r'/h), \quad (8)$$

$$r' = \sqrt{r_{Epicentral}^2 + h^2}, \; h = e^{C10+C11(M-6)}, \quad (9)$$

where $\sigma_{AdditionalPointSource}$ is the point source aleatory, $r_{Epicentral}$ is the epicentral distance, $M$ is the magnitude of the earthquake, and $C_1$ to $C_{11}$ are the model coefficients (see Table 3).

We can then combine this additional point source variability (Equation 6) with that associated with the prediction equation (Equation 2):

$$\sigma_{Total} = \sqrt{\sigma^2_{Aleatory} + \sigma^2_{AdditionalPoint Source}} \tag{10}$$

Again, if at any time a grid point is closer to a station than 10 km, the variability associated with that grid to station distance controls the uncertainty; at greater distances, the above relation is employed (Figure 2).

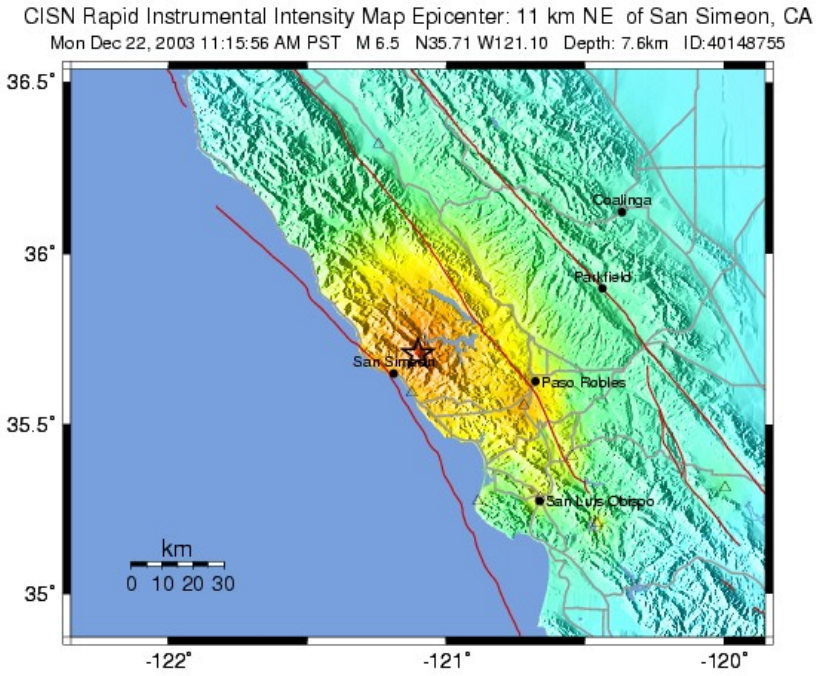


Figure 2a. ShakeMap for the magnitude 6.5 San Simeon, California earthquake of 2003, Case 2. Note there are few seismic stations.

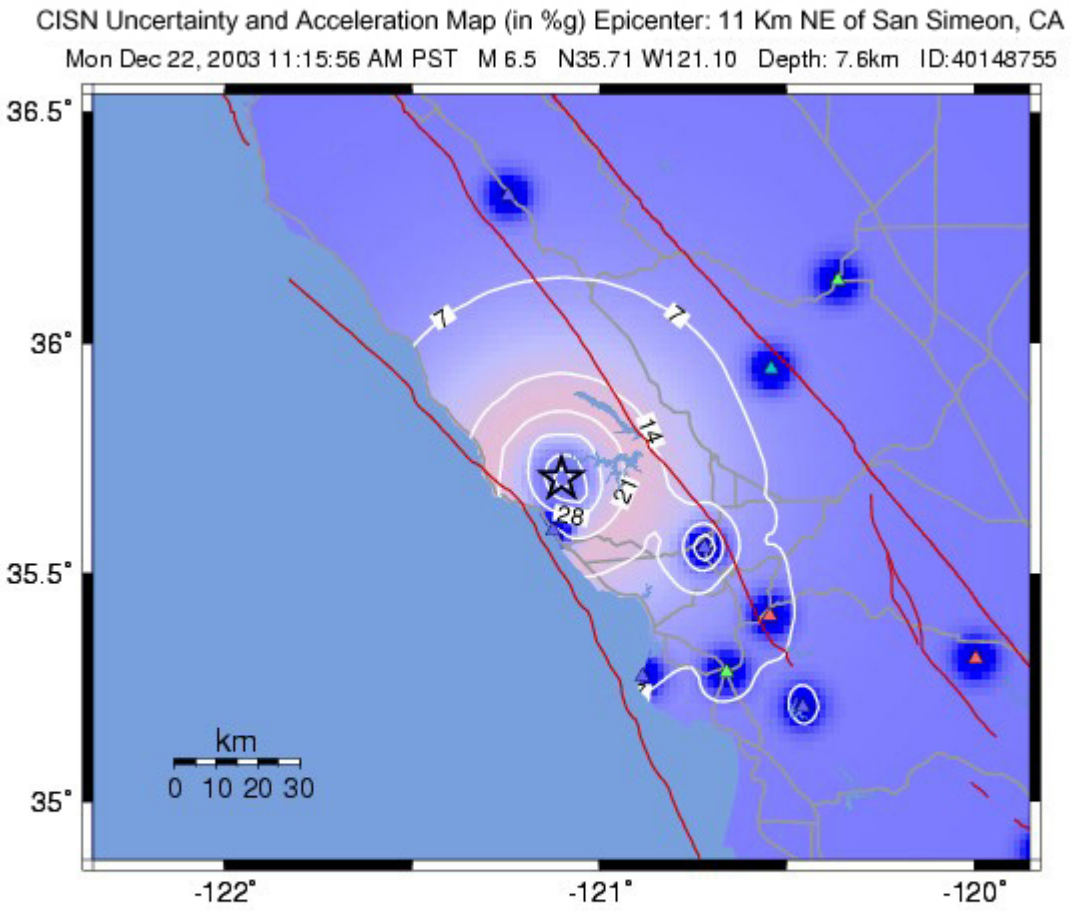


| Quality | A | B | C | D | E |
|---|---|---|---|---|---|
| Accuracy | Very High | High | Moderate | Low | Very Low |
| Uncertainty (Sigma) $Log_{10}$ Values | 0.0 | 0.1 | 0.2 | 0.3 | 0.5 |

Figure 2b. Uncertainty map, prior to adding finiteness, indicating linear units of standard error above the aleatory uncertainty (red areas) and below (dark blue, near stations). The ring of large uncertainty around the epicenter is a result of early uncertainty of the fault location and thus the uncertainty for computing distances to the fault.

### Case 3. Large Earthquake, And Fault Finiteness Is Constrained

After a description of the source becomes available—usually from some combination of source modeling, aftershock patterns, or surface rupture—we can fall back on the approach of Case 1, since the appropriate Joyner-Boore distance measure from the fault location can be determined. As in case 1, uncertainty is determined by the grid-to-station proximity uncertainty (Equation 1) or if there are no nearby observations, the uncertainty associated with the predictive relationship (Equation 2). Typically by this time, enough seismic stations are available that a bias between the data and the ground motion estimates can be computed and thus the inter-event uncertainty term is dropped (Figure 3).

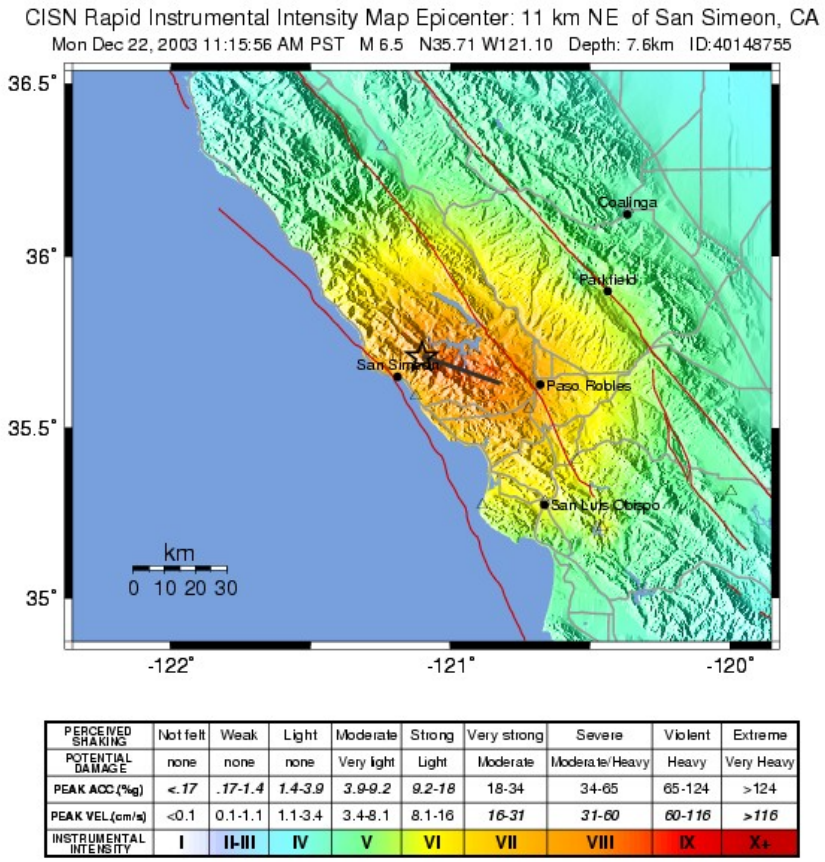


Figure 3a. ShakeMap for the magnitude 6.5 San Simeon, California earthquake of 2003 with fault finiteness imposed, Case 3 (line source shown as a grey line).

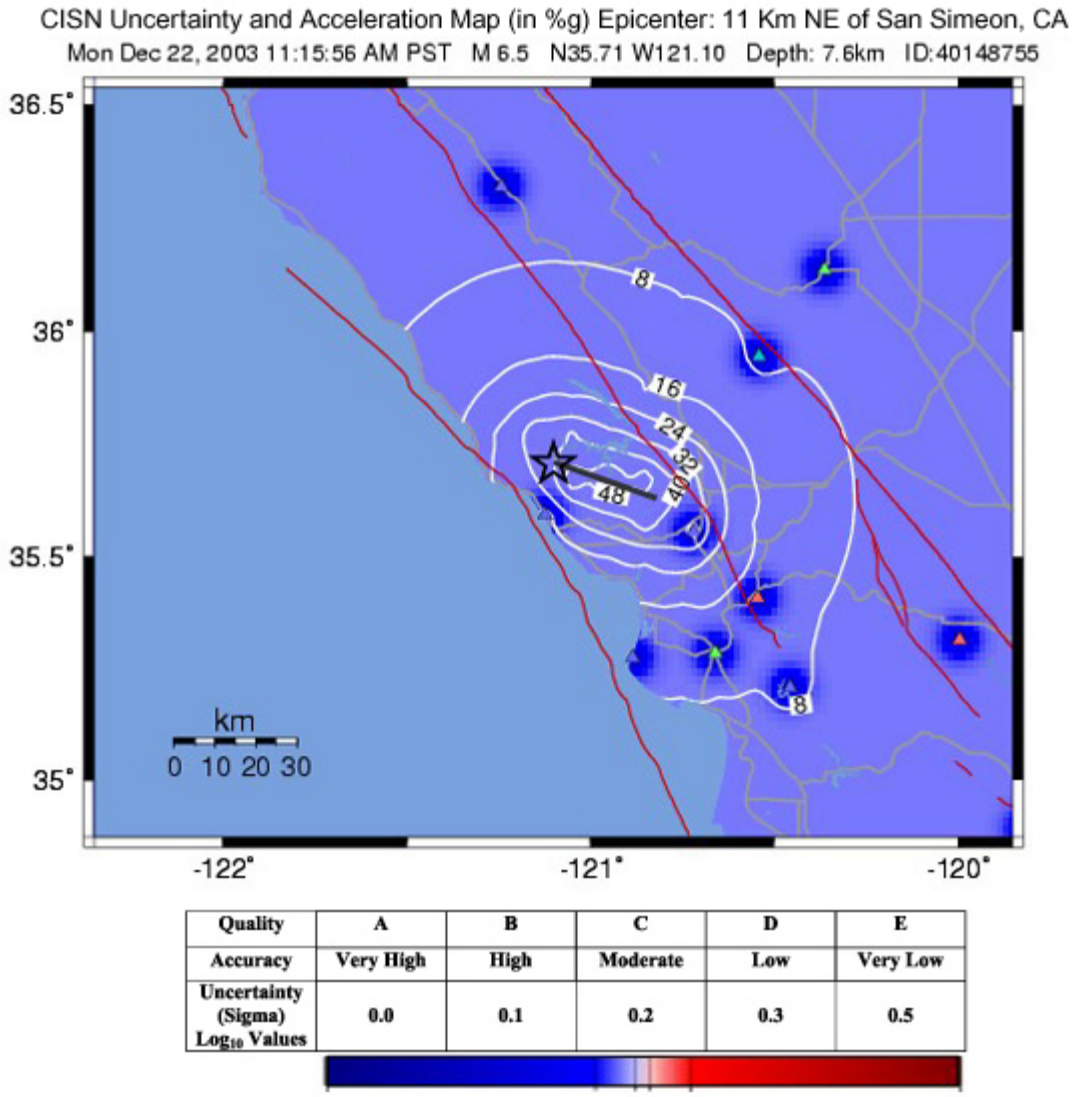


Figure 3b. Uncertainty map, after adding fault finiteness, indicating linear units of standard error above the aleatory uncertainty (red areas) and below (dark blue, near stations).

### Analysis of Spatial Variability of PGA for the M6 Parkfield Earthquake

In order to validate the effectiveness of the method for quantifying CISN ShakeMap uncertainty, we analyzed the spatial variability of PGA data from the 28 September 2004 Parkfield earthquake and compared differences between observed and estimated PGA values. The Parkfield array data recorded by the CISN during the M6 earthquake provided the highest density of recording stations in the near-fault region of any earthquake recorded to date (e.g., Langbein et al., 2005; Shakal et al., 2005). A total of 56 stations were located within 20 km of

the fault; 48 were within 10 km of the fault, more than for many other earthquakes combined. The distances between stations ranged from <1 to 40 km. It is of interest to study the spatial variability of peak ground motions across the Parkfield array and to examine dependence of variability on nearest distance-to-fault and on sensor orientation. To do this, we have followed the analysis approach of Boore et al. (2003).

The distances between all possible stations pairs were calculated and sorted in increasing order. These sorted pairs were grouped into bins with 15 station pairs per bin, and over station-pair spacings of up to 20 km. For each bin we computed mean station spacing $\Delta$ and standard deviation $\sigma(\Delta)$ of differences in logarithm of PGA. The spatial variability of standard deviation for the Parkfield earthquake (Figure 4) is consistently higher at most station spacings than that for both the Northridge and San Simeon earthquakes, and higher (by a factor of ~1.3) than the standard deviation for the regression model. The standard deviation value increases rapidly from ~0.2 at 1.2 km station spacing, to ~0.3 at 2.0 km station separation.

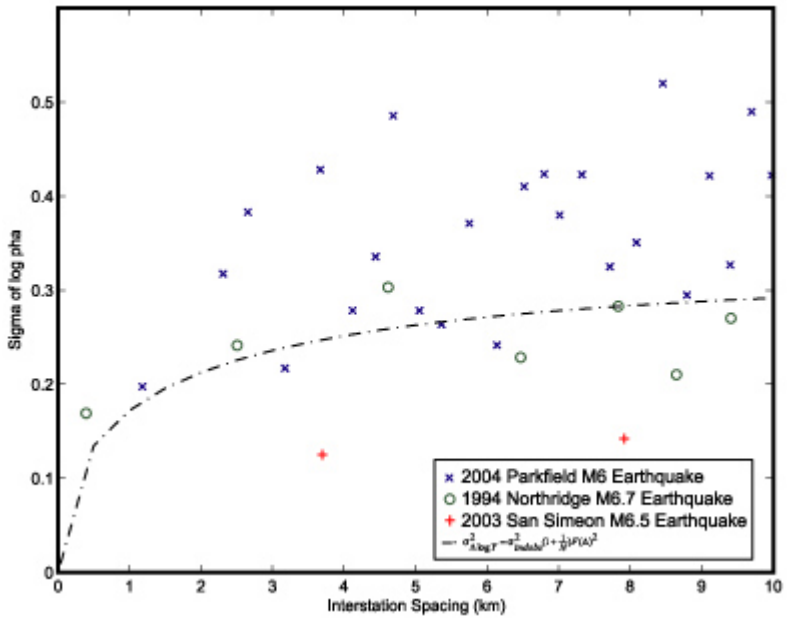


Figure 4. Standard deviation of difference of the largest peak acceleration as a function of interstation spacing. $F(\Delta)$ given in equation 1 is shown by the curve. Data include strong motion records from the Parkfield, Northridge, and San Simeon earthquakes.

To examine any dependence of the variability on sensor orientation, we divided the data to contain only East-West or North-South components and repeated the same procedure. For dependence on nearest distance-to-fault, the data was divided into near-fault/away-from-fault stations with a cut-off nearest distance-to-fault of 12 km. Figure 5 shows the results for spatial variability in standard deviations for both analyses.

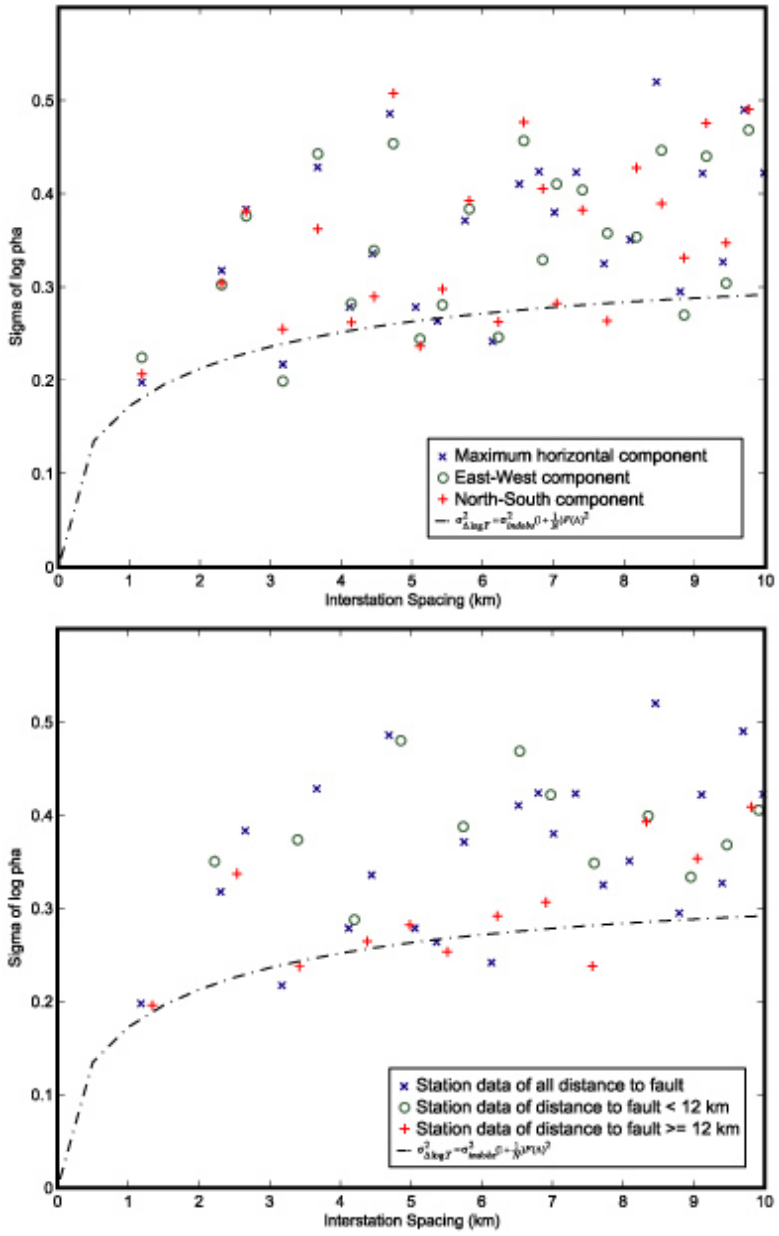


Figure 5. Standard deviation of difference of log of the peak acceleration as a function of interstation spacing for the Parkfield earthquake. (Top) Standard deviation for data with either East-West of North-South component of the strong motion data. (Bottom) Standard deviation for data either within or beyond a distance of 12 km to nearest fault.

We found that spatial variability for the Parkfield data with respect to the orientation of recording components (Figure 5) shows similar results to standard deviations obtained with analysis using the larger of the horizontal components. Contrary to direction insensitivity of spatial variability, we observed better correlation of peak ground motions for distant station pairs than for the close station pairs (Figure 5). The estimated variability of peak ground motions for distant station pairs approximates the standard deviation of the regression model.

The results of spatial variability for the Parkfield array data represent a special case compared with other earthquake data sets because Parkfield has many near-fault stations and relatively few at distance. The highly variable standard deviations in the near-fault data can be attributed to the complexity of near-fault ground motions, which are not accounted for by the regression model and will require further investigation.

We also compared observed peak values of strong ground motion for the Parkfield earthquake with estimated peak values to analyze the extent of data misfit for the two regression models currently used by the CISN ShakeMap, the HazusPGV (Southern California) and the Large_Seg (Northern California). (Note that the peak values of model estimates were not adjusted for site condition and do not coincide with the results of the CISN ShakeMap.) Both regression models use forms similar to the regression model of Boore et al., 1997 (BJF97). The models generate PGA, PGV, and SA for a given magnitude and distance.

Figure 6 shows results of comparison of the observed PGA recorded by the CISN network and the estimated values, based on the Southern California and Northern California regression models, for the 2004 Parkfield earthquake. The estimated PGA values from both regression models are consistently higher than the observed values at low PGA range (less than ~0.2g). However, the estimated values are lower than the observed values at high PGA range (greater than ~0.5g).

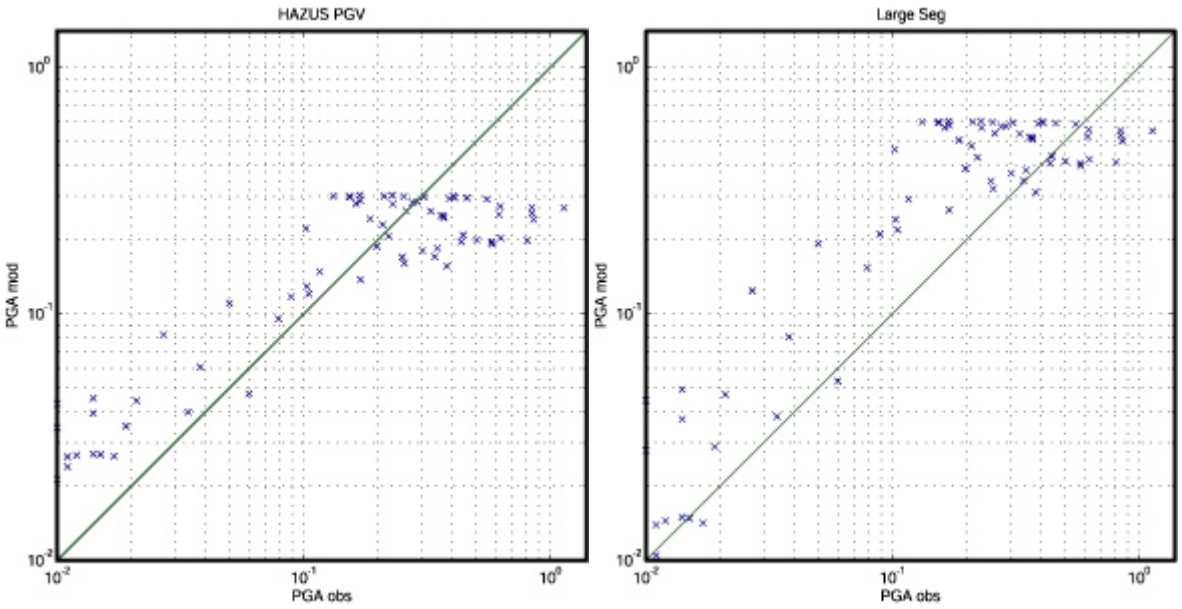


Figure 6. Comparison of the PGA recorded by the CISN network and the estimated values based on either (left) Southern California or (right) Northern California regression model for the 2004 Parkfield earthquake.

## Summary

Quantifying ShakeMap uncertainty is an ongoing development at CISN as growing expectations of the use of the maps continue. The next version of ShakeMap (V3.1) is nearing

release, and should be available in mid-2005. The new features in the release include the underlying code for quantification of uncertainty, for testing and feedback, and the implementation of an XML file for the distribution of the gridded ShakeMap data.

The three end member cases described here will be used in quantifying ShakeMap uncertainty: (1) small earthquake of M5.5 or less as point source representation, (2) large earthquake without known fault rupture geometry and dimensions, and (3) large earthquake with fault finiteness. Using one of these methods, the goal is to produce a grid of latitude and longitude pairs containing peak ground motion parameters and uncertainty at each point.

Results from a study of spatial variability of the Parkfield earthquake data indicate that the variability is generally direction insensitive and approximately corresponds with model predictions for distant stations. In the near-fault area the variability is complex and cannot be accounted for by the standard deviation from the regression model.

## References

Boore, D. M. (1997). Estimates of average spectral amplitudes at FOAKE sites, Appendix C in An evaluation of methodology for seismic qualification of equipment, cable trays, and ducts in ALWR plants by use of experience data, K. K. Bandyopadhyay, D. D. Kana, R. P. Kennedy,and A. J. Schiff (Editors), U.S. Nuclear Regulatory Commission NUREG/CR-6464 and Brookhaven National Lab BNL-NUREG-52500, C-1-C-69.

Boore, D. M., W. B. Joyner, and T. E. Fumal, (1997). Equations for Estimating Horizontal Response Spectra and Peak Acceleration from Western North American Earthquakes: A Summary of Recent Work, *Seismological Research Letters*, Volume 68, Number 1, January/February 1997.

Boore, D M., Gibbs, J. F., Joyner, W. B., Tinsley, J. C., and Ponti, D. J (2003). Estimated Ground Motion From the 1994 Northridge, California, Earthquake at the Site of the Interstate 10 and La Cienega Boulevard Bridge Collapse, West Los Angeles, California, *Bull. Seism. Soc. Am*, 93, 6, 2737-2751.

EPRI (2003). CEUS Ground Motion Project: Model Development and Results, EPRI Report 1008910, EPRI, Palo Alto, CA, 105 pp.

Field, E. H., and S. E. Hough, (1997). The variability of PSV response spectra across a dense array deployed during the Northridge aftershock sequence, *Earthquake Spectra*, **13**, 243-257.

Hok, S., and D. J. Wald, (2003). Spatial Variability of Peak Strong Ground Motions: Implications for ShakeMap Interpolations, *EOS. Trans. AGU*, 84(46), F1121.

Langbein, J., R. Borcherdt, D. Dreger, J. Fletcher, J.L. Hardebeck, M. Hellweg, C. Ji, M. Johnston, J.R. Murray, R. Nadeau, M.J. Rymer, and J.A. Treiman, (2005). Preliminary report on the 28 September 2004, M 6.0 Parkfield, California earthquake, *Seism. Res. Lett.*, **76**, 1, 10-26.

Shakal, A., V. Graizer, M. Huang, R. Borcherdt, H. Haddadi, K. Lin, C. Stephens, and P. Roffers, (2005). Preliminary analysis of strong-motion recordings from the 28 September 2004 Parkfield, California earthquake, *Seism. Res. Lett.*, **76**, 1, 27-39.

| | PGA | PGV | PSA03 | PSA10 | PSA30 |
|---|---|---|---|---|---|
| HazusPGV (SC) | 0.2258 | 0.2423 | 0.2267 | 0.2662 | 0.2918 |
| Large_Seg (NC) | 0.3606 | 0.3286 | undef | undef | undef |

Table 1. Standard deviation (aleatory) values (log10) for both Northern and Southern California regression models for the CISN ShakeMap.

| Frequency (Hz) | $C_1$ | $C_2$ | $C_3$ | $C_4$ | $C_5$ |
|---|---|---|---|---|---|
| 0.5 | -0.4098 | -1.394 | 1.003 | 1.235 | 1.421 |
| 1.0 | -0.4060 | -1.394 | 1.003 | 1.237 | 1.424 |
| 2.5 | -0.4066 | -1.394 | 1.003 | 1.235 | 1.426 |
| PGA | -0.4517 | -1.394 | 1.003 | 1.239 | 1.431 |





Table 2. Distance adjustment from epicentral to Joyner-Boore distance coefficients for equations 3 and 5 (random epicenters) [from Table 3-38 of EPRI (2003)].

| Frequency (Hz) | $C_1$ | $C_2$ | $C_3$ | $C_4$ | $C_5$ | $C_6$ | $C_7$ | $C_8$ | $C_9$ | $C_{10}$ | $C_{11}$ |
|---|---|---|---|---|---|---|---|---|---|---|---|
| 0.5 | -1.502 | 0.5506 | -0.03874 | -0.8330 | -0.01935 | -1.341 | -0.6375 | -0.1008 | 0.3328 | 1.564 | 1.635 |
| 1.0 | -1.604 | 0.6415 | -0.05674 | -0.8626 | -0.01209 | -1.177 | -0.7274 | -0.1472 | 0.4290 | 1.722 | 1.635 |
| 2.5 | -1.430 | 0.5386 | -0.03777 | -0.7968 | -0.04394 | -1.378 | -0.6413 | -0.1241 | 0.3472 | 1.607 | 1.630 |
| PGA | -1.407 | 0.5926 | -0.05345 | -0.8708 | -0.001605 | -1.305 | -0.7161 | -0.1846 | 0.3675 | 1.599 | 1.629 |

Table 3. Additional aleatory variability (random epicenters) coefficients for equations 6-9 [from Table 3-42 of EPRI (2003)].

# VISUALIZATION OF NONLINEAR SEISMIC BEHAVIOR OF THE INTERSTATE 5/14 NORTH CONNECTOR BRIDGE

Robert K. Dowell

Department of Civil and Environmental Engineering
San Diego State University

## Abstract

This paper discusses modifications to the existing bridge visualization program, previously developed by the author, to properly include nonlinear behavior of the 5/14 North Connector bridge expected from future, severe, design-level earthquake motions. Such modifications recognize that nonlinear behavior will develop at predetermined column locations, based on current state-of-the-art seismic design practice. For single-column-bent bridges, plastic hinges are expected to develop at the base of the column in transverse bending and at both ends of the column under longitudinal loading. The bridge can now be viewed in full 3-D animation, developing plastic hinges at all critical locations and showing color-coded damage or ductility levels for transverse and longitudinal behavior for each bridge column. Spline functions were modified from cubic equations representing elastic member response to a combination of plastic and elastic responses.

## Introduction

The existing bridge visualization program [1] has been modified to include the possibility of nonlinear response of the 5/14 North Connector Bridge from significant earthquake loading. This structure has been heavily instrumented as part of the California Strong Motion Instrumentation Program (CSMIP), with 42 sensors placed on and in the vicinity of the bridge. The author was the PI on 2 prior Lifeline Response Projects [1, 2], and is the PI for the project discussed in this paper. In the 1st project, detailed finite element analyses were conducted and compared to measured responses of the 5/14 North Connector, with excellent results. For the second project a bridge visualization computer program was developed that allows the animated measured response of 3 bridges to be viewed in 3-D, with any level of exaggeration to deformations and level of perspective. The three bridges included in the visualization program are the Golden Gate Bridge, Vincent Thomas Bridge and the 5/14 North Connector Bridge. As modifications to the visualization program for the on-going project only concern the 5/14 Connector, the other bridges will not be discussed further herein.

Of importance in the development of the original bridge visualization program is that it realistically displays the measured bridge motions without requiring detailed structural analyses. The reasons for this are that (1) real-time animation is possible while rotating the bridge with the mouse due to increased computing speed, (2) displacements are known at instrument locations for all time intervals by double integration and filtering of measured accelerations, (3) development and verification of detailed structural models takes considerable time and can be

subjective and (4) a predictive analysis model, especially a nonlinear one, is complicated and results in skepticism opinions from decision makers, partly because different models often predict different behaviors. This is best demonstrated by comparing weather patterns predicted by the various computer models and reported on the nightly news. As with weather predictions, nonlinear response of bridge structures subjected to earthquakes is still considered to be a somewhat subjective practice. By avoiding structural modeling it can be argued the that the 3-D animated response represents the actual measured dynamic behavior of the structure, with all instrumented locations moving through the measured displacement time-histories and all other locations displayed by interpolation between measured data.

Modifications to the existing program includes (1) showing color-coded damage levels for the bridge columns that are designed to perform in the nonlinear range when subjected to a design-level earthquake and (2) changing the elastic spline functions to allow for plastic column displacements. Original cubic spline functions that are used to determine the bridge response between measured locations (based on elastic beam theory) are modified to properly display the nonlinear response of the structure that includes plastic and elastic displacement components. Both of these modifications require that the idealized yield displacement in the local transverse and longitudinal directions be known for each column of the 10-span structure. One possibility was to use moment-curvature analyses for each column in the transverse and longitudinal directions and then calculate the idealized yield displacements for the two local column directions. This idealized yield displacement represents displacement ductility 1 and all other displacement levels can be shown color-coded as a multiple of this yield displacement. The idealized yield displacement also provides the dividing line between measured elastic and plastic displacements, allowing realistic nonlinear splines to be displayed in the 3-D animation of the measured bridge response.

Running moment-curvature analyses for each column section requires that all of the column details be known, including the column shape, longitudinal and transverse reinforcement details and the axial load on the column. However, this goes against the original philosophy of the project to have a visualization tool that animates the measured bridge response with no dependency on a detailed structural analysis component. This dilemma is resolved in the following with the development of simple yield displacement expressions that are based only on the column geometry (aspect ratio and column height).

## Idealized Yield Displacement

A series of moment-curvature analyses were conducted using ANDRIANNA [3] in order to compare the yield curvature for various sections. Since yield curvature has the dimensions of radians/inch, it was immediately clear that sections with different size, but with the same longitudinal and transverse steel ratios and the same axial load ratio would have yield curvatures in proportion to their gross section dimensions. In other words, the yield curvature multiplied by the gross section dimension (in the direction of loading) is identical for different size sections that are otherwise the same. It was of interest then to compare sections of the same size with varying levels of axial load and longitudinal steel ratios. The transverse steel ratios are modified accordingly so that all of the members have a displacement ductility capacity of 6, providing a realistic level of transverse confinement to the column.

Moment-curvature analyses were conducted for a 6 ft diameter column with longitudinal steel ratios ranging from 1 to 2% and axial load ratios ranging from 5 to 20%. This is the typical range for bridge columns. From this study it was found that the idealized yield curvature multiplied by the gross column dimension of 72 inches (6 ft) was, on average, equal to 0.0054 (with no result more than 10% outside of this value). As discussed above, the identical value is found from dimensional analysis for, say, a 1-foot diameter column and a 10-ft diameter column, so long as the longitudinal and transverse reinforcement ratios and the axial load ratio are kept the same. It was then required to determine if this ratio also works for different section shapes, and so moment-curvature analyses were also conducted for the bridge column sections of the 5/14 Connector. Separate moment-curvature analyses were conducted in the transverse (strong) and longitudinal (weak) directions for the 10.5'x7' and the 12'x8' columns. Since the axial loads vary along the connector a range of axial loads were included, representing axial load ratios of 5 to 10%.

Idealized yield curvatures are plotted against axial load ratio from moment-curvature analyses of the 6 ft column and the 5/14 Connector columns (10.5'x7' and 12'x8') in Figure 1. Here it is clear that there are significant differences between yield curvatures of the different sections. However, with yield curvature multiplied by the gross section dimension (in the loading direction) the comparisons are much closer, as shown in Figure 2. The normalized line in Figure 2 is placed at 0.0054, and a study of the data shows that all of the results are within 10% of the normalized line. So for standard bridge column ratios it appears that the idealized yield curvature multiplied by the gross section dimension (in the direction of interest) can be taken as the dimensionless constant of 0.0054.

For a cantilever column the idealized yield displacement is found in terms of the yield curvature and column length to be

$$\Delta_y = \frac{\phi_y L^2}{3}$$

However, the yield curvature may be expressed as the dimensionless constant of 0.0054 divided by the gross section dimension *D*, or

$$\phi_y = \frac{0.0054}{D}$$

permitting the cantilever yield displacement (representing transverse column response of the 5/14 Connector) to be written

$$\Delta_y = 0.0018\frac{L^2}{D}$$

The aspect ratio is given as the column length divided by the section dimension in the direction of interest

$$\eta = \frac{L}{D}$$

allowing the yield displacement in the transverse direction to be written in terms of the column aspect ratio and column length.

$$\Delta_y = 0.0018\eta L$$

In the longitudinal direction the column responds in double bending due to the continuity of the superstructure. However, the point-of-contraflexure is shifted somewhat and, based on typical ratios of superstructure-to-column stiffness, the point of inflection is found to be at 0.55 the column height. From the moment-area displacement method (recognizing that the M/EI diagram is the curvature) the idealized yield displacement is found as

$$\Delta_y = \frac{\phi_y L^2}{5}$$

and, as with the cantilever column, the yield curvature is given as

$$\phi_y = \frac{0.0054}{D}$$

The yield displacement for the longitudinal direction is

$$\Delta_y = 0.00108\frac{L^2}{D}$$

Or, in terms of the aspect ratio and column length

$$\Delta_y = 0.00108\eta L$$

With the 2 expressions given above for idealized yield displacements in the local transverse and longitudinal column directions, all ductility 1 displacement values can be found from the column aspect ratio $\eta$ and the length $L$. The aspect ratio is the column length divided by the maximum column cross-section dimension in the direction of loading.

The cantilever yield displacement expression is further validated by comparisons against measured yield displacements reported from 7 reinforced concrete bridge column structural tests with varying aspect ratios, axial load ratios and longitudinal steel ratios. Axial load ratio ranged from 7 to 18%, longitudinal steel ratio ranged from 0.75 to 3% and the aspect ratio ranged from 4 to 10. For each of the 7 test units the simple expression given above is compared to reported, idealized yield displacements found directly from the measured experimental results (see Figure 3). These tests were conducted at UCSD and UCB under three different projects [4, 5 and 6].

All of the column tests reported in [6] and the reference column tests reported in [4] and [5] are included in the comparison. Figure 3 show reasonably close results between the simple expression and measured yield displacements. It is interesting to plot these results against column height for all 7 structural tests (Figure 4). Here points are plotted from the 7 tests as well as the corresponding points from the simple expression. A best-fit exponential curve is drawn through the two sets of points, demonstrating a very similar trend between the simple expression and the measured results. Indeed, more variation is seen between competing methods for calculating theoretical yield displacement than between the simple expression and the measured results.

The two validated yield displacement expressions are used for this project in determining displacement ductility one in the local transverse and longitudinal directions. The expressions are included directly in the visualization program, requiring only the column height and overall column cross-section dimensions (width and depth) to determine the ductility one displacement for both local directions. With this it is possible for the program to determine and display in changing colors, and in real time, the displacement ductility demand for each column in both local directions. This is an excellent indicator of the damage level sustained. Ductility demand is the relative displacement between the top and bottom of the column (measured) divided by the idealized yield displacement found from the new and simple expressions. Ductility one assessment also allows the program to more accurately display the column behavior under dynamic loading, as the measured column displacements can be separated into elastic and plastic components. Elastic displacements follow cubic spline shape functions while plastic displacements follow straight shape functions between plastic hinges. Combining these gives realistic deformation patterns for nonlinear response in single and double bending.

## Visualization Program

The initial panel for the modified bridge visualization program is shown in Figure 5. Here all 3 bridges that were included in the original program are given and can be used. However, nonlinear behavior has been included only for the 5/14 North Connector. This is a 10-span, single-column-bent, cast-in-place, prestressed concrete box-girder bridge. Several pictures of the structure are given in the 5/14 Connector tab (Figure 6). From this panel the Model tab is clicked and from the Views box, near the bottom of the screen, the Isometric tab is clicked, showing the model from an angle with a level of perspective of 2000 (Figure 7). This perspective number represents a viewpoint that is positioned 2000 ft from the center of the bridge. Other standard views can be selected or the bridge can be rotated about any axis with the mouse.

By clicking on the Select EQ tab, a menu appears and the EQDatabase is clicked followed by selecting the 514 directory (Figure 8). In this directory there are 3 data files that the visualization program can read, developed from past, recorded earthquakes measured at the bridge site. Of these three the most interesting is the Hector Mine Earthquake record (HMine.txt), as it resulted in 50 times more structure displacement than the other 2 earthquakes listed. Even so, the maximum relative column displacements were still very small compared to yield displacement of the columns indicating that the bridge has not yet performed in the

nonlinear range as expected from a major earthquake. Elevation and plan views of the model are given in Figures 9 and 10, selected from the Views box.

Longitudinal and transverse column yield displacements are automatically computed by the program and can be viewed by clicking the Yield Displacement button (Figure 11). Displacement ductility demand is color-coded from Magenta at ductility 1 to deep red at ductility 6 (Figure 12). In order to test the behavior of the modified model the displacement demands from an earthquake must be larger than the yield displacements. With this in mind, is was decided to use the existing measured data from the Hector Mine Earthquake and scale up the results to represent large measured motions. This will test the color changing capabilities in the animation that graphically show damage levels developing in the columns and provide visual validation of the modified splinning techniques where elastic and plastic components are initially separated and then added back together again after using different spline techniques. Prior to exceeding yield displacement the columns behave in single bending in the transverse direction and double bending with a shifted point-of-contraflexure at 0.55 up the height of the column in the longitudinal direction.

Prior to column plastic hinging, at the base of the column there should be no absolute rotations and there should be no relative rotations between the top of the column and the superstructure. However, as ductility demand increases the plastic hinge formation will be visible by the more straightened appearance of the column (plastic displacement component of total measured relative displacement is larger than the elastic displacement) and the concentrated relative rotation between the superstructure and top-of-column, as well as the concentrated rotation at the column base. The superstructure rotation at the top of the column will be less than the total top-of-column rotation, but it will be the rotation associated with column yield displacement. In Figure 13 the column at Bent 10 is at a displacement ductility of 3 in the longitudinal direction. In order to really see the behavior, longitudinal deformations have been magnified by a factor of 25. It is clear that the column shape is a combination of elastic and plastic displacements, with concentrated plastic rotation at the base of the column and a definite relative rotation between the top of the column and the superstructure. Note that the superstructure is rotating at the top of column, but not as much as the column is. To view the displacement ductility colors legend the Ductility check box under Display is chosen. Within the ductility color legend, Transverse or Longitudinal behavior can be chosen. If both are selected then it will show the maximum ductility demand from either local direction.

Prior to forming plastic hinges, the columns respond in single bending in the transverse direction (Figure 14). Longitudinal and transverse ground motions are shown near the top of the screen, indicating small input in Figure 14 at 16 seconds and much larger ground motions by the time Figure 13 was captured at about 45 seconds. Transverse plastic hinging is seen in Figures 15 and 16 with maximum displacement ductility demands of 3 and 4, respectively. A few seconds later the end columns reach displacement ductility 6, with an exaggerated displaced shape that resembles a straight line (Figure 17). From initial loading the columns respond in double bending in the longitudinal direction, with no rotation at the base of the columns and no relative rotation at the column/superstructure joint (Figure 18). In Figure 19, plastic and elastic longitudinal column behaviors are seen in the same picture, with the column at Bent 9 exceeding ductility 3 and the adjacent Bent 8 column responding with less demand.

## Conclusions

The existing bridge visualization program has been modified to include nonlinear behavior of the bridge columns for the 5/14 North Connector subjected to future large ground shaking from a design-level earthquake. The program allows measured responses of the bridge to be viewed in 3-D animation, with any level of deformation exaggeration, level of perspective and time-scale. Different deformation scales can be applied to the longitudinal and transverse directions. While animated the bridge model can be rotated about different axes, translated in any direction and zoomed in or out with the computer mouse, and different components of the model can be turned on and off. The animation can be slowed down or sped up, and the model can be paused at any time. While paused, the bridge can be rotated and the deformation scales can be changed, as can the distortion associated with level of perspective. In fact, all of the functions that apply to the bridge model while being animated also apply to it when frozen in time. This is interesting because very different appearances and viewpoints are possible while the model data remains the same.

Modifications to the bridge visualization program that have been implemented as part of this on-going project include color-coded damage indicators that display different colors for each level of displacement ductility that the columns are subjected to, based on measured relative displacements between the top and bottom of the columns in the two principal directions. Displacement ductility demand is defined as the displacement demand of the column divided by the idealized yield displacement. As the column acts in single bending in the transverse direction and double bending in the longitudinal direction, the yield displacements are different in the local longitudinal and transverse directions.

To avoid detailed calculations in keeping with the visualization tool philosophy, simple expressions were developed to determine the yield displacement of a column based only on its aspect ratio in the direction of loading and on the column height. Different expressions were developed for the longitudinal and transverse column directions. This approach was validated both analytically and experimentally, by comparing the simple expression and measured yield displacements from 7 cantilever column experiments. The only additional input required for the modified program is the overall section dimensions (width and depth, independent of section geometry), as the column lengths were already included in the original version of the program.

With realistic yield displacements determined, column ductility levels are displayed with changing colors of the columns as the bridge moves through measured motions collected by the Strong Motion Instrumentation Program. An important aspect of including column plastic hinging in the bridge visualization program is to modify the cubic spline functions that work well for animating linear-elastic column response, but do not capture the dynamic behavior of bridge columns subjected to a significant earthquake. For bridges the columns are designed to respond to a major earthquake in the nonlinear range and are detailed to allow significant ductility demands (the cost is prohibitive to design bridge columns to remain elastic in high seismic areas). Significant displacement ductility capacity of well-confined reinforced concrete bridge columns has been verified by large-scale and full-scale cyclic experiments at many institutions. In the modified visualization program measured deformations are separated into their elastic and

plastic components and the elastic part is splined with a cubic function, while the plastic term is represented by a straight line between plastic hinges.

The simple yield displacement expression allows the modified program to determine transverse and longitudinal yield displacements for each column, which in turn permits realistic splines to be displayed for the columns and bridge superstructure. It also allows damage levels to be quickly assessed based on the displacement ductility demand. Local transverse and longitudinal displacement ductility demands can be viewed separately or together in the animation program.

Still to be added to the bridge visualization program, as the project continues, is the display of complete section geometries including the multi-cell box-girder superstructure with overhangs and the column sections to add more reality to the 3-D animation of the bridge. The ground line will also be added. It is not yet clear, however, if animation speed can continue to be real-time with the complete sections and ground surface displayed, and this is anticipated to be a challenge due to the increased amount of graphics and computations. Based on the plane sections hypothesis of beam bending, all section locations can be determined based on the location of the member centroid, the section curvature (from the splines) and distance to the section edge from the section centroid. The existing visualization model represents superstructure and column members with lines that follow the section centroids.

Nonlinear time-history analyses using SAP2000 [7] will also be conducted of the 5/14 Connector subjected to measured ground motions from other sites or scaled up measured motions from the bridge site. Displacement time-history results from the time-history analysis at instrumented locations will be saved to a data file and will represent virtual measured bridge motions. The bridge visualization program will then be loaded with these “measured” motions and side-by-side animated views from both programs will be compared from various angles and perspectives. Elastic and nonlinear comparisons will be conducted. Note that this step is required since the 5/14 Connector has not yet been subjected to an earthquake large enough to cause plastic hinges to develop at the column ends.

Supported by the California Department of Conservation, California Geological Survey, Strong Motion Instrumentation Program, Contract 1004-795.

## References

1. Dowell, R.K., *Visualization of Measured Seismic Bridge Motions*, Report No. DH-04-08, Dowell-Holombo Engineering, Inc., San Diego, California, 2004.

2. Dowell, R.K., *Time-History Analysis versus Measured Seismic Responses of the 5/14 Connector Bridge*, Report No. DH-04-02, Dowell-Holombo Engineering, Inc., San Diego, California, 2004.

3. Dowell, R.K., ANDRIANNA User's Guide, Dowell-Holombo Engineering, Inc., 2002.

4. Hose, Y.D., Seible, F., Priestley, M.J.N., *Strategic Relocation of Plastic Hinges in Bridge Columns*, Report No. SSRP-97/05, University of California, San Diego, 1997.

5. Priestley, M.J.N., Seible, F., Seismic Assessment and Retrofit of Bridges, Reprt No. SSRP-91/03, University of California, San Diego, 1991.

6. Lehman, D.E., Moehle, J.P., *Seismic performance of Well-Confined Concrete Bridge Columns*, Report No. 1998/-01, Pacific Earthquake Engineering Research Center, Berkeley, 1998.

7. SAP2000, Version 9, User's Manuals, Computers and Structures, Inc., Berkeley, California, 2004.

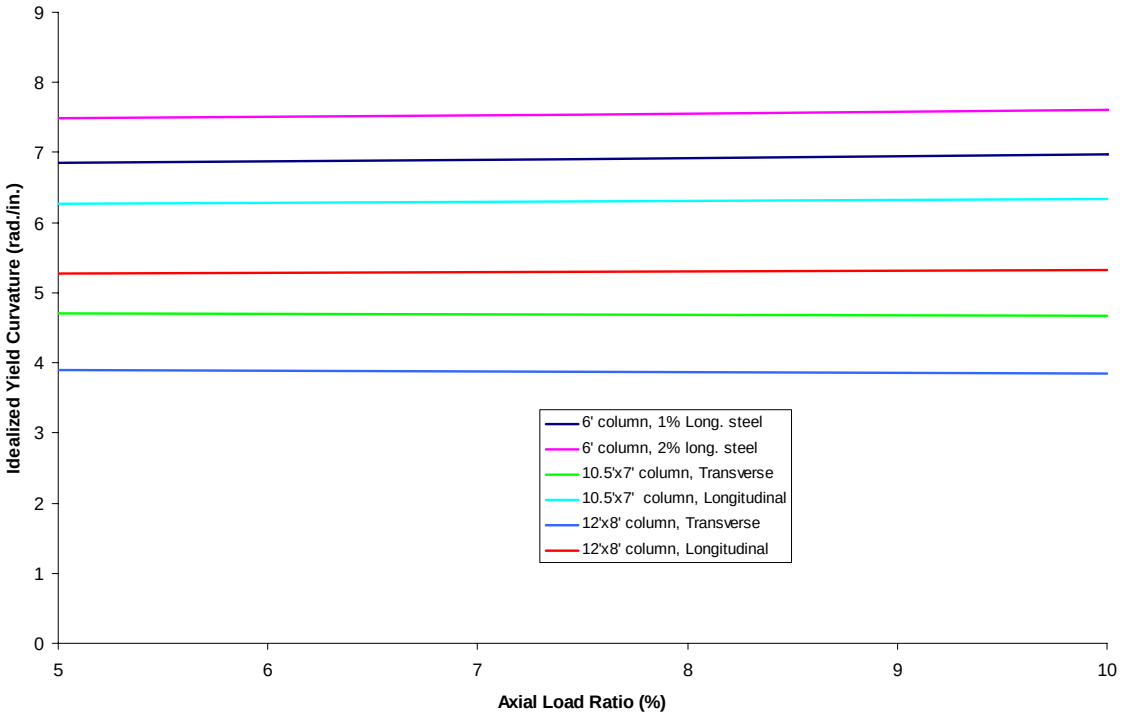


Figure 1. Idealized yield curvature from moment-curvature analyses

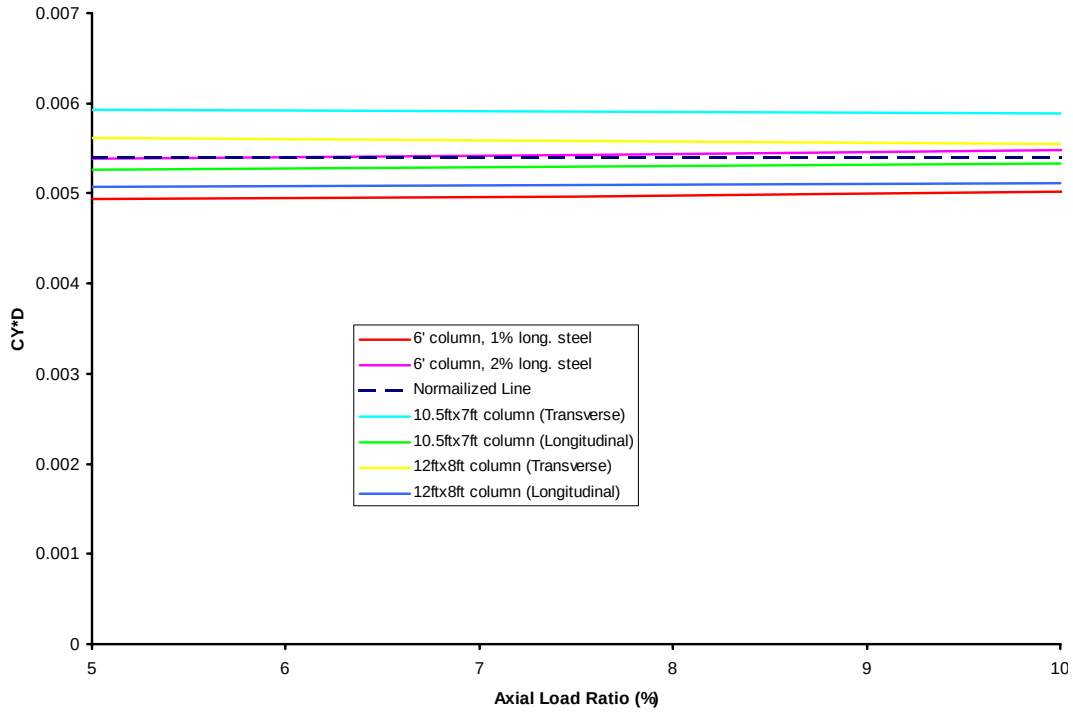


Figure 2. Idealized yield curvature multiplied by gross section dimension (in loaded direction)

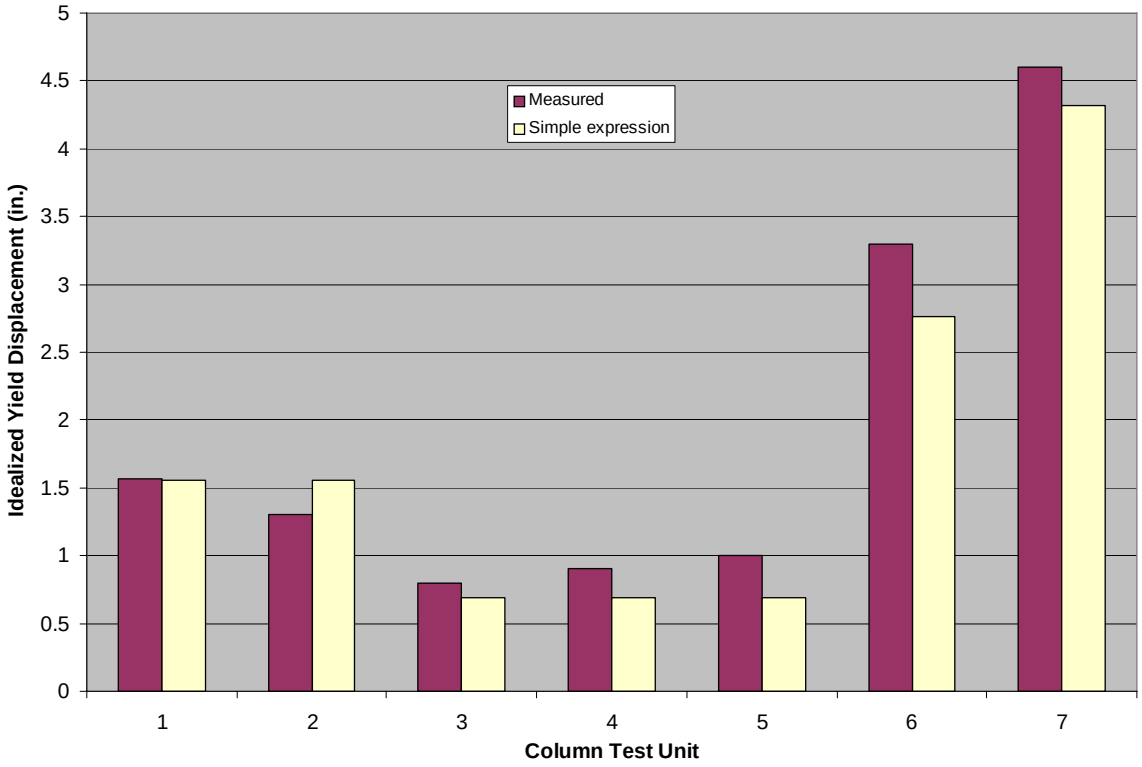


Figure 3. Measured versus simple expression yield displacements

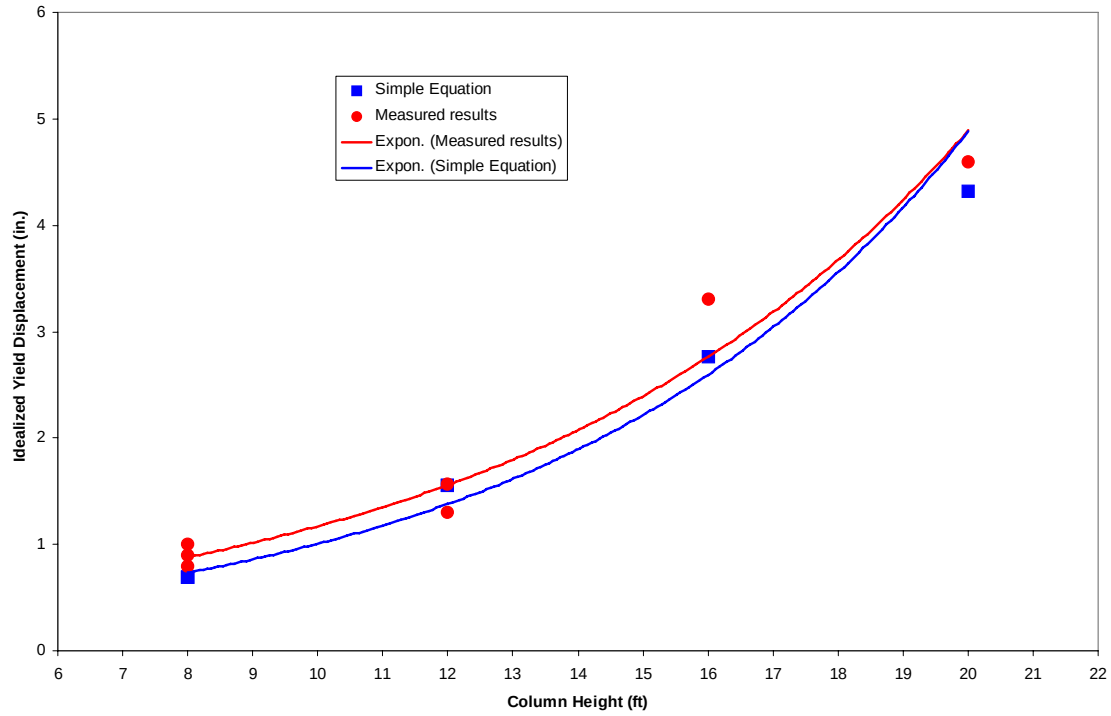


Figure 4. Measured and simple expression yield displacements versus column height

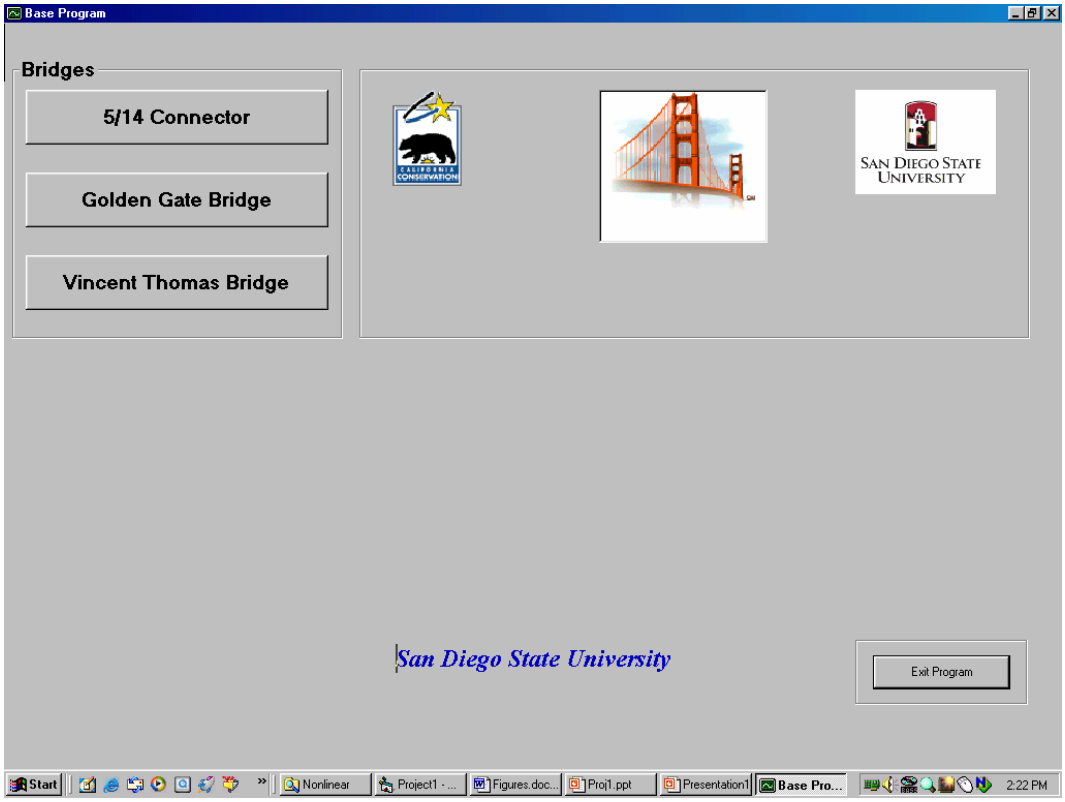


Figure 5. Graphical user interface, initial panel


Figure 6. 5/14 Connector tab

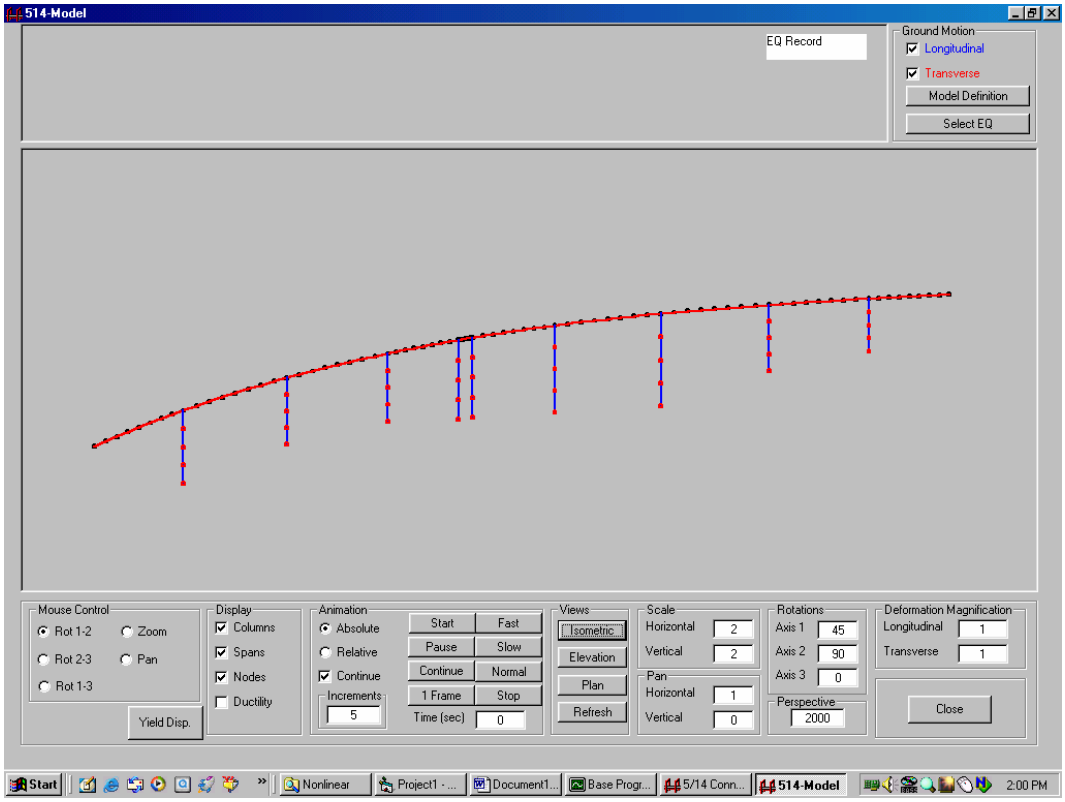


Figure 7. Model tab, isometric view of 5/14 Connector

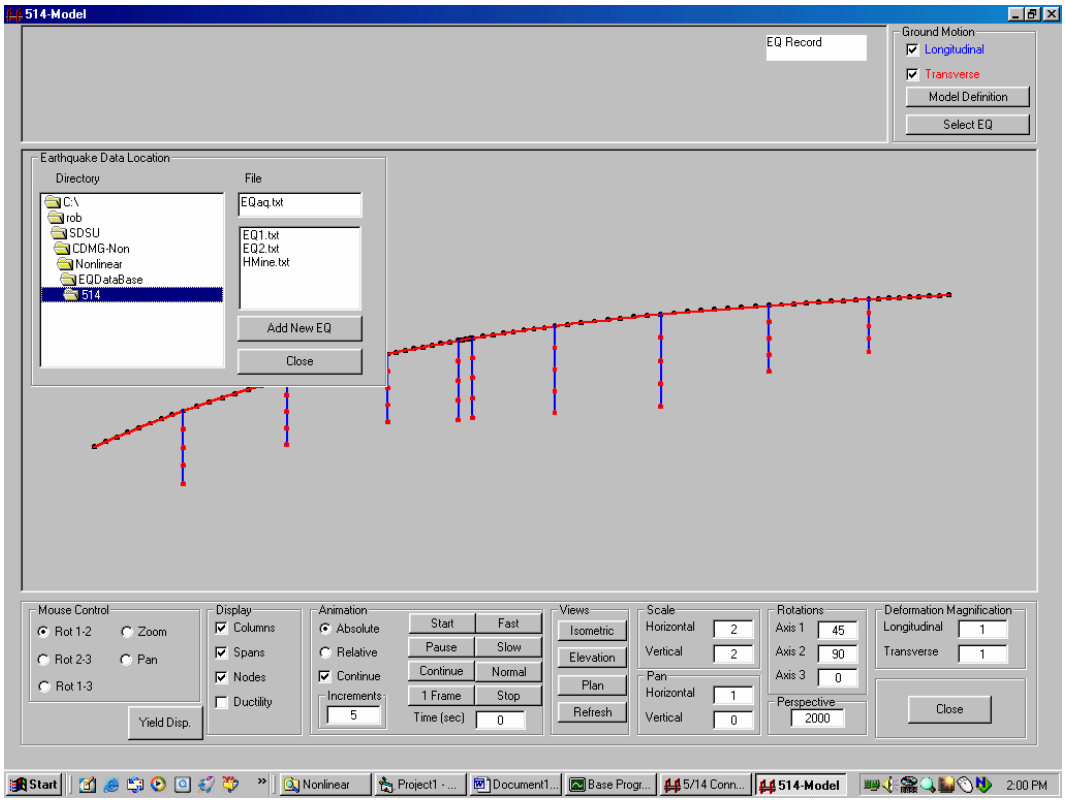


Figure 8. Selection of earthquake file from database directory

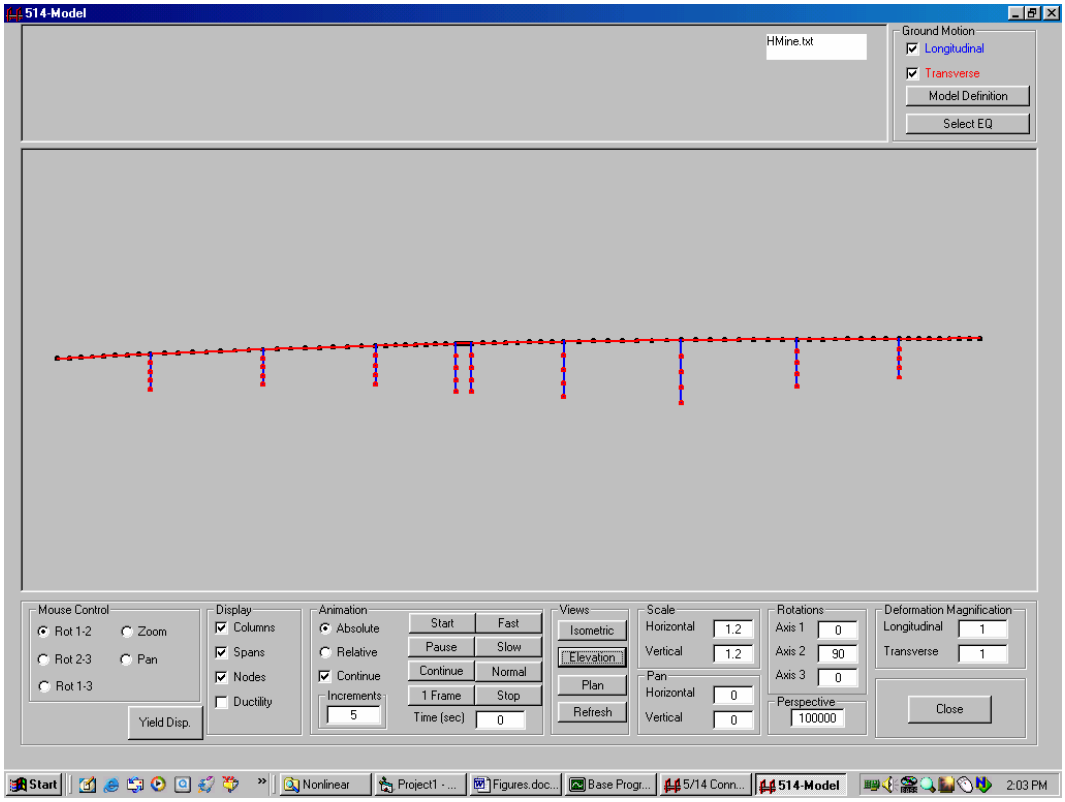


Figure 9. Elevation view of model

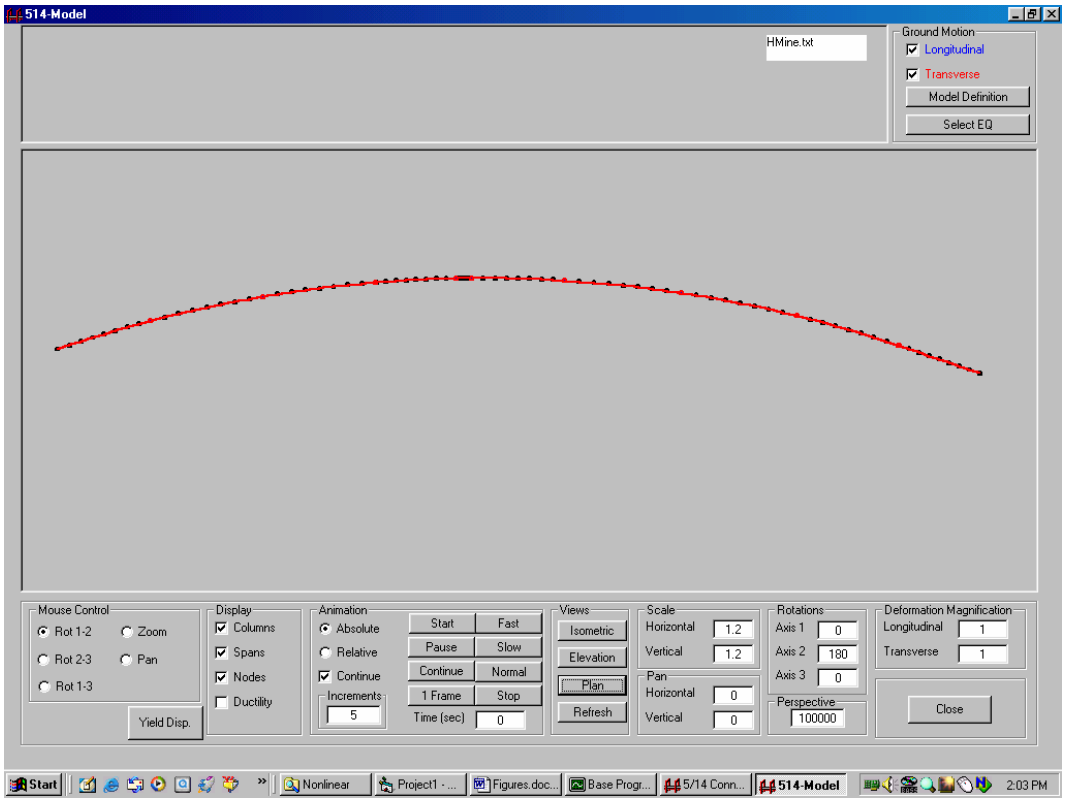


Figure 10. Plan view of model

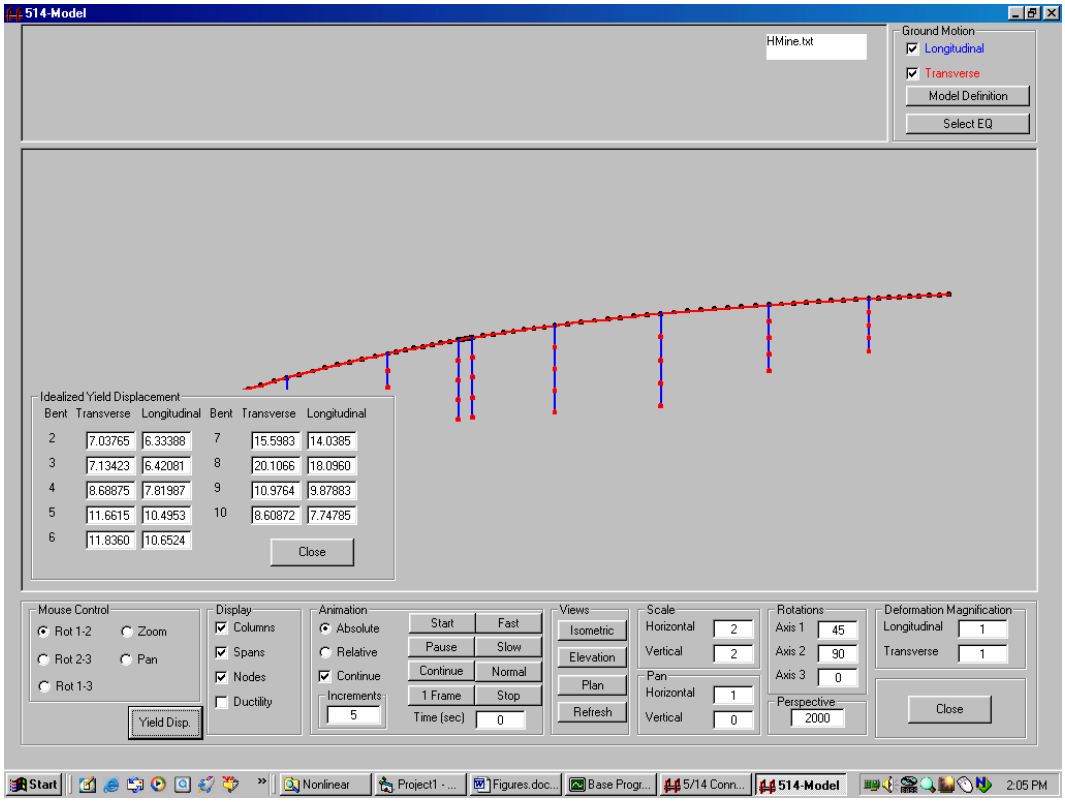


Figure 11. Longitudinal and transverse yield displacements for each column

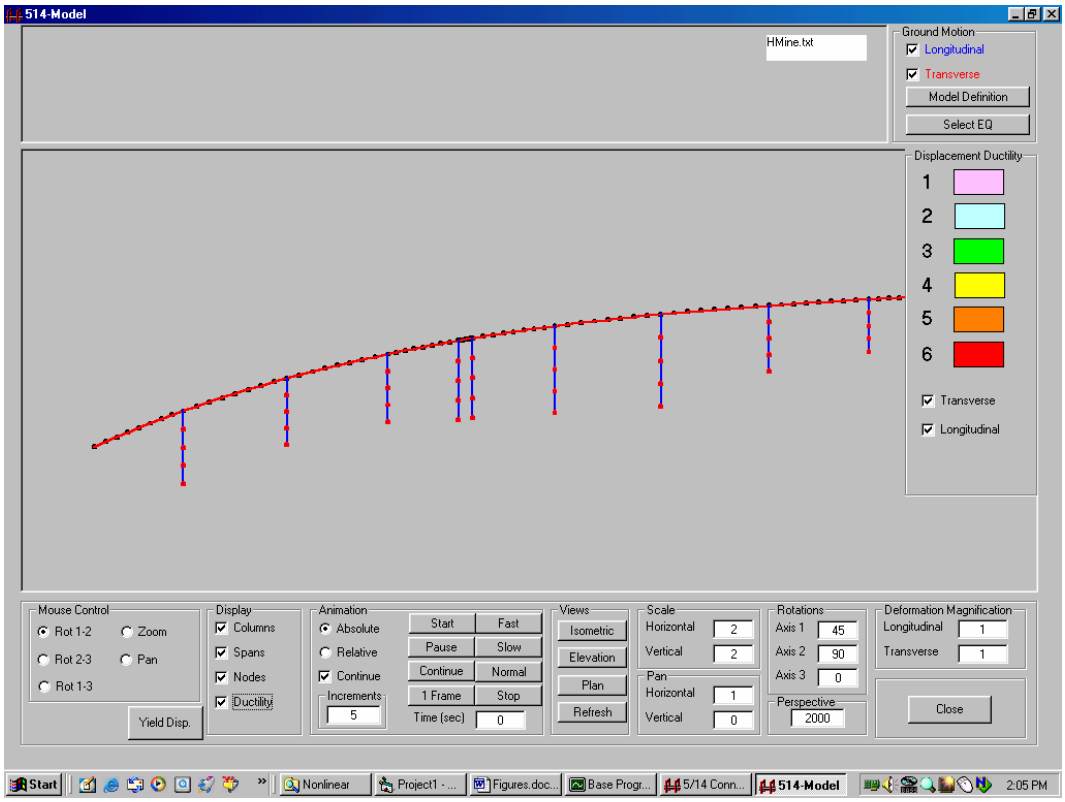


Figure 12. Displacement ductility levels

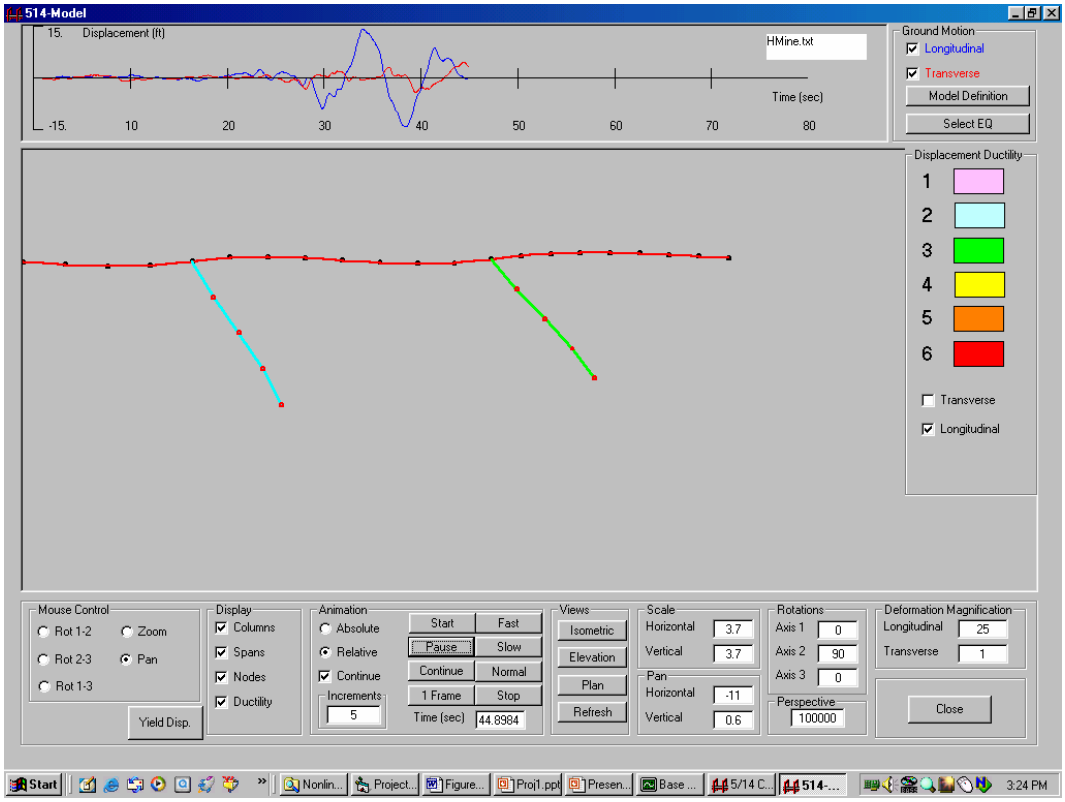


Figure 13. Column at Bent 10 at displacement ductility 3

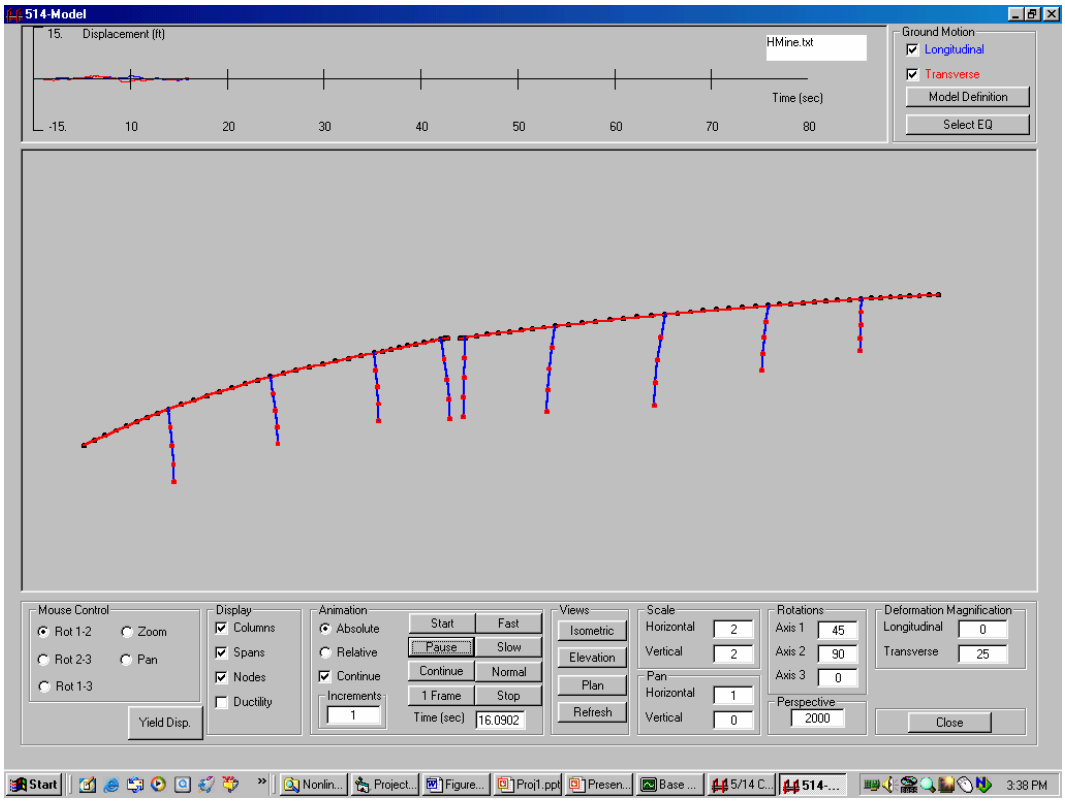


Figure 14. Transverse response prior to plastic column hinging.

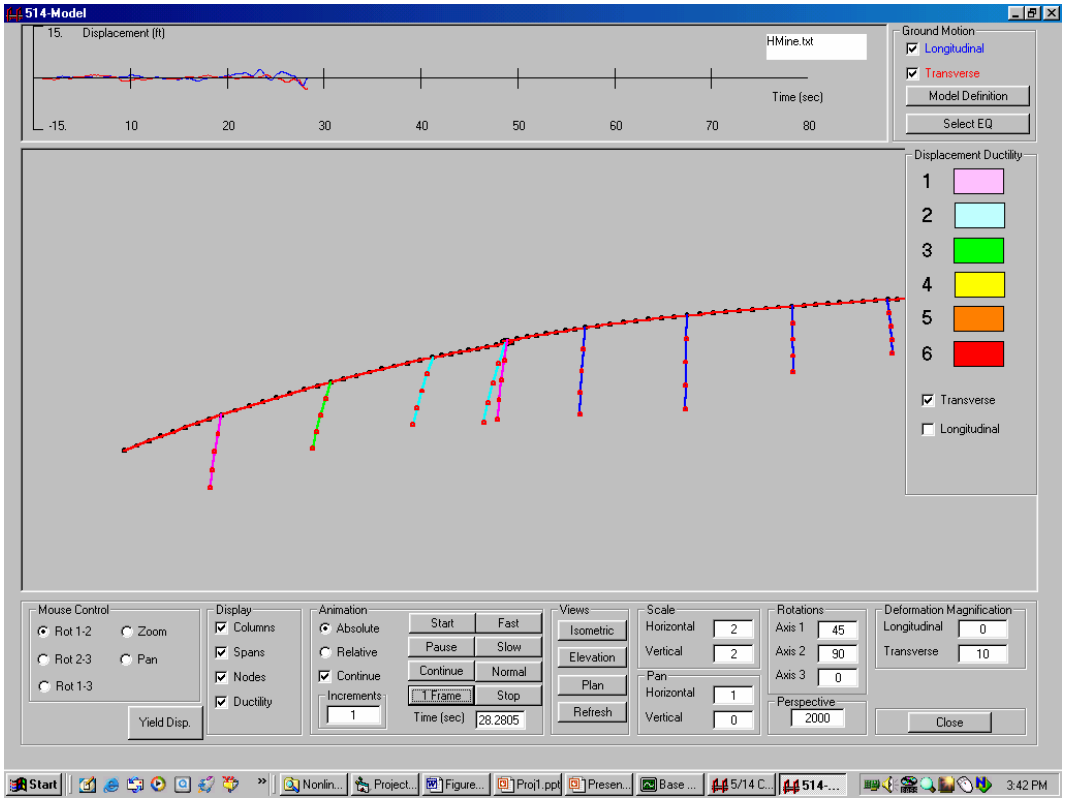


Figure 15. Transverse response with the Bent 2 column exceeding ductility 3

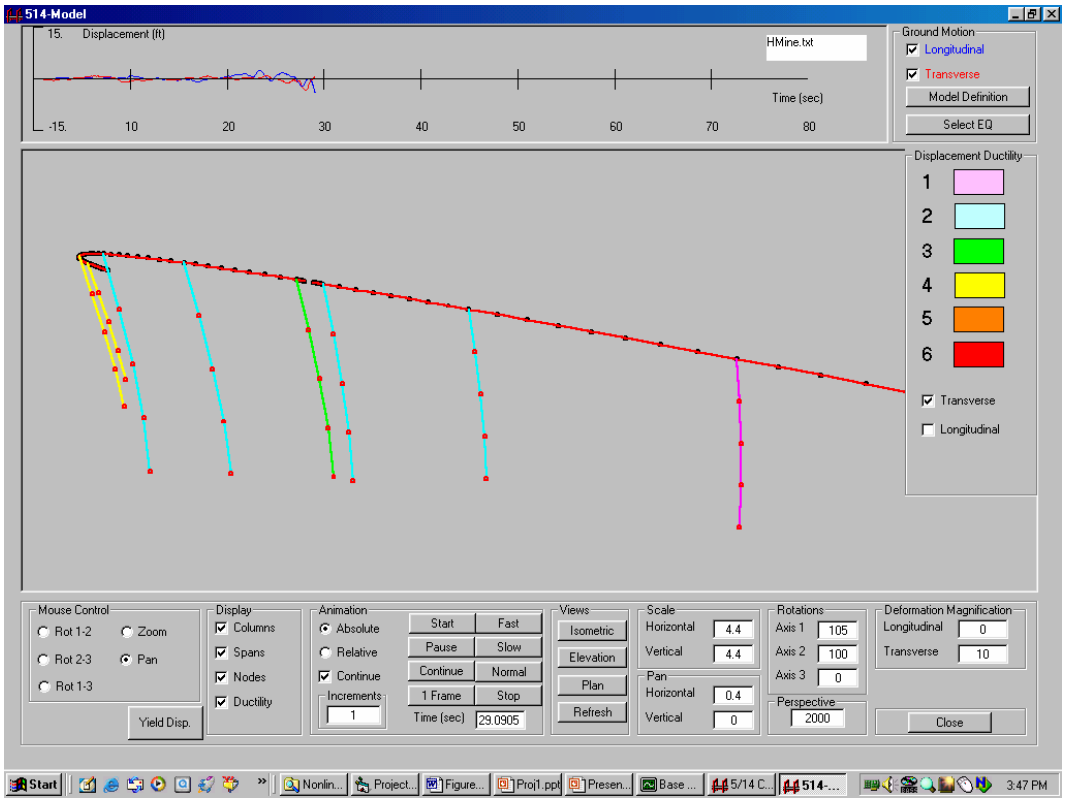


Figure 16. Transverse response with columns at Bents 9 and 10 beyond ductility 4

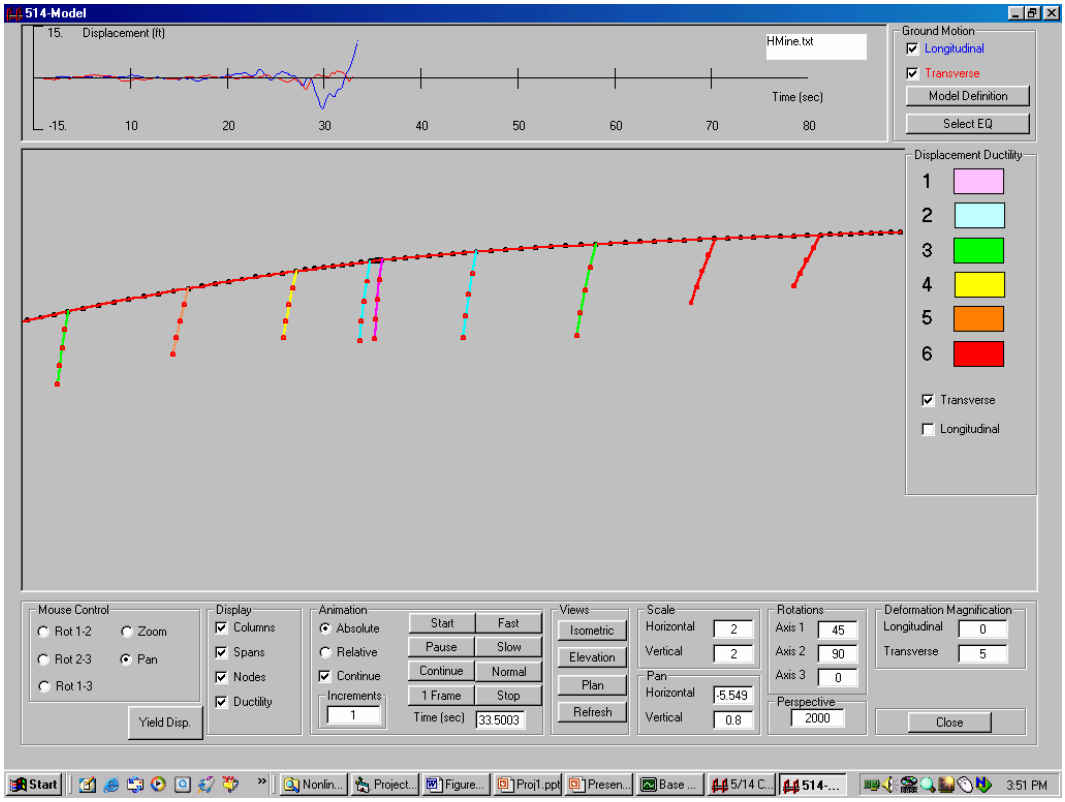


Figure 17. Transverse response with Bent 9 and Bent 10 columns exceeding ductility 6

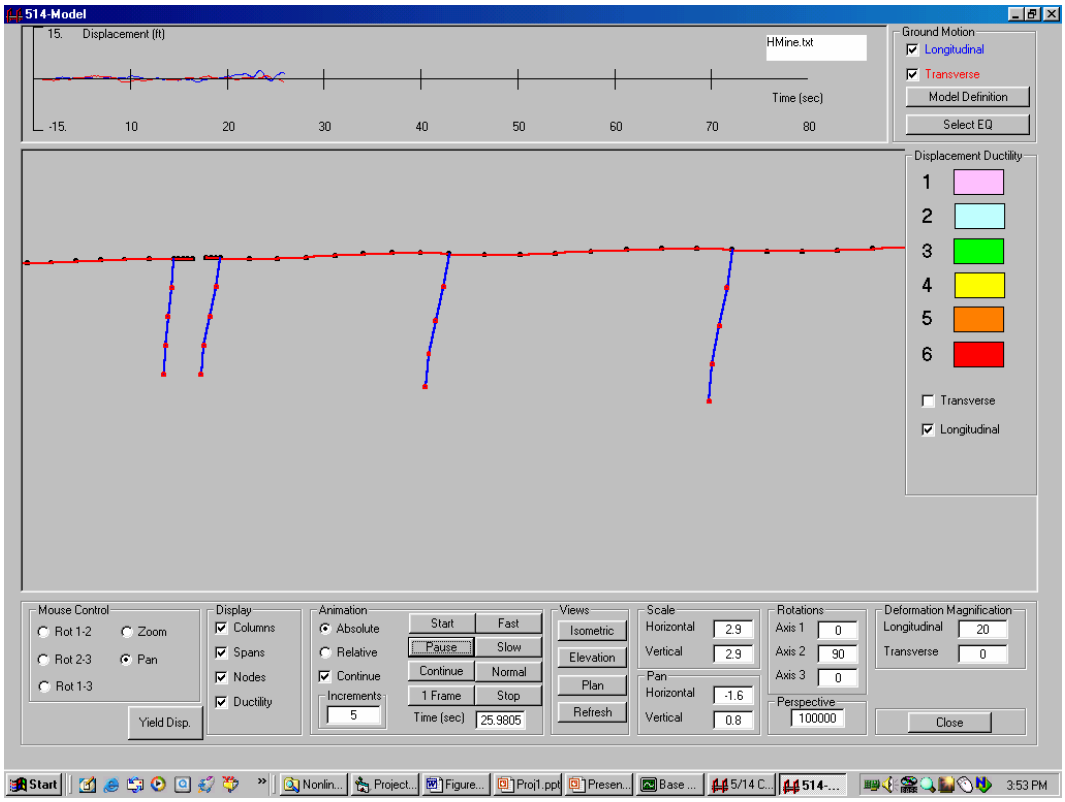


Figure 18. Longitudinal response prior to plastic hinging

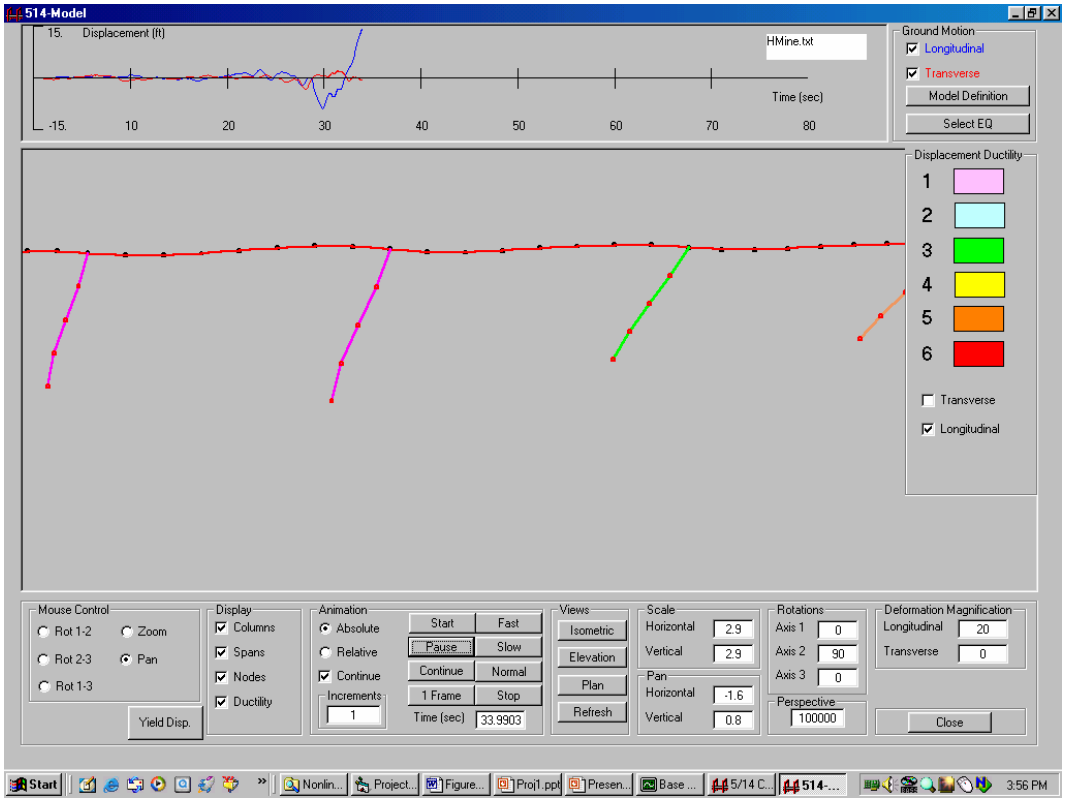


Figure 19. Longitudinal plastic response of Bent 9 column at ductility 3

# AUTOMATED POST-EARTHQUAKE DAMAGE ASSESSMENT AND SAFETY EVALUATION OF INSTRUMENTED BUILDINGS

Farzad Naeim, Scott Hagie and Arzhang Alimoradi

John A. Martin and Associates, Inc.

Eduardo Miranda

Stanford University

## Abstract

A set of methodologies for automated post earthquake damage assessment of instrumented buildings are presented. These methods can be used immediately after an earthquake to assess the probability of various damage states in the N-S and E-W directions and throughout the height of each building. The methods have been applied to more than 40 CSMIP instrumented buildings which have recordings from more than one earthquake. The results indicate that the proposed methods, when used in combination, can provide very useful information regarding the status of a building immediately after an earthquake by simple and rapid analysis of sensor data and prior to any building inspections.

## Introduction

This paper provides an overview of an exhaustive investigation to determine the feasibility of an automated approach to post-earthquake damage assessment of instrumented buildings and establishment of a coherent set of techniques and methodologies to achieve the objective of automated post-earthquake damage assessment.

The objective of this project was to use and study strong-motion data from instrumented buildings with several earthquake records to determine the threshold of measures of motion that would provide guidance to the building officials, in a manner consistent with ATC-20, for determining whether to inspect the building or evacuate it based on the records taken from the building. The proposed measures are such that they can be computed directly from recorded data of instrumented buildings.

Due to publication space constraints this paper provides only a preview of the methodologies developed and a small number of representative examples. A full report which is currently in preparation (Naeim et. al, 2005) will contain detailed information regarding various methodologies implemented and the results of application to numerous instrumented buildings. In addition, papers are being prepared for submission to scientific journals that document certain

major developments achieved during this project (Alimoradi, et. al 2005a; Alimoradi et. al, 2005b).

Automated damage assessment (ADA) provides an incentive for building owners to instrument their buildings and has the potential of significantly adding to the inventory of instrumented buildings so critically needed for development and evaluation of existing and future design provisions. Elimination or reduction of possible false alarms produced by ADA procedures is a major concern. Therefore, we assess damage using several independent techniques and provide the degree of confidence in terms of probability of occurrence with each of our damage assessments.

Robust ADA methodologies should be able to provide increasingly more accurate estimates of post-earthquake damage when more information is available regarding the building and its contents. With our approach, preliminary damage estimates are provided based on the sensor data and a general understanding of the building and its contents. More accurate damage estimates may be obtained if more detailed information regarding the structural system and contents are available such as detailed fragility curves for various components.

The more specific information ADA provides, the more useful it is. We provide damage estimates per floor in each direction of the building. Damage estimates may be based on the maximum response values per floor or response values at the geometric center of each floor's diaphragm.

In more ways than one this project is a natural continuation of the last year's effort which resulted in development and dissemination of the CSMIP-3DV software system (Naeim, et. al, 1994). We utilized and expanded on the information that we generated regarding 80 CSMIP instrumented buildings contained in the CSMIP-3DV database in order to evaluate, rank, and combine various potential methods to achieve reliable automated post-earthquake damage detection. These enhancements include:

- Calculation of instantaneous and envelope values of story forces and story shears, as well as hysteretic diagrams for these parameters.
- Calculation of instantaneous and envelope values of floor accelerations, velocities and floor spectral attributes.
- Application of numerous fragility curves (Aslani and Miranda 2003; FEMA 2004; Porter and Kiremidjian 2001) for probabilistic assessment of damage to structural and nonstructural systems and components.
- Investigation of possible use of FEMA-356 (ASCE 2000) tables and/or linear/nonlinear response analyses for damage assessment.
- Investigation of the use of Wavelet Analysis techniques for damage assessment
- Development of a new rapid system identification technique based on the use of Genetic Algorithms (Alimoradi, et. al 2005a) and approximate mode shapes (Miranda and

Taghavi 2005; Alimoradi, et. al 2005b) for identifying building periods, mode shapes, and changes in dynamic characteristics of buildings during their response to earthquake ground motions.

- Investigation of the use of the Fuzzy Logic Theory (Revadigar and Mau 1999) for combining information obtained from various methods and techniques.

## Classes of Potential Damage Indicator Parameters

Several categories of techniques for automated damage assessment based on building records were evaluated:

1. "Simple" or "Design Oriented" Measures. These include demand/capacity ratios based on the following measures.

    a. Comparison of base shear inferred from the records with the capacity level values suggested by the applicable code or used in design.

    b. Comparison of maximum inter-story drifts inferred from records with the capacity level values suggested by the applicable code or used in design.

    c. Comparison of observed peak ground acceleration obtained from the records with the capacity level values suggested by the applicable code or used in design.

    d. Comparison of relevant response spectral entities for a number of modes, combined using an appropriate spectral combination technique, with the capacity level values suggested by the applicable code or used in design.

2. Probability-based Measures. These include the fragility functions developed by PEER/NSF, utilized by HAZUS-MH and proposed by Porter and Kiremidjian as well as an attempt to cast FEMA-356 limit-state tables in a pseudo fragility function form for possible damage assessment. These are probabilistic damage measures for various floors and contents which are developed utilizing one or more of the following indicators:

    a. Peak inter-story drift ratios

    b. Peak floor accelerations

    c. Peak floor velocities

    d. Floor response spectra

    e. Story shears inferred from recorded motions

3. Wavelet Characteristic Measures. These are signal processing measures based on wavelet analyses in which the high-frequency content of the signal is separated from its low frequency content in order to provide information on the timing and extent of changes in the frequency and amplitude characteristics of the sensor data.

4. Damage Measures Based on Structural Identification. These are damage measures

inferred from changes in the dynamic characteristics of the building such as elongation of natural periods or a change in the dominant mode of behavior of the building during an earthquake(i.e., a change from shear dominated deformation shape to a flexural dominated shape or vice versa).

Consistent with ATC-20 (Applied Technology Council, 1989), the damage state suggested by each damage indicator are classified in one of the following four categories:

1. No Damage
2. Slight Damage
3. Moderate Damage
4. Severe Damage

## Use of Fragility Curves for Damage Assessment

As will be shown later in this paper, the various fragility curves proved to be the most useful tools for post-earthquake damage assessment. Once engineering demand parameters have been computed based on interpreted data from the sensors, damage in specific stories can be estimated through the use of fragility functions. A fragility function relates structural response with various levels of damage. Unlike deterministic values recommended in FEMA-356 (ASCE, 2000), fragility functions take into account the uncertainty on the structural motions that trigger different levels of damage. In particular, a fragility function supplies the probability that the structure will reach or exceed a particular damage level.

Available experimental data on various types of structural components permit the development of fragility functions. Recent research at PEER (Aslani and Miranda, 2003) indicates that fragility functions for many structural components can be assumed to follow a lognormal distribution. Fragility curves implemented in HAZUS also utilize a lognormal shape. Examples of probabilities of experiencing light ($dm_1$) and severe ($dm_2$) cracking in reinforced concrete slab-column connections as a function of interstory drift ratio are shown in Figure 1.

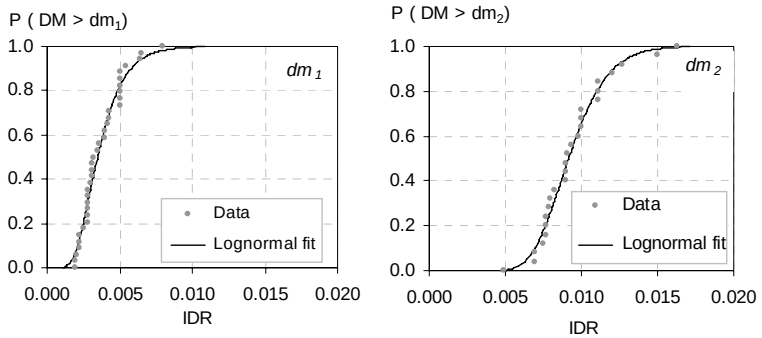


Figure 1. Example of fragility functions to estimate damage in reinforced concrete buildings with slab-column connections as a function of interstory drift (After Aslani and Miranda, 2003).

As shown in this figure severe cracking in slab-columns connections has been observed in specimens subjected to interstory drift ratios as low as 0.5% while in others as large as 1.6%.

Rather than categorically stating that severe cracking occurs at a particular level of interstory drift, fragility functions describe how the probability of reaching or exceeding this level of damage increases as the interstory drift ratio imposed in the building increases. As shown in the figures the lognormal distribution captures quite well the observations from experimental results.

Fragility functions assumed to follow a lognormal probability distribution are defined by only two parameters for each damage state. One parameter describes the engineering demand parameter at which a 50% probability of reaching or exceeding a damage state occurs and the other parameter describes the dispersion in the data. An example of fragility functions for three damage states is presented in Figure 2.

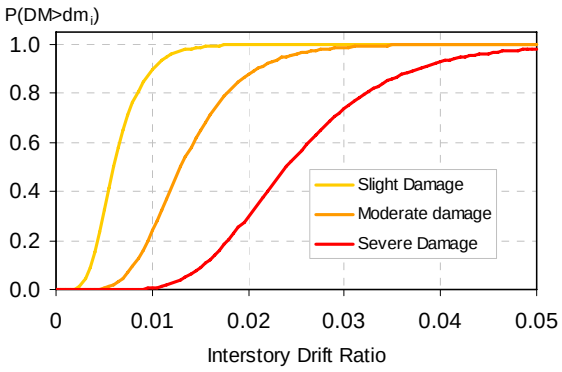


Figure 2. Example of drift-based fragility functions for three damage states.

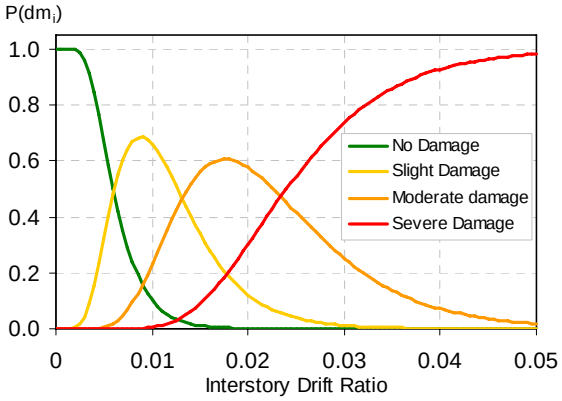


Figure 3. Probabilities of being in various damage states as a function of the level of interstory drift demand.

Once the fragility functions have been defined, the probability of being in one of the damage states is easily computed as the difference between two consecutive damage states. An example of damage being within one of the various damage states is shown in Figure 3.

In can be seen that, for this example, stories with interstory drift demands of 1% would have a very small probability (about 10%) of not having damage, a high probability of having slight damage (about 65%), a small probability of experiencing moderate damage (about 20%) and essentially no chance of experiencing severe damage. However, stories experiencing an interstory drift demand of 2.5% would certainly experience some degree of damage: about 5% probability that the damage is slight, about 40% that is moderate and about 55% of experiencing severe damage.

The fragility-based damage assessment algorithms provide the decision makers with a number of options for estimating structural and nonstructural damage in a CSMIP-instrumented building:

1) Apply the HAZUS-MH fragility functions for various FEMA categories of buildings and regions
2) Apply the PEER/NSF fragility functions or fragility functions provided by other researchers

3) Use the deterministic values provided by FEMA-356; or
4) Use their own fragility functions obtained from detailed structural analyses of the building performed prior to the earthquake(s).

## Examples

An overview of the utility and limitations of various ADA techniques evaluated and implemented during this study are provided by examination of two instrumented buildings. Details of application to other buildings will be included in our final report to CSMIP (Naeim, et al, 2005). The two selected building examples are:

1. The Imperial Valley County Services Building response to the 1979 Imperial Valley earthquake, and
2. The Van Nuys 7 Story Hotel response to the 1992 Landers and Big Bear, and the 1994 Northridge earthquakes.

### Example 1. Imperial Valley County Services Building (CSMIP ID = 01260)

This six story building has been the subject of numerous studies (Figure 4a). A reinforced concrete building with discontinuous shear walls, it suffered severe damage in the form of collapse of the first floor concrete columns at the ground floor during the 1979 Imperial Valley earthquake (Figure 4b). The building was subsequently demolished. The irregular structural system, interruption of exterior walls at the second floor, and sudden transfer of loads at that plane were major contributors to the failure of this building. A sketch of the building depicting sensor locations is shown in Figure 5.

System identification using GA optimization in the East-West direction indicates that the initial fundamental period of this building was about 0.7 sec. This period was elongated to 1.5 sec. towards the end of the record (Figure 6). Comparison of input elastic spectra at the base with a typical unreduced code spectrum for seismic zone 3, where this building was located, provides little to work with as far as damage assessments are concerned (see Figure 7). First, the elastic demand/capacity ratios in the E-W and N-S directions look about the same. Second, comparison of modal base shear demand and assumed capacities are not far apart from each other. Third, no information pertaining to the significant attributes of the building particular to this structure, such as irregularity, discontinuity of shear walls can be inferred from spectral comparisons. Fourth, the E-W and N-S picture do not vary by much although the building is significantly weaker in the E-W direction. Finally, no information regarding the possible distribution of damage throughout the height of the structure can be obtained from Figure 7. This illustrates the disadvantages of using design-based approaches as tools for automated post-earthquake damage assessment.

Instantaneous and maximum values of interstory drifts of CSMIP instrumented buildings after an earthquake can be easily and immediately estimated using tools such as CSMIP-3DV (Naeim et. al, 2004). These drift values were proven to be of immense value in automated damage assessment. A glimpse at the E-W and N-S lateral displacements and story drifts (Figures 8 and 9) reveals that the drift demands in the E-W direction were significantly larger

than those in the N-S direction. Furthermore, a drift of 3.5 inches at the first floor is inferred from sensor data in the E-W direction while the maximum drifts in the upper floors are limited to about 1.0 inch. Evaluation of the shear-displacement hysteretic plots (Figure 10) indicates significantly larger excursions and softening of the first floor in the E-W direction.

Surprisingly, completely independent approaches using interstory drift indices provide similar and very useful results. For example, if we use HAZUS-MH fragility curves based on interstory drifts for this type of building (C1M or C2M, older building), we obtain 85% probability of severe damage and 15% probability of moderate damage at the first floor in the E-W direction (see Figure 11). This is exactly where the column failures occurred. In the N-S direction at the same floor the probability of severe damage is estimated at less than 11% and probability of moderate damage at 78%. The damage at the upper floors of this building was limited as the failure of the first floor columns produced a relatively rigid pin-based block. This is also reflected in these damage estimates. In the E-W direction the probabilities of severe, moderate, slight and no damage are constant from the second floor to roof at 6%, 76%, 16% and 1%, respectively. In the N-S direction these values are 0%, 11%, 47%, and 42% respectively.

Use of the PEER/NSF fragility curves for flexural behavior of nonductile R/C columns provides similar useful information (see Figure 12). Based on this approach, the probability of severe damage to the first floor columns in the E-W direction is 74% and in the N-S direction is 19%. The probability of the severe column damage in upper floors is only 14% in the E-W direction and 0% in the N-S direction. The elegance of the PEER/NSF fragility curves is that the probability of damage based on various damage mechanisms and various components can be estimated. For example, using the fragility curves developed for old R/C beam-column joints, one obtains that the probability for beam-column joint severe damage throughout this building is 0% while the probability of slight damage to these joints is 81% at the first floor in the E-W direction.

Even FEMA-356 tables intended for nonlinear performance analyses such as Table 6-8 can be cast into a fragility curve for the purposes of automated post-earthquake damage assessment. For example, one can assume a certain level of elastic drift and apply some adjustment factors to take into consideration the inherent conservatism of FEMA-356 tabulated limit states. For instance, if we assume the building can take 0.005 of interstory drift angle within its elastic limit, do not apply any adjustment factors, and use the mean secondary values provided in FEMA-356 Table 6-8 for nonconforming columns in flexure (see Figure 13), then our damage assessment would indicate a 100% probability of exceeding the secondary Collapse Prevention (CP-S) for the first floor columns in the E-W direction (Figure 14). Based on this analysis, all columns in upper floors are within the Immediate Occupancy (IO) limit state.

In summary, use of sensor data to estimate interstory drifts and application of various fragility curves, if available at the time, could have provided excellent post-earthquake damage assessment of this building.

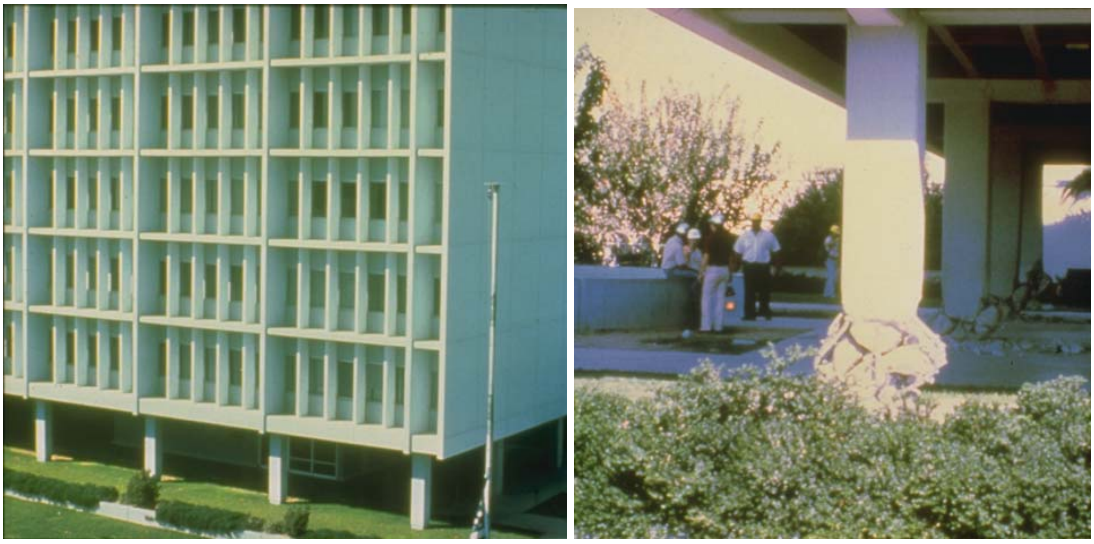

(a) A view of the building (b) Failure of columns at the base

Figure 4. Imperial County Services Building (Photo Credits: BAREPP and USGS)

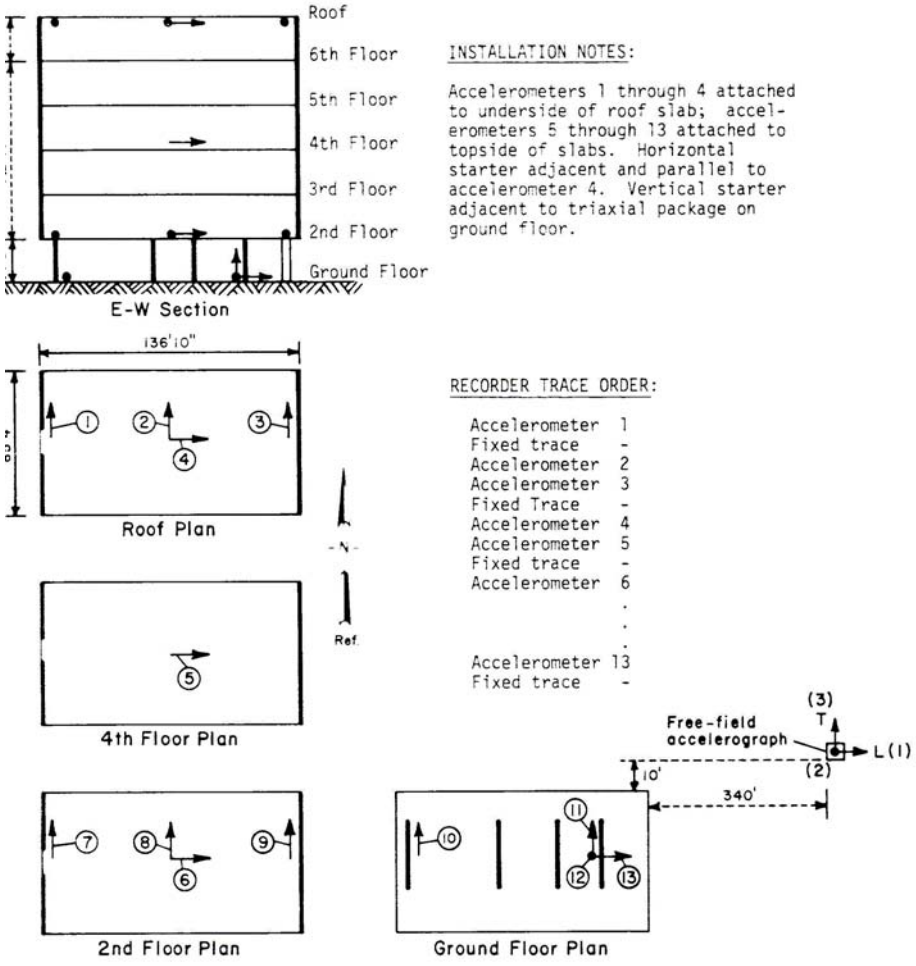


Figure 5. Sketch and sensor layout for Imperial County Services Building (from McJunkin and Ragsdale 1980)

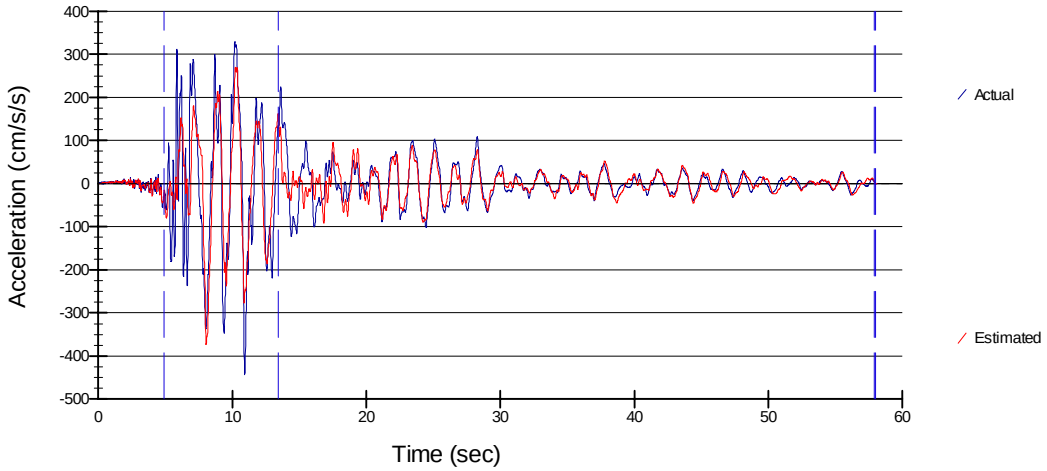


Figure 6. Recorded and GA identified response in the E-W direction at the roof.

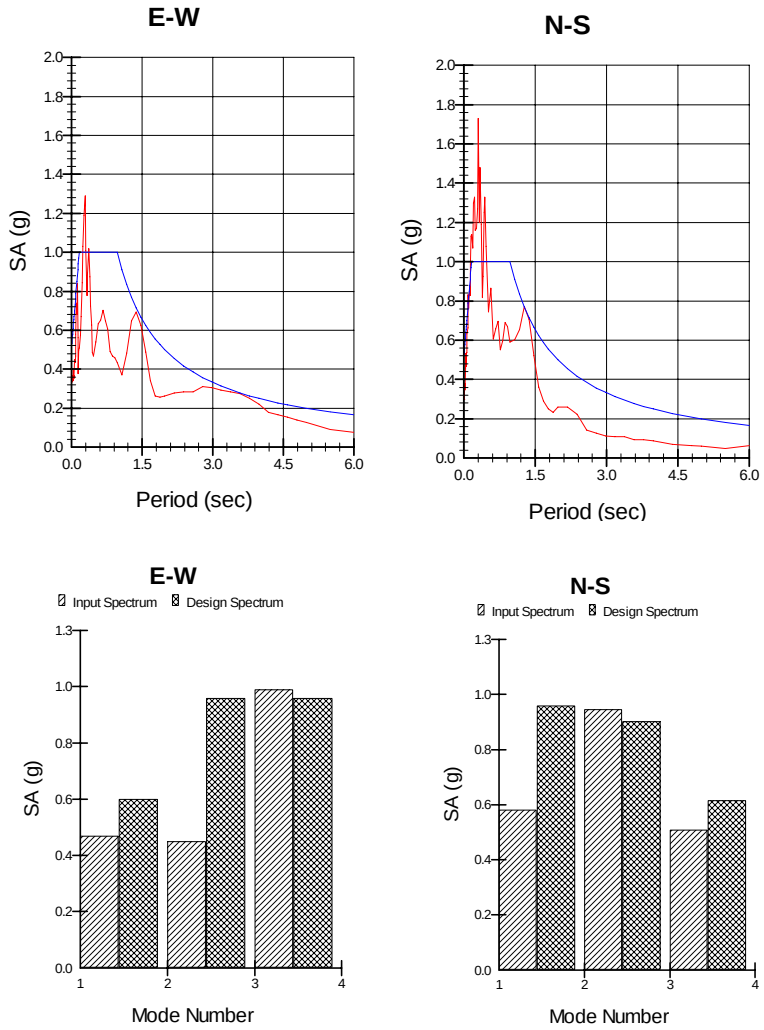


Figure 7. Comparison of the recorded response spectra (5% damped) at the base of the building with a typical "design" spectrum for seismic zone 3 and corresponding elastic modal demands for modes 1 to 3.

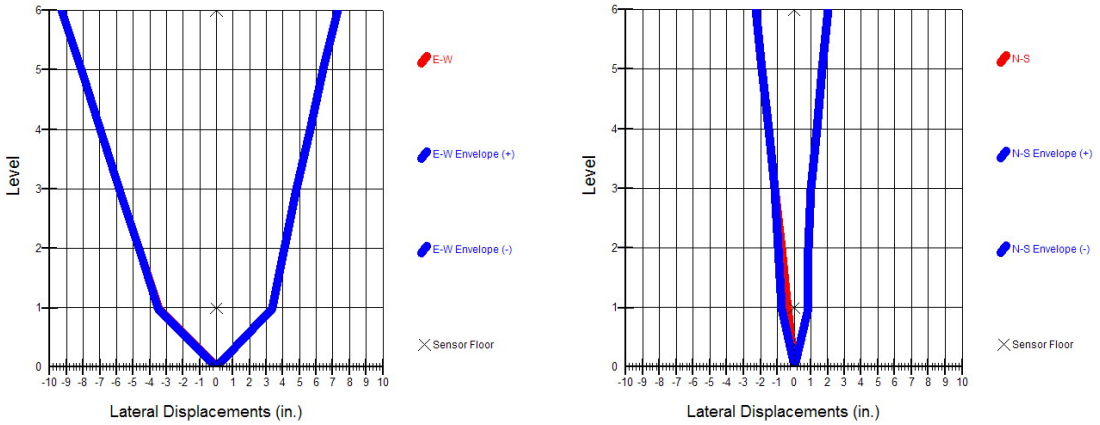


(a) E-W (b) N-S

Figure 8. Maximum lateral displacements in the E-W and N-S directions

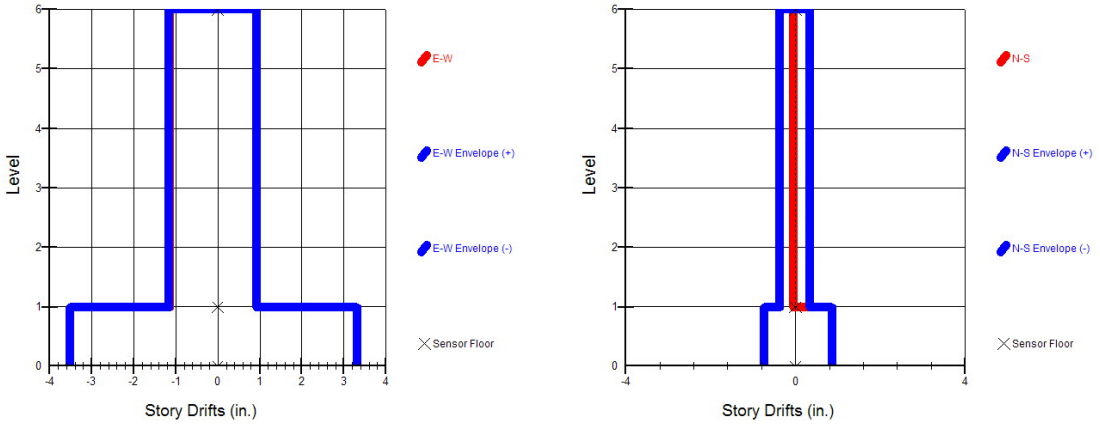


(a) E-W (b) N-S

Figure 9. Maximum intersory drifts in the E-W and N-S directions

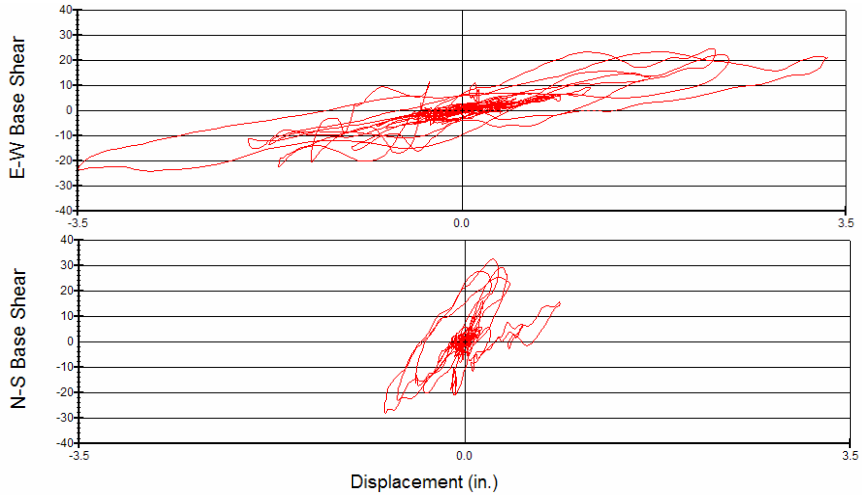


Figure 10. First floor shear-displacement hysteretic loops (E-W on top, N-S at the bottom)

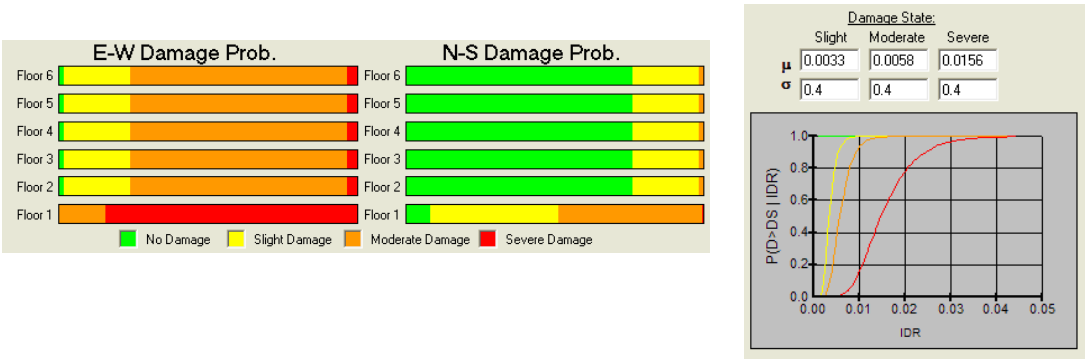


Figure 11. Damage probability established based on HAZUS-MH drift-based fragility curves for older concrete buildings clearly identifies the first floor in the E-W direction as the zone of severe damage.

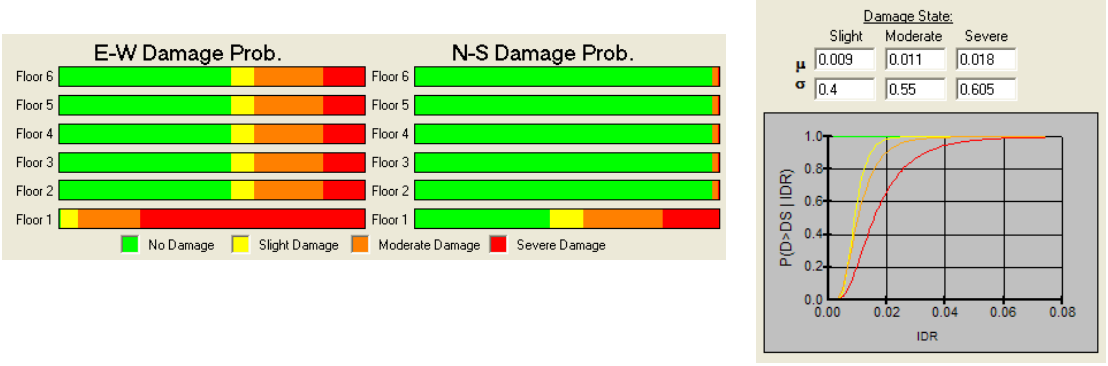


Figure 12. Damage probability established based on PEER/NSF fragility curves for nonductile R/C columns under large gravity loads clearly identifies the first floor columns in the E-W direction as the zone of severe damage.

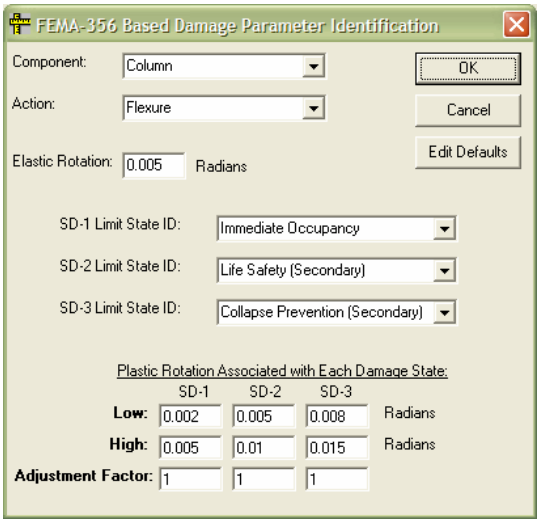


Figure 13. Assumptions used in converting FEMA-356 tabulated values to a fragility curve for nonductile R/C columns

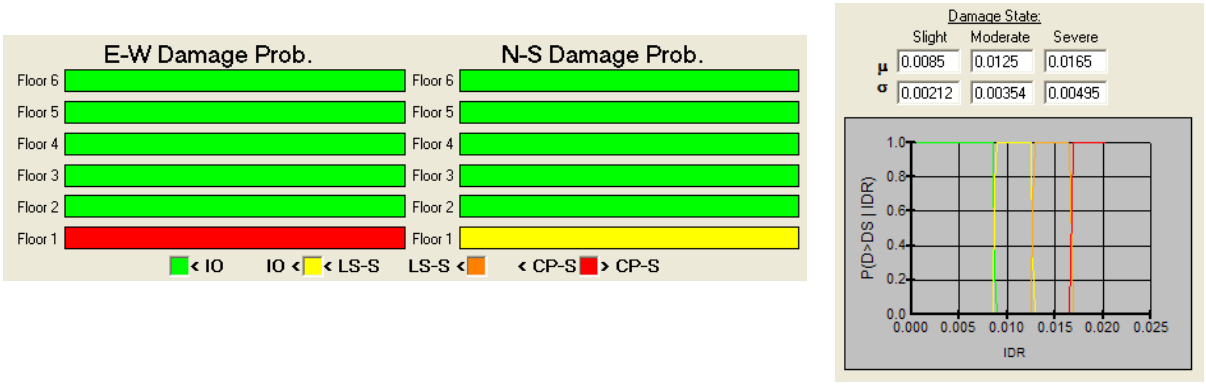


Figure 14. Damage probability established using Tables contained in FEMA-356 for limit-states of nonductile concrete columns clearly identifies the first floor in the E-W direction as the zone of severe damage.

## Example 2. The Van Nuys 7-Story Hotel (CSMIP ID = 24386)

This 7-story nonductile concrete frame building (Figures 15 and 16) is probably the most studied instrumented building in the world. We applied ADA to records obtained from three earthquakes: 1992 Landers, 1992 Big Bear, and 1994 Northridge earthquake. The building did not suffer damage during the 1992 events but did suffer significant structural damage during the 1994 Northridge earthquake in the form of shear failure of columns at the 4$^{th}$ floor on the exterior E-W frame on the south face of the building.


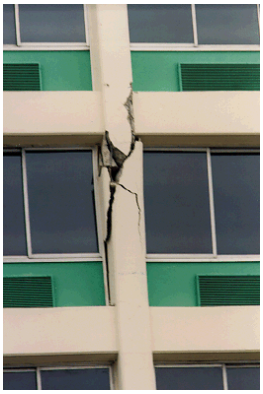

Figure 15. The Van Nuys 7-Story Hotel and damage to its fourth floor columns during the 1994 Northridge earthquake.

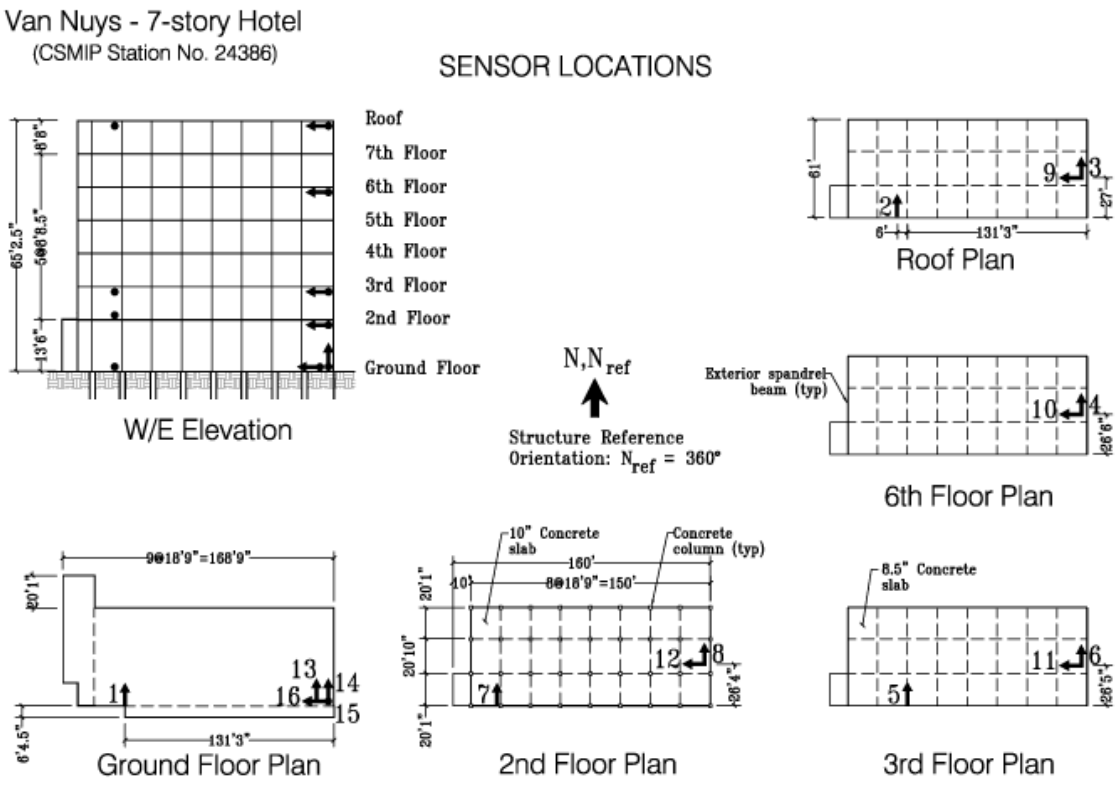


Figure 16. Sketch and sensor layout for the Van Nuys 7 Story Hotel.

Fragility analysis for 1992 Landers and Big Bear earthquakes using HAZUS-MH, PEER/NFS and FEMA-356 parameters all indicate that this building did not suffer structural damage during these two earthquakes (See Figure 17 for an example). The picture, however, is entirely different for the 1994 Northridge earthquake where all three methods indicate a high probability of extensive damage to the middle floors of the building (Figures 18 and 19). Please note that contrary to the Imperial Valley Services Building, no sensors were installed in this building on the floor that was damaged. Therefore, the estimates are provided by interpolation between sensors at other floors. As a result the ADA procedures assign possibility of damage to several floors in the building and cannot pinpoint the exact floor at which the damage occurs.

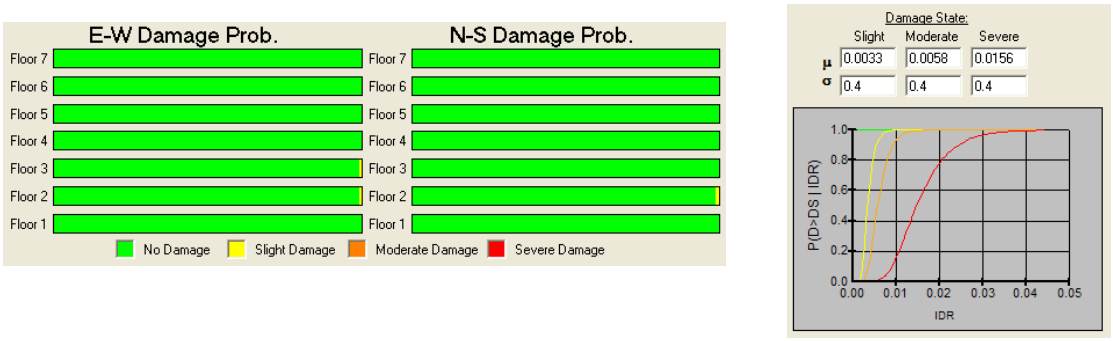


Figure 17. Damage probability established based on HAZUS-MH drift-based fragility curves for older concrete buildings indicates no damage during the Big Bear and Landers earthquakes.

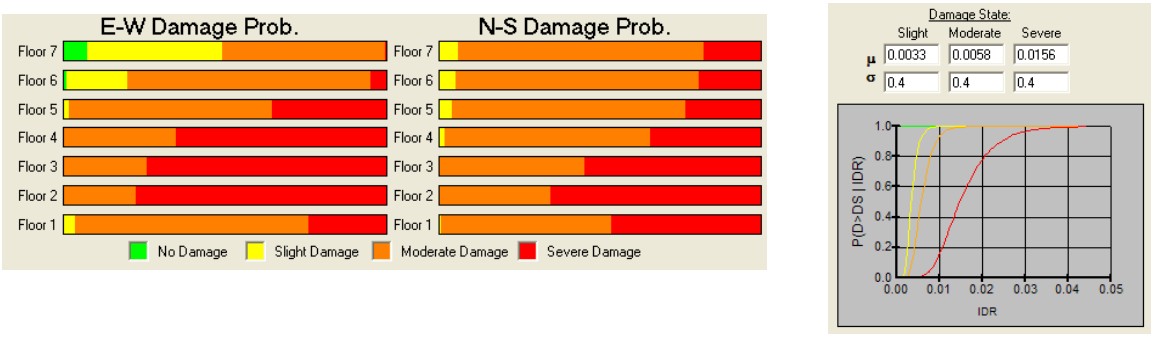


Figure 18. Damage probabilities established based on HAZUS-MH drift-based fragility curves for the 1994 Northridge earthquake show 100% probability of moderate to severe damage at the second to fourth floors.

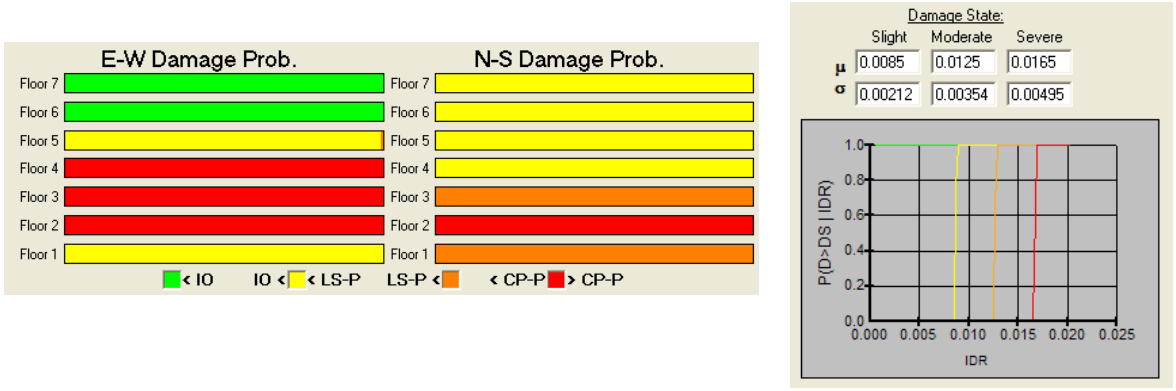


Figure 19. Damage probabilities established using FEMA-356 Tables indicate 100% probability of exceeding Collapse Prevention limit state at second to fourth floors in the E-W direction.

Our experience indicates that wavelet analysis shows promise if the results of wavelet analysis details are compared to those obtained from an earthquake in which the building was known to be not damaged (baseline earthquake). Otherwise, the possibility of false alarms based on wavelet analysis is high. Here, we use 1992 Big Bear as the baseline earthquake to estimate damage probability during the 1994 Northridge earthquake.

The amplitudes and details of wavelet analysis using a DB4 wavelet for various sensors are shown in Figure 20 where it can be seen that the detail content for the Northridge event is significantly richer than the corresponding details for the Big Bear event. Application of a simple fragility curve based on wavelet detail ratios obtained from several buildings with observed damage and the corresponding damage probabilities for the 1994 Northridge earthquake are shown in Figure 21. Notice that this procedure identifies the location of a virtual sensor at the 4$^{th}$ floor with the highest probability of damage at 92%. The results shown at the bottom for sensors 1 and 14 should be ignored because these are input sensors at the ground level. Unfortunately, obtaining more detailed damage estimates in terms of extent of damage (i.e., slight, moderate, severe) from wavelet analysis alone does not seem possible at this time.

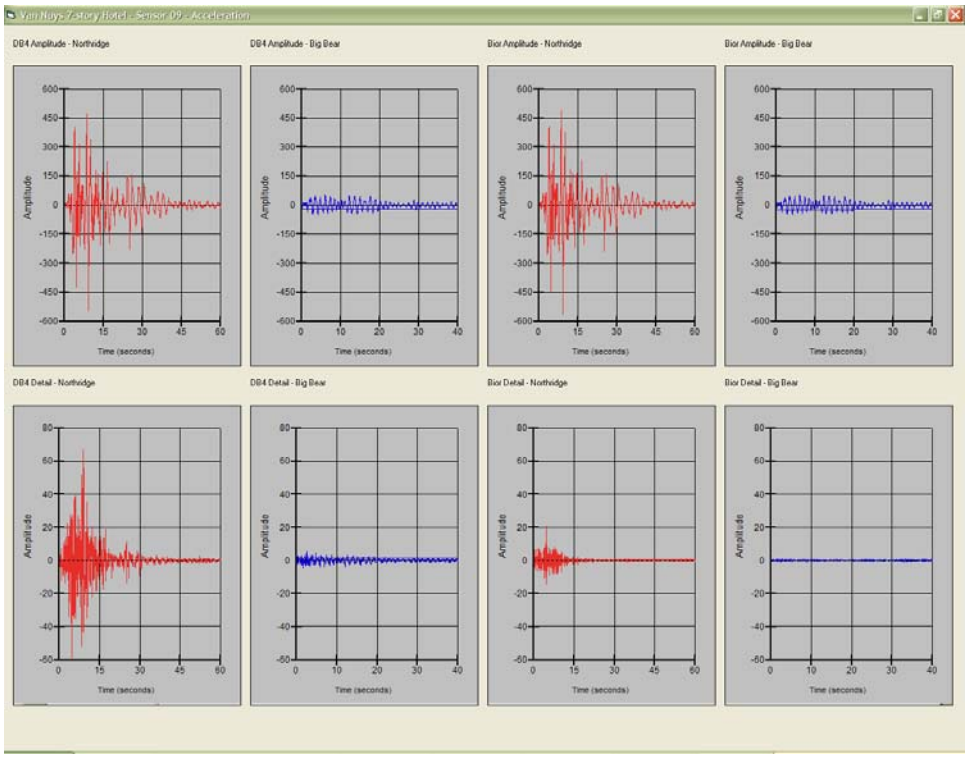


Figure 20. Amplitudes (top) and details (bottom) for a DB4 wavelet analysis of sensor data for the 1994 Northridge and the 1992 Big Bear earthquakes.

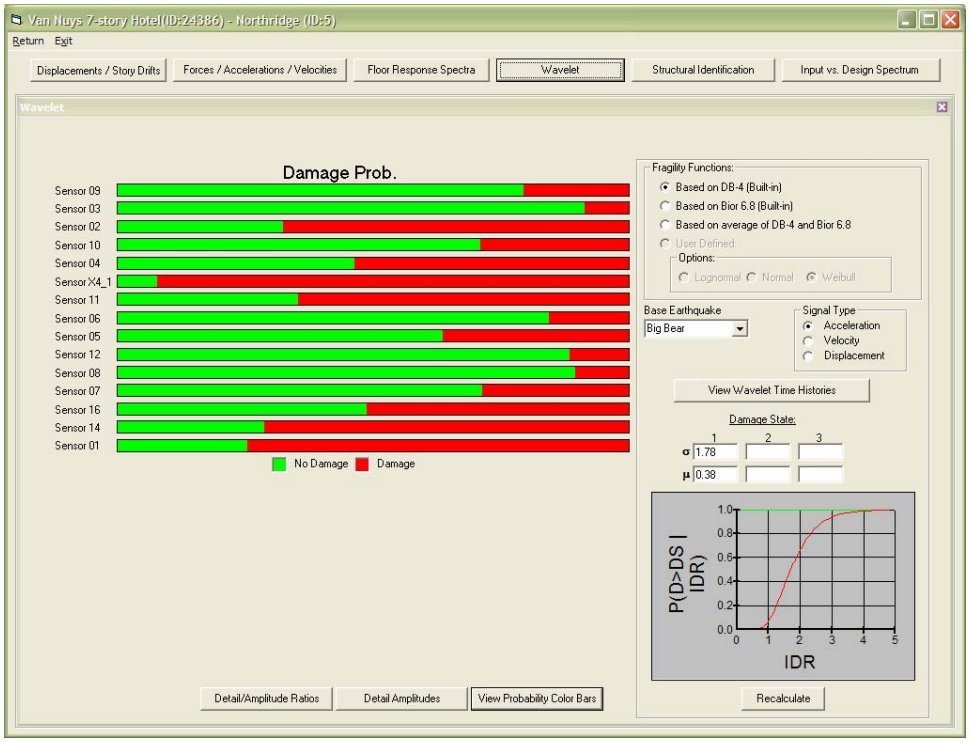


Figure 21. Damage probabilities obtained by wavelet analysis for the 1994 Northridge earthquake.

## Conclusions

A set of methodologies for automated post earthquake damage assessment of instrumented buildings were presented. It was shown that these methods can be used immediately after an earthquake to assess the probability of various damage states in the N-S and E-W directions and throughout the height of each building. The methods have been applied to more than 40 CSMIP instrumented buildings which have recordings from more than one earthquake. The results indicate that the proposed methods can provide extremely useful information regarding the status of a building immediately after an earthquake by simple and rapid analysis of sensor data and prior to any building inspections.

## Acknowledgments

Funding for this project was provided by State of California, California Geologic Survey, Strong Motion Instrumentation Program (SMIP) under Contract Number 1003-781.

The authors wish to express their gratitude to the members of the consulting panel of experts consisting of Professors Wilfred Iwan, S.T. Mau, and Eduardo Miranda.

The opinions expressed in this paper are those of the author and do not necessarily reflect the views of the California Strong Motion Instrumentation Program or John A. Martin and Associates, Inc.

## References

Alimoardi, A., and Naeim, F., 2005a, *Identification of Linear and Nonlinear Seismic Response using Genetic Algorithms*, in preparation.

Alimoardi, A., Miranda, E., Taghavi, S, and Naeim, F., 2005b, *Automated Identification of Linear and Nonlinear Structural Systems using Genetic Algorithms and Approximate Mode Shapes*, in preparation.

American Society of Civil Engineers (ASCE), 2000, *Prestandard and Commentary for the Seismic Rehabilitation of Buildings*, Washington, D.C.

Applied Technology Council (ATC), 1989, *Procedures for Postearthquake Safety Evaluation of Buildings*, Redwood City, CA.

Aslani, H., and Miranda, E., 2003, "Probabilistic Assessment of Building Response During Earthquakes," in *Applications of Statistics and Probability in Civil Engineering*, Der Kiureghian, Madanat and Pestana (eds), Millpress, Rotterdam.

California Strong Motion Instrumentation Program (CSMIP), 1995, *Processed Data for Los Angeles 2-story Fire Command Control Building from the Northridge Earthquake of 17 January 1994*, Report No. OSMS 95-01A.

Federal Emergency Management Agency (FEMA), 2004, *HAZUS-MH Technical Manual*, Washington, D.C.

McJunkin, R.D., and Ragsdale, J.T., 1980, *Compilation of Strong Motion Records and*

*Preliminary Data from the Imperial Valley Earthquake of 15 October 1979*, Preliminary Report 26, Office of Strong Motion Studies, California Division of Mines and Geology, Sacramento, CA.

Miranda E., and Taghavi S., (2005) "Approximate Floor Acceleration Demands in Multistory Buildings: I Formulation," Journal of Structural Engineering, Vol. 131, No. 2, pp. 203-211, American Society of Civil Engineers.

Naeim, Farzad, 1997, *Performance of 20 Extensively Instrumented Buildings during the 1994 Northridge Earthquake – An Interactive Information System,* A report to CSMIP, John A. Martin & Associates, Inc.

Naeim, F., Lee, H., Bhatia, H., Hagie, H., and Skliros, K., 2004, "CSMIP Instrumented Building Response Analysis And 3-D Visualization System (CSMIP-3DV)," Proceedings of the SMIP-2004 Seminar.

Naeim, F., H., Hagie, H., Alimoradi, A., and Skliros, K., 2005, *Automated Post-Earthquake Damage Assessment and Safety Evaluation of Instrumented Buildings,* A report to CSMIP, John A. Martin & Associates, Inc., in preparation.

Porter and Kiremidjian, 2001, *Assembly-Based Vulnerability of Buildings and its Uses in Seismic Performance Evaluation and Risk-Management Decision-Making,* Report No. 139, John A. Blume Earthquake Engineering Research Center, Stanford, CA

Revadigar, S. and Mau, S.T., "Automated Multi-criterion Building Damage Assessment from Seismic Data," Journal of Structural Engineering, ASCE, Vol. 125, No. 2, Feb., 1999, pp. 211-217.

# A DATA DRIVEN METHODOLOGY FOR ASSESSING IMPACT OF EARTHQUAKES ON THE HEALTH OF BUILDING STRUCTURAL SYSTEMS

Dionisio Bernal[1] and Eric Hernandez[2]

[1] Associate Professor, Civil and Environmental Engineering Department, Center for Digital Signal Processing, Boston, MA.
[2] Graduate Student, Northeastern University, Boston, MA,

## Abstract

A data-driven approach for post-earthquake posting of buildings is presented. The approach is based on the analysis of residuals obtained by subtracting the measured responses from reference signals that reflect the behavior of the healthy system. The residuals are used to compute two indices from which the impact of the motion on the structure is assessed. One index measures the extent of nonlinearity and the other looks at changes in structural characteristics after the strong motion part of the record is over. Results obtained for a number of buildings taken from the CSMIP database suggest the approach may be suitable for automated posting.

## Introduction

An item that has come to the forefront of the earthquake engineering agenda is assessing the state of health of structural systems after violent ground motion. The matter is of significant practical and economical importance given that assurance of structural safety is required before structures can be reoccupied following a major earthquake. At the present time post-earthquake assessment of structural health is based on visual inspections [1].

Although use of sensor data to asses the impact of earthquakes on structural systems is appealing, the idea has proven difficult to implement successfully. Work on using instrumental data to asses the impact of earthquake motion has been mainly focused on looking at the evolution of "effective fundamental period" [2,3,4]. The basic premise being that elongation of the "effective period" during the motion is an indication of softening and, therefore, of damage. The approach, which suffers from the fact that the feature used cannot be objectively defined (since there is no "effective period" at a given point in the response of a nonlinear system), has not proven robust in real applications.

This paper presents a new strategy to characterize the impact of earthquake motions in buildings. The approach is based on contrasting the measured response with the response of a fictive system whose behavior reflects the characteristics of the system in its reference (healthy) state. The responses of the reference state are computed through a partial observer model that is formulated using data from a non-damaging event. While the details of the observer are best explained in the body of the paper, the scheme essentially operates as a sequence of maps connecting each channel to all the others. The paper presents the mathematical support of the technique and illustrates its application in detail in the context of one particular case using real data. In addition, a summary of results for a number of building-earthquake pairs taken from the CSMIP database is also included.

## The Basic Scheme in Open Loop Operation

Assume that data from a non-damaging event is available and that this data is used to obtain a map from input to output. The map can take various forms, in the time domain, for example, it could be specified in terms of the matrices of a state-space realization or in the form of a weighting sequence description (pulse response) or perhaps in an ARX model where the auto-regression part leads to a particularly concise representation. Assume that at a later time the structure is subjected to another earthquake and the formulated map, together with the new measured input, is used to estimate the output. If the structural response to the current earthquake is linear and the map is accurate (for the reference state) one anticipates that the measurements and the predictions will be in good agreement. If, on the contrary, the structure experiences significant nonlinearity the measurements and the estimates from the map will not match and the discrepancy provides a useful characterization of the nonlinear behavior experienced (the important issue regarding discrimination between nonlinearity and permanent damage is commented on later). Indeed, at each channel one has two curves: 1) the measured signal and 2) the estimate of what the signal "would have been" if the response was governed by the structural properties that prevailed during the non-damaging event used to formulate the map. The scheme outlined is depicted schematically in fig.1, where we refer to it as the Open Loop Model to emphasize that the path in the analytical estimates is from input through the model to the output.

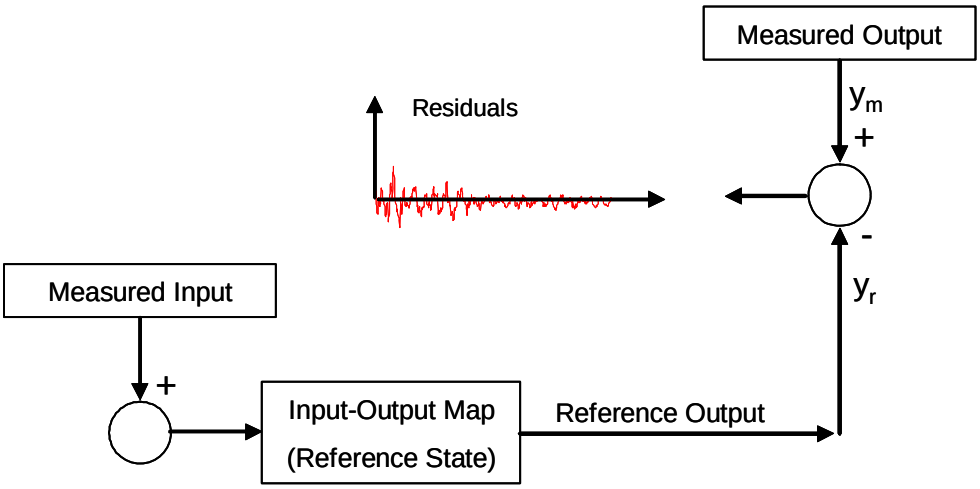


Fig.1 Computation of residuals using a basic open loop scheme

### *Factors Limiting the Accuracy of the Open Loop Scheme*

Accuracy in $y_r$ in fig.1 means that the response that is estimated by using the input-output map is a good approximation of the response that "would have been" measured if the structure had retained the properties that prevailed during the non-damaging event. A number of factors, however, conspire to produce non-negligible residuals, even when the response to the new motion does not induce damage (and this holds even in steel structures, where one cannot use the argument of variations due to different micro-cracking and so on). There are several factors that can contribute to making the residuals non-negligible for motions that do not induced damage

but the most important one is the fact that the input-output (open loop) map reflects a *linearized* version of the compliance for the degrees-of-freedom (DOF) that are not prescribed at the soil-structure interface. Indeed, if one inspects the way the motion enters into the building from the ground it is evident that to perfectly isolate the structure from the soil and say "this collection of signals is the prescribed motion" and all the responses measured elsewhere are causally related to it, is a difficult proposition. The foregoing is not intended to imply that SSI is usually important (in a design sense) but simply that operating with a system that reflects compliance leads to a degradation in the level of accuracy that would otherwise be attainable if the map reflected only the properties of the structure.

Work to reduce the residuals in cases where the structure behaves (essentially) as a linear system led to a modification of the open loop strategy which we have referred to as the Partial Observer (PO) model. In simple terms, the idea is that instead of thinking in the strict terms of input-output one can divide the available signals into a "predictor set" and a "target set" and use the predictors to anticipate the targets. As will be apparent from subsequent developments, the mathematical structure of the observer effectively eliminates the influence of compliance on the map, increasing the accuracy notably. Before we embark on describing the details of the PO model it is opportune to take a brief detour and comment on the matter of variability in the characteristics of the base motion.

Changes in Frequency Content

Implicit throughout the discussions presented in this section is the fact that the model identified during the non-damaging event "exists" in a bandwidth that is adequate for estimating the reference response to the subsequent inputs. Since the frequency content of the ground motion can change from event to event due to variations in source to site distance, focal mechanism and/or magnitude, difficulties from a potential dependency of the input-output map on the characteristics of the input may be problematic. Upon close examination, however, one concludes that no substantial problem is anticipated on this account. One reason has to do with the observer structure used to compute the reference response, and this will be best appreciated after the next section is completed. Another reason, however, has to do with the fact that the mapping is done in the time domain where, given that the structure starts vibrating from an (essential) at rest condition, many modes that may be poorly excited can be "viewed" during the early part of the response.

An alternative way to state the same thing is to note that although the Fourier spectrum may be very low at some frequencies when the complete motion duration is considered, the evolution to the final form starts from a wide band function, independently of the details of the input. This last point is illustrated in fig.2 which displays the evolution of the Fourier amplitude spectrum for a sine function with a 10Hz frequency, modulated by a box window whose width varies from ½ to 5 cycles. As expected, the Fourier transform becomes steep and narrow with a center at 10Hz as time increases but the envelope of the evolving spectra shows important non-zero amplitudes at all frequencies in the displayed bandwidth.

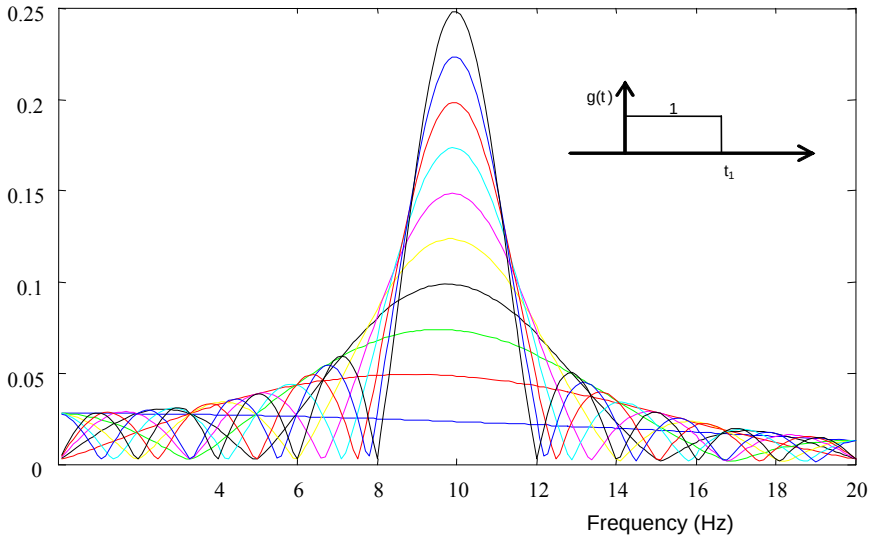


Fig.2 Evolution of the Fourier amplitude spectrum for the signal $f(t) = \sin(20\pi t).g(t,t_1)$ (10 plots corresponding to $t_1 = 0.05, 0.1,.. 0.5$ sec).

## The Partial Observer Model

As noted previously, the problem with the open-loop model lies in fact that we do not have sufficient information on the input (to the non-interacting structure) to allow the computation of residuals that are as small as we would like in cases where there is no damage. In this section we present a solution to this problem based on the use of an "augmented input vector" which contains the input and some output signals. Assume we have a linear time invariant finite dimensional linear system with a state space parameterization in discrete time given by

$$x_{k+1} = Ax_k + Bu_k \tag{1}$$

$$y = C x_k \tag{2}$$

where we've taken the direct transmission term equal to zero because this happens to be the case when one is dealing with base excitation. In the previous expressions A, B and C are: the system, input to state influence, and state to output mapping matrices, in discrete time, and *x* is the state vector. In the order presented these matrices belong to $R^{NxN}$, $R^{Nxr}$ $R^{mxN}$ $R^{Nx1}$, where N is the order of the system and *r* and *m* are the number of inputs and outputs respectively.

### A Full Observer Model

It is appropriate to begin by developing what we refer to as a Full Observer (FO) model. Adding and subtracting to the state recurrence the output multiplied by some gain, G, one gets

$$x_{k+1} = (A - GC)x_k + [B\ G]\begin{Bmatrix} u_k \\ y_k \end{Bmatrix} \tag{3}$$

which, with obvious notation can be written as

$$x_{k+1} = \overline{A}x_k + \overline{B}\,\nu_k \tag{4}$$

Following the sequence in eq.4 for k = 1,2,3, etc one can find an expression for the state at step k in terms of the state at zero and the compound input $\nu_k$ from k = 0 to k-1 which, upon substitution into eq.4 gives

$$y_k = C\overline{A}^k x_0 + \sum_{j=1}^{k} \overline{Y}_j \nu_{k-j} \tag{5}$$

where the Markov parameters of the FO model, $\overline{Y}_j$, are given by

$$\overline{Y}_j = C\overline{A}^{j-1}\overline{B} \tag{6}$$

Assuming the pair {A,C} to be observable there is a gain G that renders $\overline{A}$ nilpotent so, for some exponent $k \geq p$, $\overline{A}^k = 0$ and, taking the initial condition as zero one can write

$$\begin{bmatrix} y_{1,1} & y_{1,2} & . & y_{1,\ell} \end{bmatrix} = \begin{bmatrix} \overline{Y}_1 & \overline{Y}_2 & . & \overline{Y}_p \end{bmatrix} \begin{bmatrix} \nu_0 & \nu_1 & . & \nu_{\ell-1} \\ 0 & \nu_0 & . & \nu_{\ell-2} \\ . & 0 & . & . \\ 0 & 0 & . & \nu_{\ell-p} \end{bmatrix} \tag{7}$$

or, introducing obvious notation

$$y = \overline{Y}V \tag{8}$$

where $V \in R^{(m+r)p \times \ell}$ is Toeplitz and $\ell$ = number of the last time station considered. Taking $\ell$ sufficiently large the matrix V can be made wide and the least square solution for the Markov parameters of the FO model is

$$\overline{Y} = V^* y \tag{9}$$

where * stands for pseudo-inversion.

***From Observer Markov Parameters to Markov Parameters***

A last piece of background needed before introducing the Partial Observer (PO) model is clarification of the connection between the FO Markov parameters and the Markov Parameters

(MP) of the original system, which we designate as Y. The MP connect the input to the output and are given by eq.6 with $\overline{A}$ and $\overline{B}$ replaced by A and B, namely

$$Y_j = CA^{j-1}B \tag{10}$$

From a physical perspective $Y_j$ is a matrix containing, in column *q*, the measurements at all the *m* output sensors due to a unit pulse applied at the $q^{th}$ input. Because of their slow decay, the MPs are best computed from the Markov's of the FO in a recursive fashion. The governing expression is [5]

$$Y_k = \overline{Y}_k^{(1)} + \sum_{j=1}^{k-1} Y_j \overline{Y}_{k-j}^{(2)} \tag{11}$$

where the superscript (1) refers to the first *r* columns of $\overline{Y}$ and the subscript (2) to the remaining *m* columns (recall that *r* is the number of inputs and *m* the number of outputs).

### *Response in Terms of Markov Parameters*

In terms of the MP the response can be expressed as

$$y_k = \sum_{j=1}^{k} Y_j u_{k-j} \tag{12}$$

Note that the representation of the output as function of the input and the output at a finite number of prior steps (eq.6) is the vector form of the widely used ARX structure. Likewise, the representation in eq.12 connecting the output exclusively to prior inputs is the weighting or pulse response sequence representation.

### *The Partial Observer Model*

Consider eq.2 with the output signals partitioned into two sets with the *t* and the *p* superscripts suggesting *target* and *predictors*, namely

$$\begin{Bmatrix} y^t \\ y^p \end{Bmatrix} = \begin{bmatrix} C^t \\ C^p \end{bmatrix} x_k \tag{13}$$

defining

$$\overline{Y}_j^t = C^t \overline{A}^{j-1} \overline{B} \tag{14}$$

one can write

$$y_k^t = \sum_{j=1}^{k} \overline{Y}_j^t v_{k-j} \tag{15}$$

We now indulge in a bit of mental gymnastics. Consider a fictive system with an "augmented input vector" given by

$$v_k^t = \begin{Bmatrix} u_k \\ y_k^p \end{Bmatrix} \tag{16}$$

and output given by $y^t$. Reviewing the previous definitions one concludes that, for this system, eq.14 gives the FO Markov parameters and, consequently, the MP of this fictive system, $Y^t$, can be obtained from eq.11 by replacing $\overline{Y}$ with the appropriate partitions from eq.16. The output at the target set given the Markov parameters and the predictors in eq.16 is then

$$y_k^t = \sum_{j=1}^{k} Y_j^t v_{k-j}^t \tag{17}$$

Eq.17 predicts the output at an arbitrarily selected set of channels (the *t* set) using the augmented input of eq.16. It's opportune to note that the form in eq.17 is not autoregressive, since there is no intersection between the signals in the right and the left side of the equal sign, and it is not a weighting sequence either (in the traditional sense) because the right side includes not only the input, but also part of the output. The form in eq.17 is what we refer to as the Partial Observer (PO) model.

## Observer Structure

The result in eq.17 can be viewed in terms of the observer like structure depicted schematically in fig.3

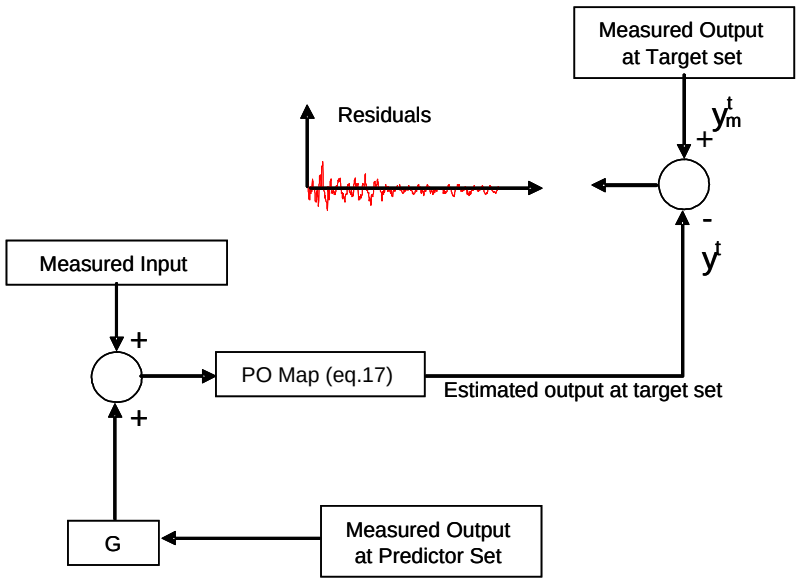


Fig.3 Schematic illustration of the Partial Observer Scheme

At this point it should be apparent why the target channels are not included in the predictor set. Namely, we wish to control the effect of unmeasured inputs and to isolate SSI effects but otherwise allow the target channels to respond freely - namely:

*The target output obtained from the observer is the response that the linear system of the reference state would have if subjected to the measured inputs and to prescribed motions equal to the measurements at the channels in the predictor set.*

***Selection of the Target and the Predictor Sets***

Given that the fundamental objective of the "feedback" from $y^p$ is to isolate the effect of unmeasured base motions it appears that the channels in the lowest instrumented level of the building are a good choice for this set. In this scheme damage occurring between the foundation and the first instrumented level would be addressed by switching the $y^p$ and the $y^t$ sets, although one anticipates that in this case the foundation effects would be less effectively isolated.

Another possibility is to place all the channels in the predictor set, except for one at a time, which is treated as the target and to proceed by formulating one map for each channel. This alternative maximizes isolation of the structure from SSI and any unmeasured disturbances but also reduces sensitivity of the residuals to inelastic behavior. A review of the mathematical developments of the previous section shows that the formulation of all the maps can be done directly from the FO Markov parameters and, as a consequence, the computational burden in this alternative is not much larger than in the first case.

In deciding between the two alternatives we contemplated one more factor, namely, the fact that the dynamics of the model in the second alternative are simpler than in the first because each channel that is moved to the predictor set eliminates two eigenvalues from the system matrix of the "augmented input" system. Given that this simplification adds to robustness, and that robustness is of the essence, we opted for the second alternative.

***On the Selection of p***

The only user decision in the approach to obtain the PO model is the selection of the number of non-zero observer Markov parameters ($p$) in eq.7. Notwithstanding minor caveats because of details in the inter-step behavior of the input, in an ideal situation of noise free data the value of $p$ does not need to be larger than the order of the system divided by the number of output measurements.

In a realistic noisy environment, however, a more useful result is that the product of $p$ and the number of outputs is the maximum number of modes that can be identified if the Markov parameters of eq.10 are used in a realization algorithm. Given that the number of system modes that can be extracted from real data is not too large, when the objective is to compute frequencies and mode shapes the typical approach is to specify $p$ such that $p_x m$ is larger than what experience shows can be reasonably computed and then proceed to separate computational modes from system modes [6]. This last step, i.e., the discrimination between system and computational

modes, however, is a difficult problem for which no entirely satisfactory solution is currently available (although major gains appeared to have been made in the last couple of years with the introduction of the POLYMAX technique [7,8].

In any event, the point to stress here is that in our application there is no pressing need to "clean out" computational modes since these have very small contributions to the map and prove immaterial in the evaluation of residuals. In the current automated implementation of the PO model we've taken $p=2*NS$, where $NS$ is the number of stories of the building. In the unlikely event that the maps obtained are not sufficiently accurate with $p=2*NS$ (gauged with metrics that compare the measurements with the predictions in the reference state) the value is increased until the criterion is satisfied. If $p > 30$ seems necessary for an accurate map this is taken as an indication of anomalies, namely, either the structure is behaving with significant nonlinearity, which invalidates the selected record as reference motion, or there are faulty sensors in the set.

### *Comparison of Open Loop with PO Model*

Before proceeding to examine the processing of the residuals it is useful to illustrate how the predictions of the PO model are significantly more accurate than those from the open loop system for realistic operating conditions. For this purpose consider the 6 story building at CSMIP station #24370 (Burbank). We focus attention on channel #3 which is located on the roof and is oriented in the E-W direction. Assume that two identification models are obtained using data taken from the response to the Whittier Earthquake of 10/01/1987. The first model is the open loop model that predicts the output in channel #3 using the excitation at the base and the second is the PO model. The measured response is compared in Fig.4b with the open loop prediction and in Fig.4a with the PO model – the improved accuracy of the PO model is evident.

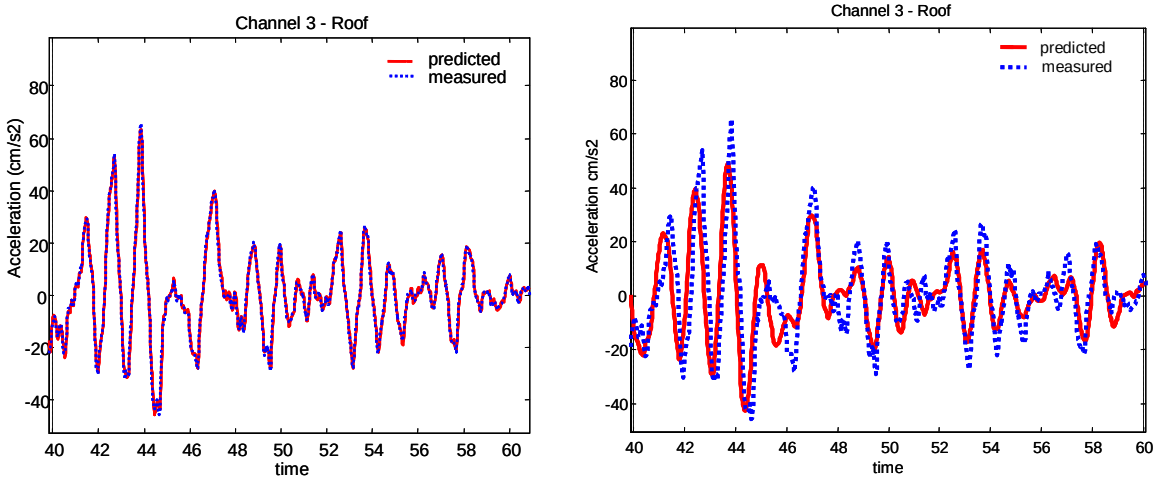


Fig.4 a) PO model predictions b) Open loop model

## Residuals

The objective of the work reported here was to provide a post-earthquake automated health assessment compatible with the current ATC-20 posting scheme. To attain this objective there is a need to reduce the time histories of the residuals to metrics that can be used in a

classification scheme. After exploring various alternatives we settled on two scalars, η and κ, in particular

η - is a measure of the total deviation of the measured response from linearity. Based on the aggregate of the numerical results examined $\eta < 0.20$ is proposed as equivalent to the ATC-20 posting INSPECTED.

κ - is a parameter used to differentiate inelastic response with no permanent damage from cases where the structure does not revert back to the original state after the strong motion ceases. Computation of κ is relevant only when $\eta > 0.20$.

The previous metrics are defined by

$$\eta = \gamma_{t=t_{max}}\Big|_{\text{max over all channels}} \tag{18}$$

$$\kappa = \frac{S_e}{S_r}\Big|_{\text{max over all channels}} \tag{19}$$

where

$$\gamma(t) = \frac{\int_0^t \varepsilon^2 dt}{\int_0^{t\,max} y_m^2 dt} \tag{20}$$

$$\varepsilon = y_p - y_m \tag{21}$$

where, $y_p$ = output predicted by the PO model (for the channel in question); $y_m$ = measured output and $t_{max}$ = total duration of the earthquake record.

The numerator in eq.19 is the average slope of the curve given by eq.20 computed after it reaches 95% of its final value. The denominator is the slope of a line joining the 10% to the 90% values of the function in eq.20 for the earthquake used to generate the PO model. It's worth noting that the denominator ($S_r$) would, ideally, be an estimate of the initial slope of the same curve used to compute the numerator (prior to the onset of inelastic action) but this definition does not prove practical because the time available to ascertain this average slope is too small to ensure robustness.

## Instrumental Automated Posting

In keeping with the objective, the information from the PO model has been mapped to the three group scheme adopted in the ATC-20 posting procedure [1]. The resulting Instrumental Automated Posting (IAP) approach, as tentatively defined, is summarized in Fig.5.

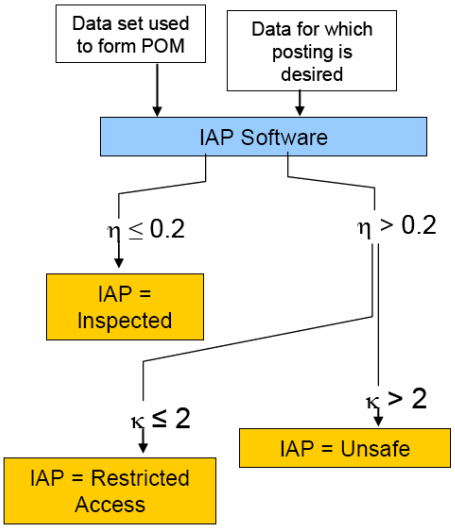


Fig.5 Instrumental Automated Posting Scheme

## Detailed Illustration

We illustrate the procedure by looking at the well known Van Nuys 7-story Hotel. As shown in fig.6, the structure has 16 sensors. The impacts of two earthquakes on the building are investigated: one is the Big Bear earthquake of 1992, which did not produce any damage, and the other the Northridge earthquake of 1994 which induced significant damage.

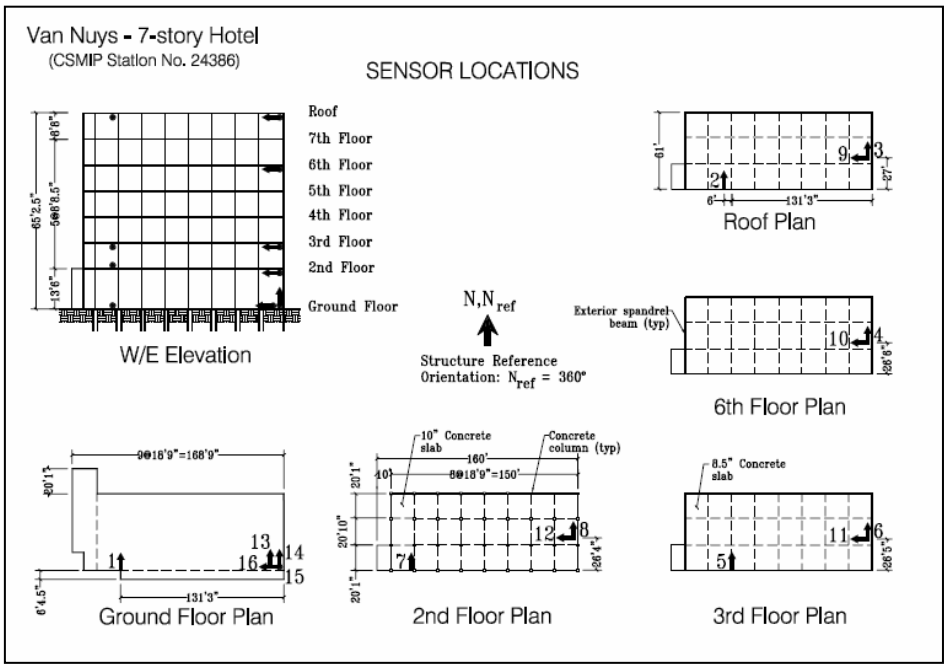


Fig.6. Schematic illustration of building and sensor location (taken from CSMIP web site)

## Formulation of the PO Model

To PO model is formulated using the Landers Earthquake of 1992. For this earthquake the maximum base acceleration recorded was 0.06g, and the maximum acceleration elsewhere in the structure was 0.19g, which are modest values and thus damage is not anticipated and none was observed.

## Case 1. Big Bear, 1992.

The maximum recorded base acceleration for this motion is 0.03g, and the maximum structural acceleration 0.06g. The intensity of shaking is, therefore, significantly smaller than that induced by the Landers motion used to generate the PO model. Fig.7 shows a comparison between the measured and predicted response at the channel where the largest residual is obtained (ch.12-1$^{st}$ Floor). As can be seen, the residual is very small and one would conclude (by inspection) that there was no damage in the response to this event – which was the case. In terms of the IAP outlined in fig.5 one finds $\eta = 0.06$ which is well bellow the 0.2 cutoff so the structure is classified as INSPECTED.

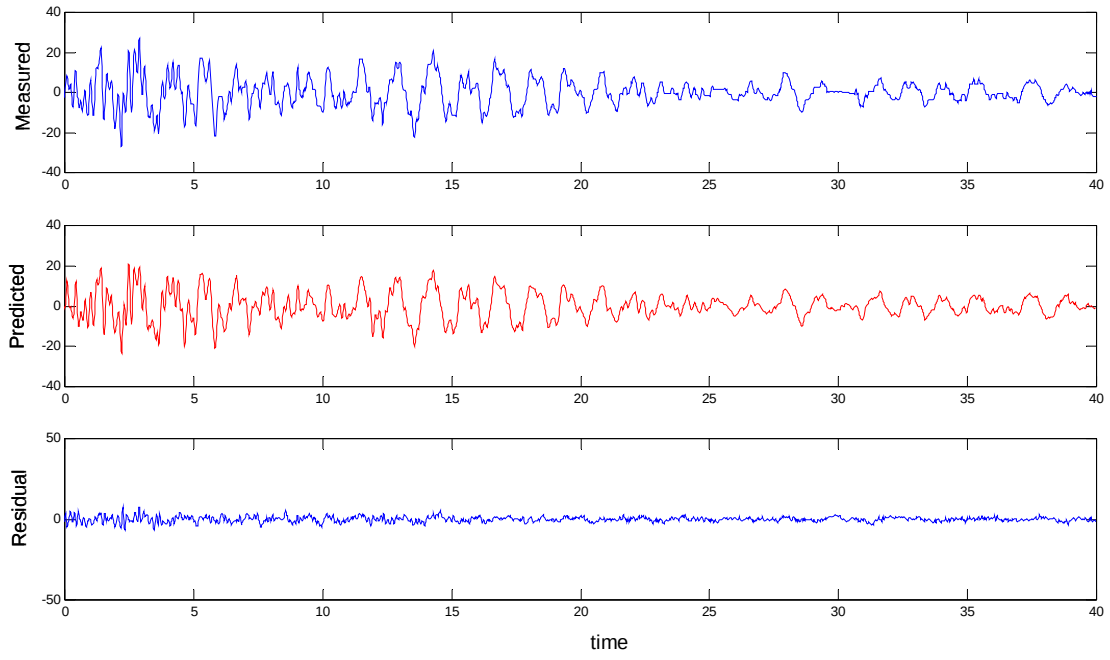


Fig. 7. Comparison of Measured and POM reference accelerations (cm/s$^2$) at channel 12 during Big Bear.

For illustration, the plot of $\gamma$ as a function of time for channel 12 is depicted in Fig. 8.

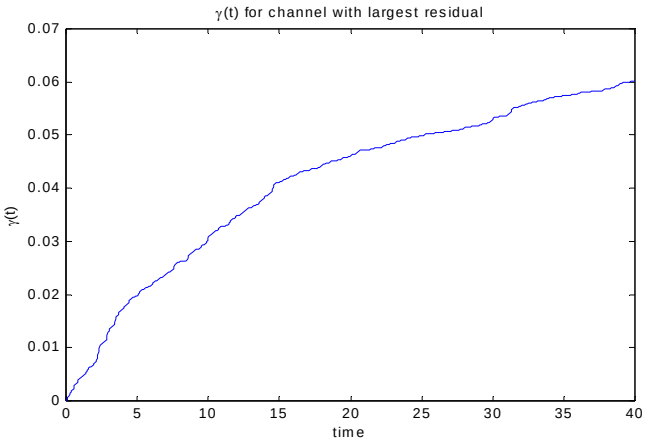


Fig. 8. γ for channel #12.

## Case 2. Northridge Earthquake, 1994.

The maximum recorded base acceleration for this earthquake was 0.49g and the maximum recorded acceleration on the structure 0.59g. The measured and the PO model reference response at the channel where the largest residual is obtained (ch.9-roof) are depicted in fig.9. The value of η proves to be 0.55, which is significantly larger than the threshold (0.2) bellow which no damage is anticipated. Given that the methodology indicates that the building has suffered significant nonlinearity one proceeds to determine if the nonlinearity led to permanent changes in stiffness. In the IAP approach this is done by looking at the parameter κ which, in this case proved to be 20.33, which is much larger than the threshold of 2 below which the structure would be assumed to have suffered nonlinearity but no substantial permanent damage. For the (η,κ) pair obtained, namely (0.55, 20.33) the IAP leads to a classification of UNSAFE which, of course, is consistent with the field observations.

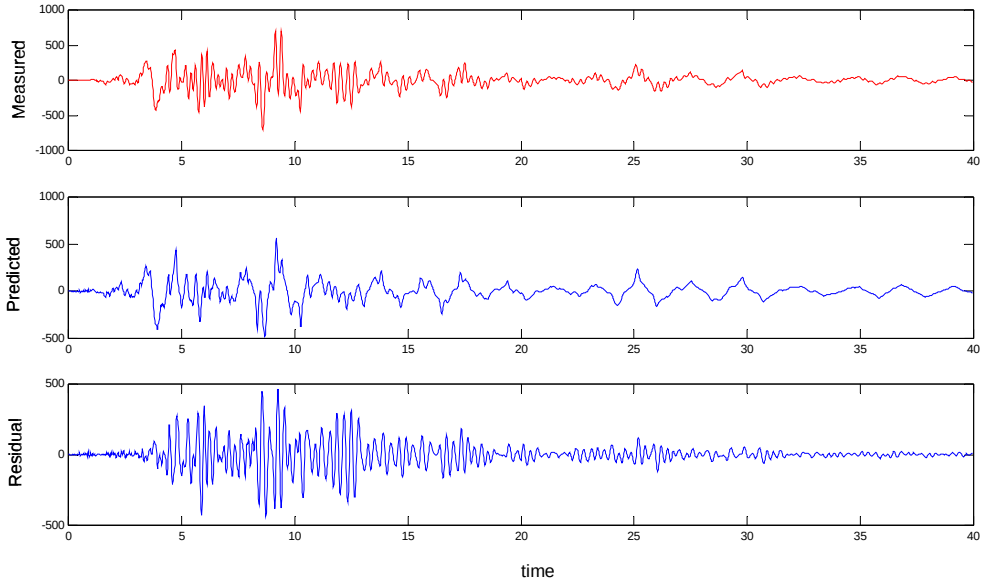


Fig. 9. Measured and PO model reference acceleration (cm/s$^2$) in channel 9 during the Northridge Earthquake

### *Other Buildings from the CSMIP Database*

The same procedure described previously has been applied to several other buildings of the CSMIP database and the results are, to the best knowledge of the writers, in agreement with the empirical observations from the field in all cases. Table1 presents results for five structures for which explicit post earthquake assessments have been reported [9,10].

Table 1. Summary of IAP results for 5 buildings taken from the CSMIP database

| Building | Earthquake used to formulate POM ---------- Earthquake investigated | PGA (PSA) In g's | η | κ | IAP |
|---|---|---|---|---|---|
| Sherman Oaks 13-story commercial building Station# 24322 Concrete | Whittier 1987 | 0.15 (0.17) | 0.03 | | |
| | Northridge 1994 | 0.46 (0.90) | 0.29 | 0.95 | Restricted Access |
| Van Nuys 7-story hotel Station# 24386 Concrete | Landers 1987 | 0.06 (0.19) | 0.02 | | |
| | Northridge 1994 | 0.47 (0.59) | 0.55 | 20.33 | Unsafe |
| Los Angeles 17-story residential building Station# 24601 Concrete | Landers 1992 | 0.05 (0.21) | 0.02 | | |
| | Northridge 1994 | 0.26 (0.58) | 0.03 | NA | Inspected |
| Burbank 6-story commercial building Station# 24370 Steel | Whittier 1987 | 0.05 (0.22) | 0.07 | | |
| | Northridge 1994 | 0.35 (0.49) | 0.59 | 0.30 | Restricted Access |
| Los Angeles 52-story Station# 24602 Steel | Landers 1992 | 0.05 (0.17) | 0.06 | | |
| | Northridge 1994 | 0.15 (0.41) | 0.14 | NA | Inspected |

## No Prior Earthquake Available to Formulate the POM

A situation that can arise in practice is that there is no excitation to formulate the PO model. The first thing that comes to mind for resolving this situation is to generate the maps using the early part of the records, before the motion is strong enough to induce nonlinear response or damage. This option was explored and it was concluded that the available duration is usually too short to ensure an accurate map. Another alternative, of course, is to use the late portion of the records, after the strong motion ceases, so the response can be once again assumed to be essentially linear – to distinguish this model from the standard situation we refer to it as the LPO model (where the L is reminiscent of late). Needless to say, if the structure has suffered permanent damage the reference map is then the one for the damaged system. For the purpose of identifying the impact of the motion on the building the information lost in trading the reference model at the start for the one that prevails at the end is not much regarding the computation of $\eta$ (the amount of nonlinearity) but the computation of $\kappa$ is no longer feasible (at least in the standard fashion) because the average slope after the strong motion ends will always be small.

One could think or reversing the process to use the slope at the early part of the record to get κ but robustness becomes a problem due to the short time intervals involved. At the present state of development, if there is no prior reference motion, we limit the IAP to differentiating between INSPECTED and OTHER.

To offer some quantitative insight into the accuracy that can be attained with a PO model based on the later portion of the record we consider again the Van Nuys building but assume that at the arrival of the Northridge earthquake no prior data was available to formulate a PO model. Fig.10 shows, in the same plot, the LPO model predictions and the measurement at channel #9. As expected, the model matches the later part of the response and shows that the strong part of the excitation was not governed by the same map. The value of η for the results in fig.10 (which is the channel with the largest residual) is 0.51 – which is in good agreement with the 0.55 that was obtained when the Landers earthquake was used to formulate the PO model.

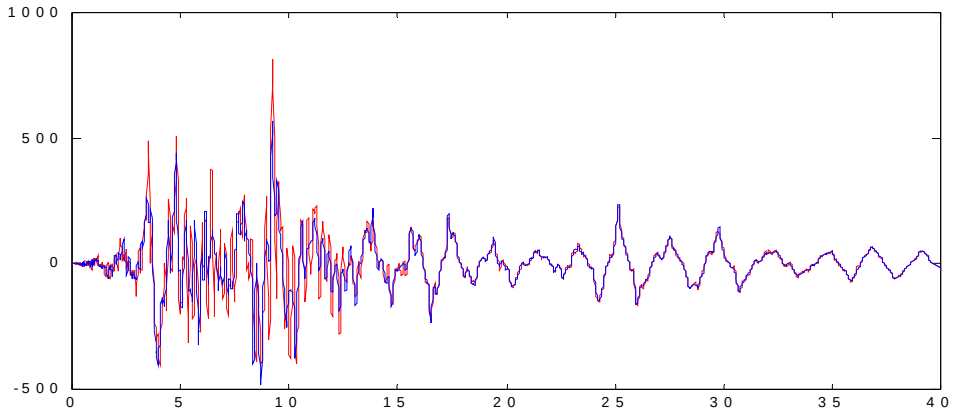


Fig.10. Comparison between measured (blue) and LPO model (red) in channel 9 (cm/sec$^2$) Northridge Earthquake

## Conclusions

The data driven approach to asses the impact of earthquakes presented here is based on a very simple concept, namely, if one has data from a non-damaging motion a map between the available channels for the healthy behavior can be established and this map can be used to determine the deviations from the reference in subsequent earthquakes. Needless to say, the key for success in this simple concept is connected with the ability to formulate an accurate map for realistic conditions. In this regard, a standard map operating in open loop proves to be less accurate than one would like, primarily because of SSI effects. One way to improve accuracy is by changing the open loop to an observer structure. The solution developed here, which has been designated as the Partial Observer model feeds the measured output channels that are not being predicted into the model that predicts the reference response. The lack of an autoregressive term ensures adequate sensitivity to nonlinearity.

One point that deserves explicit note and which was only briefly mentioned in the body is the fact that much of the robustness of the approach presented derives from the fact that the

technique avoids the nemesis of most identification based procedures, i.e, the need to distinguish between computational and system modes. Indeed, in the real situation one faces high order dynamics, noise in all the signals and the inevitable fact that the structure is not viscously damped and perfectly linear, even when there is no damage. All of these facts (and many others not noted for brevity) combine to make the separation of actual system modes from computational ones a difficult problem for which no entirely satisfactory solution has been yet devised. Nevertheless, because the computational modes have a small contribution to the output the PO model can be formulated without a need to worry about this (otherwise potentially critical) matter.

A related issue also worth noting is the fact that the technique presented is not only devoid of heuristics but is insensitive to complications from high modal density, interacting closely spaced modes and all the other issues that can arise if one attempts to translate the map between the channels into a modal-model characterization.

We conclude by noting that the approach uses *all the available data,* does not call on any priory knowledge about the structural system and operates in a fully automated fashion. This last feature is one that we insisted from the outset, not because it is essential for practicality, but because it ensures against the malady of "we can find it when we know where it is". Note that while the information from the residuals has been mapped to the ATC-20 posting, the residuals are rich in information and may allow a more refined classification, including perhaps indications on the localization of damage, if damage is identified.

## Acknowledgement

The work reported in this paper was carried out under the support of a grant from the California Strong Motion Instrumentation Program (CSMIP). This support is gratefully acknowledged.

## References

1. ATC, Procedures for Post earthquake Safety Evaluation of Buildings, 1989.

2. Naeim, F. "Seismic Performance of Extensively Instrumented Buildings an Interactive Information System", CSMIP. 1997

3.Chen, S J H. "System Identification and Damage Assessment of Existing Structures", PhD thesis, school of civil engineering , Purdue University, W. Lafayette , IN., 1980

4. Beck, J L "Determining Models of Structures from Earthquake Records", Report No EERL 78-01, California Institute of Technology, Pasadena, CA, 1978

5. Juang, J N "Applied System Identification", Prentice Hall, NJ, 1994.

6. Juan J., and Pappa, R. (1985). "An Eigensystem Realization Algorithm for Modal Parameter Identification and Model Reduction," Journal of Guidance and Control Dynamics, Vol.8, No.5, pp.610-627.

7. H. Van der Auweraer and B. Peters (2004). "Discriminating Critical Poles from Mathematical Poles in High Order Systems: Use and Automation of the Stabilization Diagram". IMTC 2004-Instrumentation and Measurement Technology Conference, 2004.

8. B. Peters , H. Van der Auweraer, P. Guillarme and J. Leuridan (2004). "The PolyMAX Frequency Domain Method: A New Standard for Modal Parameter Estimation". Shock and Vibration (11) 2004, pp. 395-409

9. Earthquake Spectra. "Northridge Earthquake Reconnaissance Report", April 1995, Vol. 2

10. F. Naeim (1998). "Performance of 20 Extensively Instrumented Buildings During the 1994 Northridge earthquake". Structural Design of Tall Buildings (7) pp. 179-194

# GROUND MOTIONS OF THE SUMATRA EARTHQUAKES OF 2004 AND 2005

Paul G. Somerville, Hong Kie Thio and Gene Ichinose

URS Corporation
566 El Dorado Street, Pasadena, CA 91101

## Abstract

The Sumatra earthquakes of December 26, 2004 (Mw 9.15) and March 28, 2005 (Mw 8.7) are the largest subduction earthquakes that have ever been recorded on modern digital instruments. Both earthquakes were caused by the subduction of the India–Australia plate beneath the Eurasian Plate. Although these earthquakes were not recorded on scale at close distances, they were recorded at regional distances. These regional recordings shown strong spatial variations in amplitude and duration that are consistent with rupture directivity effects. The duration of ground motion of the December event to the north in Thailand was about 600 seconds, while the duration in other directions, including Sumatra, was about 1,000 seconds.

## Earthquake Rupture Models

The December 26, 2004 and March 28, 2005 Sumatra earthquakes occurred on the interface between the India – Australia Plate and the Eurasian Plate. The December earthquake was the largest earthquake to occur anywhere in the world since the Mw 9.2 Alaska earthquake of 1964, and only one of four earthquakes of magnitude Mw 9.0 or larger in the past 100 years. The shallow part of the plate interface on which the earthquakes occurred lies offshore of northwestern Sumatra, and dips at an angle of about 11 degrees from the horizontal, down to the east.

Slip models that we derived using complete seismograms of the two earthquakes are shown in Figure 1 (Thio et al., 2005). The part of the interface that was ruptured by the earthquakes is about 200 km wide, and lies in the depth range of about 5 to 40 km. The rupture length of the December earthquake was about 1,200 km, extending from the epicenter, located about 250 km south of Banda Aceh, to the northern end of the Andaman Islands. The March earthquake had an epicenter located near that of the December earthquake, but it ruptured in the opposite direction for about 400 km to the southeast. The rupture dimensions of the two earthquakes are consistent with the scaling relations for subduction earthquakes developed by Somerville et al. (2002).

Analysis of teleseismic short period body waves of the December event by Ammon et al. (2005) showed that the source duration of the event was about 500 seconds, consistent with rupture propagation at 2.5 km/sec over a 1,200 km rupture length. The earthquake was followed by an aftershock sequence that spanned a zone that roughly coincides with the rupture zone shown in Figure 1, extending northward from the epicenter to the northern end of the Andaman Islands.

The slip involved sudden sliding of the India-Australia plate beneath the Eurasian plate. Before the earthquake, the interface between the two plates was locked, causing the India-Australia plate to drag the Eurasian plate downwards. The sudden rebound of

the Eurasian plate during the earthquake caused its western edge to spring upward. On the ocean floor at the edge of the Eurasian plate, the amount of this uplift was about 3 meters. This sudden uplift of the ocean floor generated a tsunami that propagated in all directions away from the source region of the earthquake. There was little geometrical spreading (reduction in wave amplitude) to the east and west of the source area, because the source was in effect a line source rather than a point source. The tsunami took about 20 minutes to reach the coast of northwestern Sumatra, and about 2 hours to reach the coasts of Thailand and Sri Lanka.

## Ground Motions

The earthquakes were not recorded on scale at close distances; the largest earthquake for which nearby strong motions have been recorded is still the Mw 8.4 Peru earthquake of 2001 (Somerville et al., 2003). The closest part of the earthquake rupture surface lies about 50 km off northwest Sumatra at a depth of about 40 km, so the closest distance from the earthquake source to the coast is about 65 km. Given the existence of damage to buildings in Aceh Province at the northwest end of Sumatra, it seems likely that the level of the ground shaking along the west coast of Aceh Province was about 25%g.

The recordings of the two earthquakes at station PSI in northern Sumatra, whose location is shown at the top of Figure 2, are clipped, but they give some idea of the duration of strong ground motion if not its peak amplitude. The time axes of all the ground motion velocity figures in this paper are demarcated at 100 second intervals. The recorded ground motions of the December event are shown at the top of Figure 3, and those of the March event are shown at the bottom of Figure 3. The December event had a duration of about 200 seconds above its clipping level of 1 cm/sec, and peak velocities remained close to 1 cm/sec for about 700 seconds, while the March event had a duration of about 150 seconds above this level, and then dropped well below that level. However, the peak velocities of the March event were evidently stronger than those of the December event, judging by the relative degree of clipping, consistent with the greater proximity of the PSI site to the rupture plane of the March event, as shown at the top of Figure 2.

Although the earthquakes were not recorded on scale at close distances, they were recorded at regional distances at the stations shown at the top of Figure 2. There are five recordings within about one source dimension of the earthquake, which by some definitions would make them “near source,” but that source dimension is very large, about 1,200 km. The recordings, shown at the bottom of Figure 2, have strong spatial variations in amplitude and duration that are consistent with directivity effects observed in the near source region of crustal earthquakes, but on a much larger time scale. Station CHTO in the forward rupture directivity direction to the north in Thailand has much larger ground motion amplitudes and shorter duration, about 600 seconds, than the other stations, which are located to the west in Sri Lanka (PALK), to the southeast in Java (UGM), and to the south on Cocos Island (COCO). Backward rupture directivity at these other stations caused the ground motion durations to be much longer, on the order of 1,000 seconds. We plan to use these recordings to model seismic wave propagation in the region, providing a basis for extrapolating the recorded seismic wave field to closer

distances, and estimating the strength of the ground motions throughout the region that experienced shaking damage.

The broadband peak ground velocities in Figures 2 and 3 contain very long period motions. Highpass filtering these velocity recordings at 5 seconds period results in the filtered ground velocities shown in Figure 4. The filtered peak velocities are reduced to about 0.4 cm/sec at station PSI (which is still influenced by clipping), and attenuate much more rapidly than the broadband peak velocities in Figure 3 at the more distant stations.

A preliminary intensity map of the December 26 Sumatra earthquake from the Amateur Seismology Centre in India is shown in Figure 5. Cassidy and others (2005) have updated this map using data from David Wald from the USGS website "did you feel it?" to give intensity values as high as MMI VIII in northwestern Aceh Province, consistent with damage to buildings in Banda Aceh and towns on the northwest coast of Sumatra.

## Acknowledgment

Our work on the Sumatra earthquakes was supported in part by Pacific Gas & Electric Company.

## References

Ammon, C.J., J. Chen, H.K. Thio, D. Robinson, S. Ni, V. Hjorleifsdottir, H. Kanamori, T. Lay, S. Das, D. Helmberger, G. Ichinose, J. Polet, D. Wald (2005). Rupture process of the great 2004 Sumatra-Andaman earthquake. Submitted to Science.

Cassidy, J.F., G.C. Rogers, H. Dragert, and K. Wang (2005). The 26 December 2004, M 9.0 Sumatra earthquake: implications for Cascadia. Seismological Research Letters 76, 220.

Petersen, M.D, J. Dewey, S. Hartzell, C. Mueller, S. Harmsen, A. Frankel and K. Rukstales (2004). Probabilistic seismic hazard analysis for Sumatra, Indonesia and across the Southern Malaysian Peninsula. Tectonophysics 390, 141-158.

Somerville, P.G., H.K. Thio, G, Ichinose, N. Collins, A. Pitarka, and R.Graves (2003). Earthquake source and ground motion characteristics of the June 23, 2001 $M_w$ 8.4 Arequipa, Peru, earthquake. SRL 74, 223.

Somerville, P.G., T. Sato, T. Ishii, N.F. Collins, K. Dan and H. Fujiwara (2002). Characterizing heterogeneous slip models for large subduction earthquakes for strong ground motion prediction. Proceedings of the Architectural Institute of Japan.

Thio, H.K., G. Ichinose, P. Somerville and J. Polet (2005). Source process and tsunami generation of the 2004 Sumatra-Andaman earthquake. Proceedings of the Second Annual Meeting of the Asia-Oceania Geosciences Society, Singapore, June 20-24.

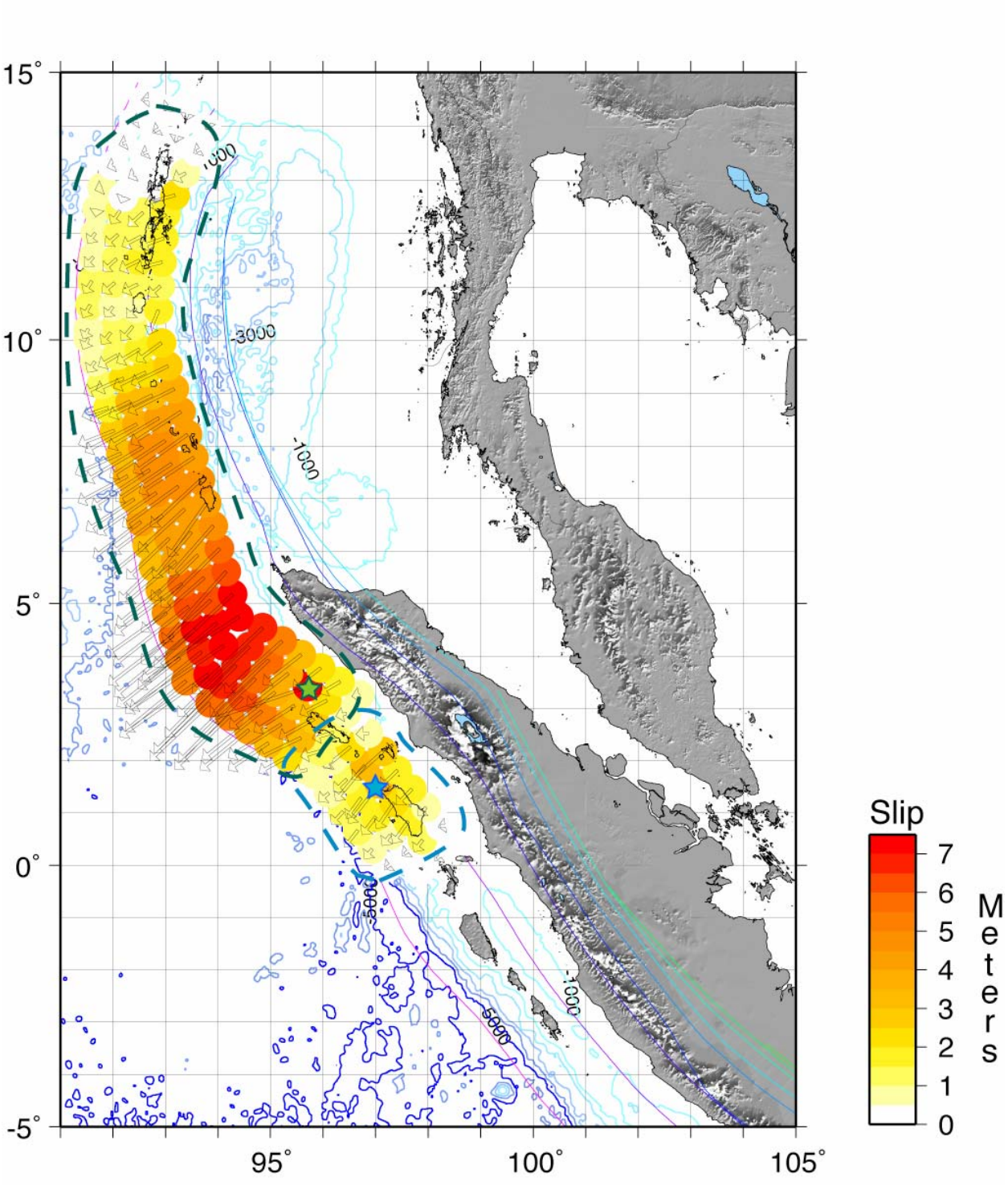


Figure 1. Slip maps of the December 26, 2004 and March 28, 2005 Sumatra earthquakes, with epicenters shown by stars.

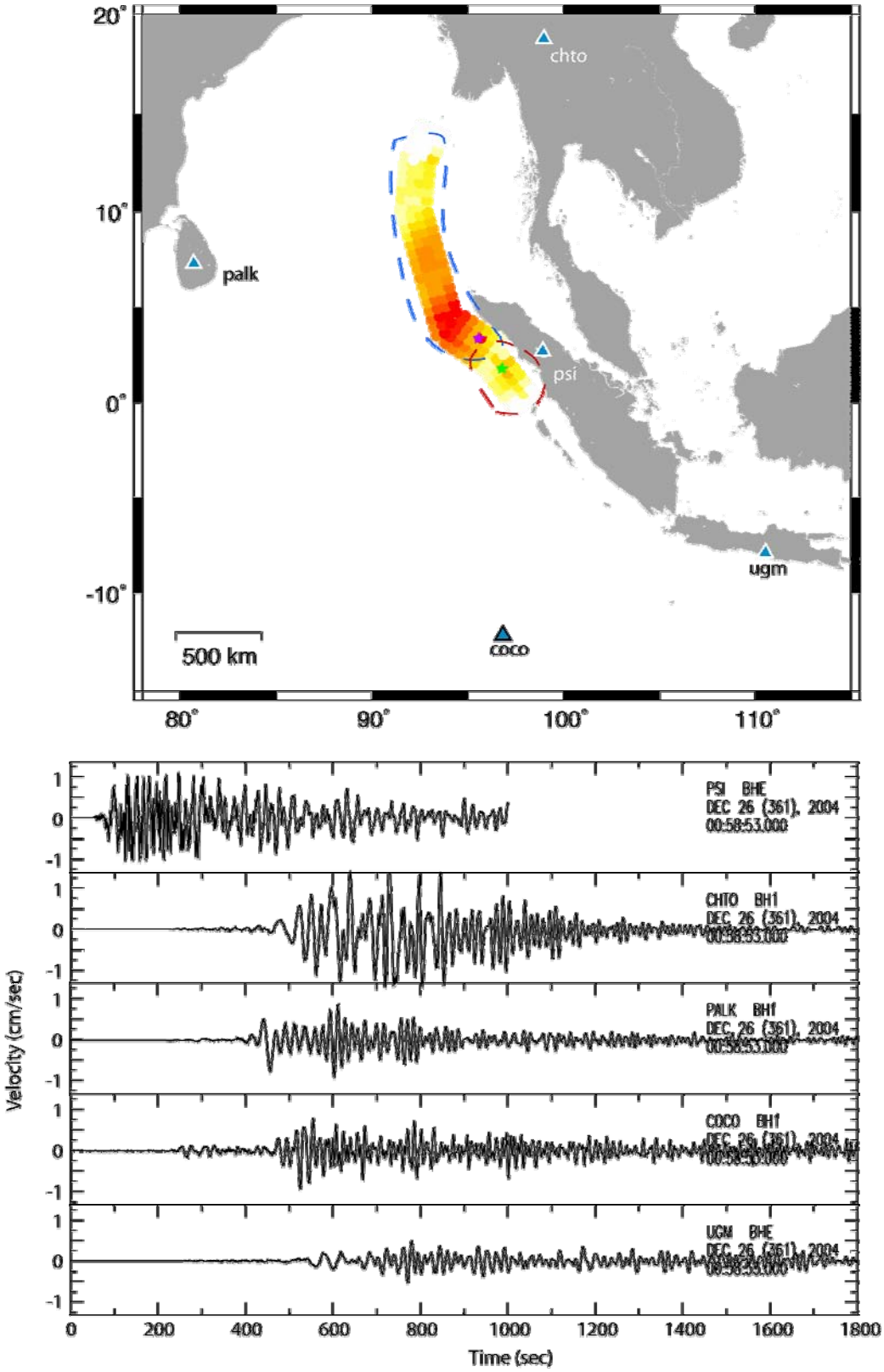


Figure 2. Top: Map of the region around Sumatra showing the slip maps of the December and March earthquakes (epicenters shown as stars), and regional seismic stations. Bottom: Broadband velocity seismograms of the December 26, 2004 earthquake recorded at the regional stations.

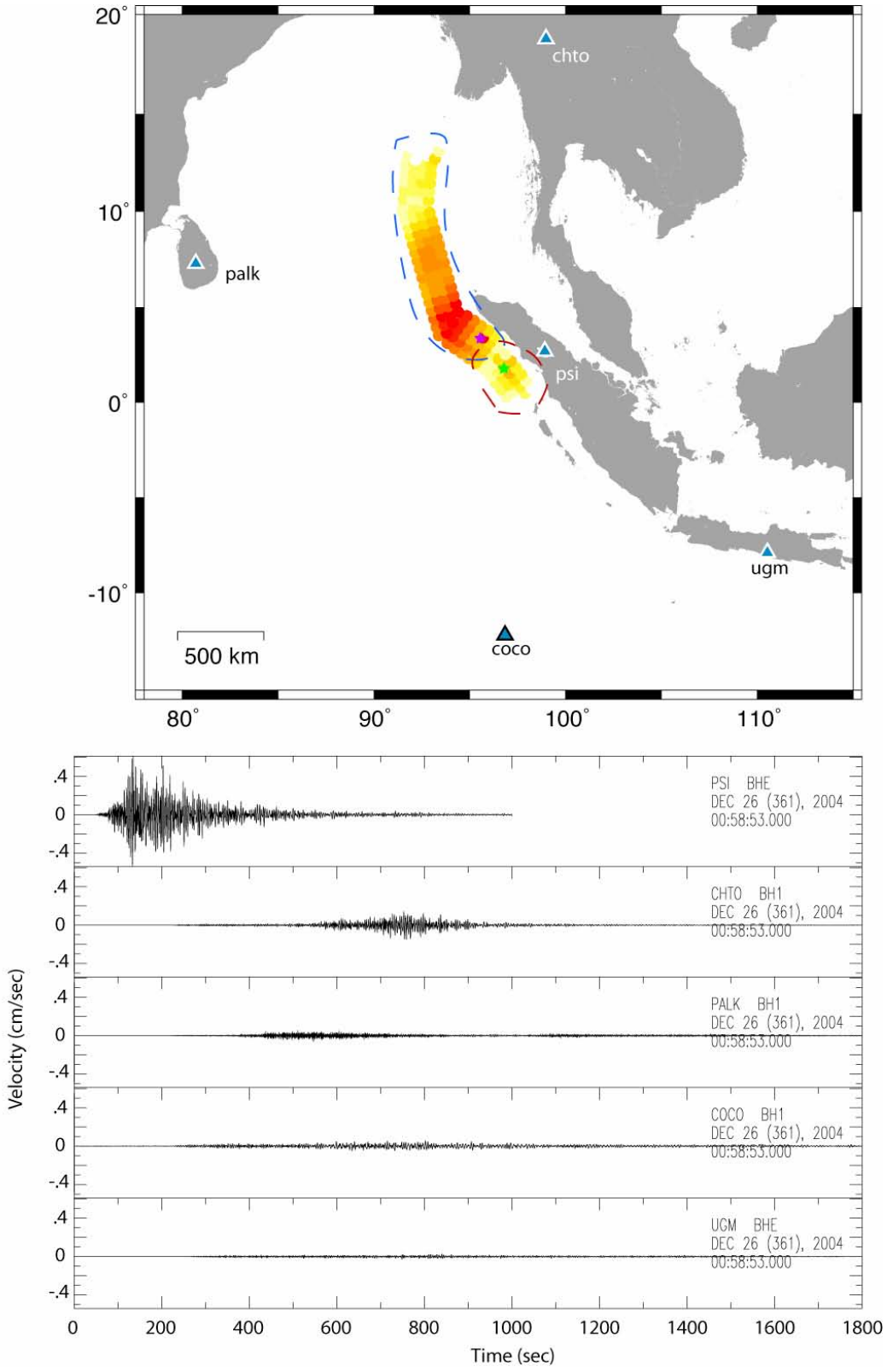


Figure 3. Top: Map of the region around Sumatra showing the slip maps of the December and March earthquakes (epicenters shown as stars), and regional seismic stations. Bottom: Velocity seismograms of the December 26, 2004 earthquake recorded at the regional stations high-pass filtered at 5 seconds.

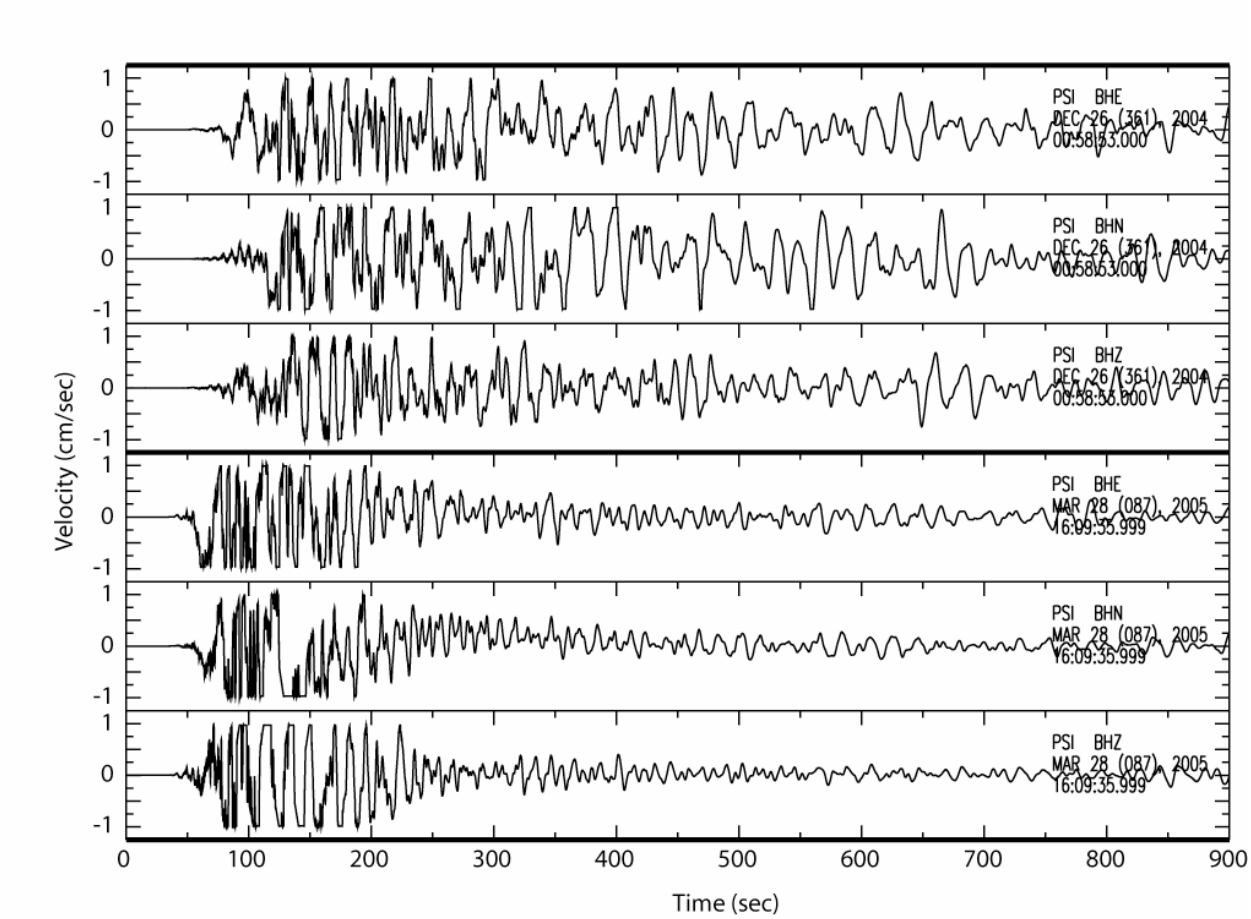


Figure 4. Recordings of the December 26, 2004 (top) and March 28, 2005 (bottom) Sumatra earthquakes at station PSI in northern Sumatra, approximately 350 and 250 km away, respectively.

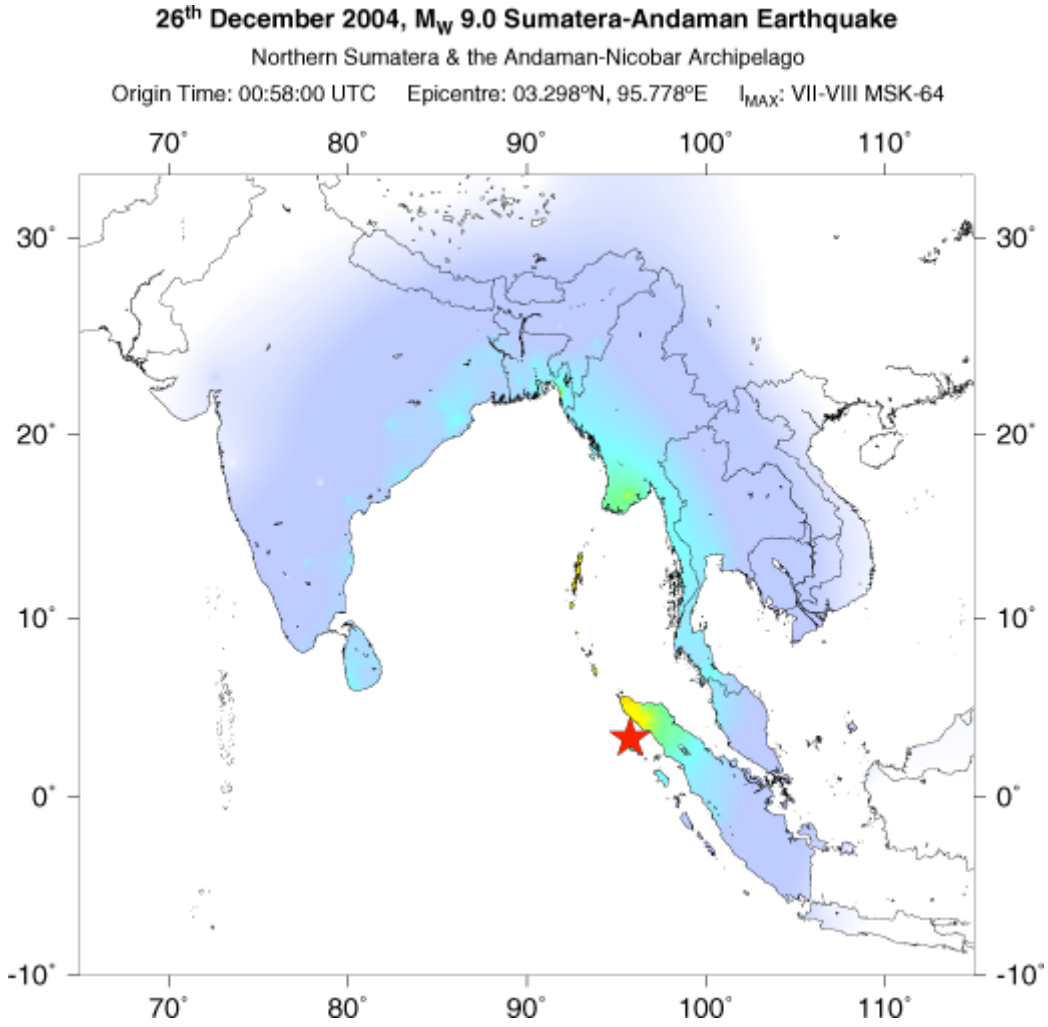


Figure 5. Intensity map of the December 26, 2004 Sumatra earthquake.

Source: Amateur Seismology Center of India, http://asc-india.org/INT/20041226.htm

# SEISMIC RETROFIT AND INSTRUMENTATION OF LOS ANGELES CITY HALL

Nabih Youssef and Owen Hata

Nabih Youssef & Associates**,** *Structural Engineers*
Los Angeles

## Introduction

The construction for the seismic rehabilitation of the Los Angeles City Hall was completed in 2001. An integral part of the project is the installation of seismic instrumentation throughout the building. The instrumentation program was a collaborative effort involving the Los Angeles City Department of Public Works Bureau of Engineering, California Geologic Services Strong Motion Instrumentation Program (CGS-SMIP) and the Engineering Design team. The future data recorded by these sensors will provide valuable insight on the actual response of the building during an earthquake. This information will aid the structural engineering community to better understand the behavior of base isolated structures with supplemental damping.

The building was originally constructed in 1926 and was the first building to exceed the 150 feet height limitation for all privately constructed buildings in Los Angeles. It is 32 stories (460 feet) tall. The original building was designed prior to the enactment of explicit seismic design requirements and therefore, was not specifically designed to resist earthquake generated forces.

Over the past 75 years, regional earthquakes have caused damage to the building. Terra cotta cladding has been cracked, broken or destroyed in portions of the building's exterior. With every significant earthquake, unanchored masonry debris has been scattered about the building's interior. Large cracks in the masonry walls appeared at the 24th floor after the 1971 Sylmar Earthquake, the 1987 Whittier Earthquake and the 1994 Northridge Earthquake.

The building has been seismically rehabilitated in order to preserve life safety, mitigate damage, maintain the integrity of the building's exterior facade, and protect the historic interior fabric from damage. Base isolation with supplemental damping was used to enhance its seismic performance. This approach was determined to be the most effective strengthening scheme based on performance and cost.

This paper presents an overview of the rehabilitation project including the development of seismic performance goals, identification of inherent seismic deficiencies of the original building, description of the final seismic strengthening and instrumentation program.

## Building Description

The Los Angeles City Hall has three major structural portions: “podium” (sub-basement to second floor), “mid-rise” (third to ninth floor) and “tower” (tenth floor to the top of the dome).

The structural frame of the tower extends through the mid-rise and podium of the building to the mat-slab foundation. Similarly, the mid-rise frame extends through the podium to the foundation level *(See Figure 1)*.

The gravity system of the building consists of a concrete encased steel frame and reinforced concrete slab/pan-joist floor system. The typical beam-to-column connection is a riveted 'wind connection' that utilizes top and bottom seat angles *(See Figure 2)*.

The building was originally designed prior to the enactment of explicit seismic design requirements and therefore, was not specifically designed to resist seismic forces. Thus, the original building did not have a distinct seismic force resisting system that provided a competent load path for seismic loads. However, there were a number of structural components that, although not specifically designed to resist earthquake forces, participated in resisting these forces.

Lateral load resistance was provided by horizontal diaphragms, perforated unreinforced masonry infill walls, lightly reinforced concrete walls and light steel bracing. The unreinforced masonry infill walls provided most of the lateral force resisting capability of the original building.

## Performance Criteria

Seismic performance objectives were established for the project. These objectives, as outlined below, were intended to satisfy both the life safety and damage mitigation objectives of the City of Los Angeles for the building.

1. Insure stability of the structural system during the maximum possible earthquake.

2. Prevent falling hazards which pose a significant life safety hazard.

3. Insure safe means of egress from the building.

4. Insure that life safety systems remain operable.

5. Maintain integrity of the building's exterior façade *(See Figure 3)*.

6. Protect historic interior fabric of the building from damage *(See Figure 4)*.

7. Protect emergency telecommunication systems including tower, satellite dishes, etc.

8. Preserve the basic functions of the building.

These objectives were quantified in engineering criteria to facilitate the evaluation of the seismic performance of the original building. The engineering criteria define the performance objectives in terms of specific analytical limit states. These limit states were determined using

the latest research data available regarding the seismic performance of existing buildings combined with guidelines developed for life safety protection and damage mitigation.

Limit states were established for inter-story drift, inelastic demand ratios for the various structural elements, and story accelerations. Inter-story drift limits are essential to maintaining global stability in the structural system by limiting the P-Δ effects. In addition, earthquake damage in many structural and non-structural building systems can be directly associated to the inter-story drift the building experiences. Inelastic demand ratios (IDR) represent a measure of the post-yield deformations of the structural members during a given earthquake. In order to insure the safety and stability of the structural system, limitations on the allowable inelastic demand ratios are required. Story accelerations affect the seismic performance of building contents and non-structural systems.

## Material and Dynamic Testing

Material and dynamic testing were performed to determine the strength and deformation characteristics of the original building materials and to determine the dynamic characteristics of the building.

Ambient and forced vibration tests were performed to determine the dynamic properties of the original building. The ambient vibration test measured the response of the building to vibrations which occur at the building site, such as vehicle traffic, wind, occupants, etc. Forced vibration tests were performed using a forced vibration oscillator to vibrate the building. The forced vibration test was used to determine the response of the building to high level excitations *(See Figure 5).* The results of these tests were used to verify the modeling assumptions made in the development of the computer model of the original building.

A variety of in-situ tests were performed on the unreinforced masonry. In-plane shear tests were performed on the masonry walls to determine the ability of the existing brick and mortar to resist shear stresses. Several flatjack tests were performed to determine the compressive strength and deformability properties of masonry *(See Figure 6).* The results of these tests were used in the development of computer models and in the determination of the strength capacity of the original building.

## Computer Models

Computer models were developed to assess the global performance of the original and rehabilitated buildings. Nonlinear finite element models were developed to determine the limit state behavior of the unreinforced masonry infill. Computer models were also developed to perform nonlinear dynamic analysis for the base isolated building.

The primary steel frame skeleton, steel bracing, reinforced concrete walls, unreinforced masonry infill walls, and concrete diaphragms were included in the linear elastic computer models to accurately simulate the behavior of the original building *(See Figure 7).* In order to assess the dynamic behavior of the building, it was crucial to understand the behavior of the existing unreinforced masonry walls. These walls represent a significant portion of the overall

strength and stiffness of the original structural system. Nonlinear finite element analysis was performed on typical URM wall configurations of the building to determine their limit state behavior. Results from these analyses were incorporated into the global model of the building. The global model of the original building was then calibrated to the results of the vibration tests. Table 1 below summarizes the measured and eigen-analysis periods.

| Mode Number | Direction | Period (sec) | | | |
|---|---|---|---|---|---|
| | | Ambient | Forced | ETABS | SAP90 |
| 1 | East-West | 2.38 | 2.50 | 2.62 | 2.78 |
| 2 | North-South | 2.08 | 2.27 | 2.44 | 2.52 |
| 3 | Torsion | 1.08 | 1.19 | 1.24 | 1.39 |

**Table 1. Periods of Vibration - Original Building**

## Evaluation of Original Building

The seismic performance of the original was evaluated and deficiencies in the lateral force resisting system were identified. The computer model of the original building was verified by performing an eigen-analysis and comparing the results with the test data obtained from dynamic testing of the building. The periods obtained from the eigen-analysis were found to be in good agreement with the results of forced vibration tests.

The seismic performance of the original building was evaluated using linear dynamic analysis procedures. The design basis earthquake, representing a 10% probability of being exceeded in a 50 year time period was used.

The results of the analyses indicated high stress levels in the unreinforced masonry walls, relatively large inter-story drifts and story accelerations in the tower. Significant damage to the unreinforced masonry walls, terra cotta, partition walls, historic fabrics and all rigid/brittle non-structural systems would be expected. The original building did not satisfy the seismic life safety criteria established for the project and required strengthening.

## Enhancement of Seismic Response

The building has been strengthened using base isolation with reinforced concrete shear walls and supplemental damping. Base isolation effectively decouples the building from ground motions, greatly reducing the level of seismic force transferred to the super-structure. The new reinforced concrete shear walls add strength, re-distribute seismic over-turning forces, stiffen the super-structure increasing the effectiveness of the isolation system, and improve the lateral force load path. The viscous dampers have been installed at the plane of isolation and between the $26^{th}$ and $27^{th}$ floors. The dampers at the plane of isolation increase the energy dissipation capacity of the isolation system and thus, reduce the energy transmitted to the super-structure. The dampers in the tower add damping to the higher modes of the building response and have the localized

effect of reducing whiplash at the top of the tower.

This approach to strengthen the building significantly reduces the accelerations, inter-story drifts and element stress levels throughout the height of the building.

**Isolation System**

The plane of isolation is located below the basement level and above the foundation. The isolation system consists of 416 high damping rubber (HDR) bearings, varying in size from 29.5 in. to 51.2 in. diameter, and 90 flat sliding bearings. The HDR bearings vary in height from 9.6 inches to 16.6 inches. *(See Figure 8)* The sliding bearings are comprised of a teflon pad mounted on a natural rubber bearing, and a stainless steel sliding plate. The sliding bearings support less than 10% of the total building weight.

The bearings were installed using a loose-bolt connection to allow uplift to occur without loading the bearing in tension.

The bearings were rigorously tested to verify their properties used in the analysis and design. Bearing stability at a maximum lateral displacement of 21 inches was also verified *(See Figure 9).*

**Supplemental Damping**

The isolation system is supplemented with 52 viscous dampers, 26 in each direction, at the plane of isolation. These dampers bridge the plane of isolation, i.e. one end is connected to the foundation and the other to the underside of the basement slab. The dampers have a mid-stroke length of 143 inches, a force rated capacity of 300 kips at 50 in/sec, and a stroke of ±21 inches *(See Figure 10).*

Twelve viscous dampers, six in each direction, have been installed between the 26$^{th}$ and 27$^{th}$ floor. These dampers have a force rated capacity of 225 kips at 10 in/sec, a stroke of ±4 inches, and a mid-stroke length of 46 inches *(See Figure 11).*

Full-scale prototype 225 kip dampers were cyclic load and drop tested to verify the damper properties in the prototype test phase. The results from the cyclic load and drop tests were well correlated.

**Structural Strengthening**

The new walls are located along the perimeter walls of the tower extending to the basement and along the walls at the north and south ends of the mid-rise extending to the basement. The walls under the tower re-distribute the seismic over-turning forces and reduce the net uplift experienced by the isolators under the walls *(See Figures 12 and 13).*

The original basement diaphragm was demolished and a new 8 inch thick concrete diaphragm constructed. Demolition of the original diaphragm provided access to the foundation

and simplified the installation of the isolators. The new diaphragm system ties all of the isolators together and ensures proper force transfer between the super-structure and isolation system *(See Figure 14)*.

A new horizontal steel truss diaphragm was added at the roof of the mid-rise to facilitate the transfer of seismic forces from the tower to the new RC walls at the north and south ends of the mid-rise. This diaphragm couples the new tower walls to end walls of the mid-rise providing an additional load path for seismic forces and reduces the over-turning demand at the base of the tower *(See Figure 15)*.

Extensive work was done on the original foundation system to strengthen and tie individual footings together.

**Constructability**

The new 24 inch thick concrete walls at the basement level facilitated the installation of the HDR bearings located under these walls. Dowels were provided to transfer gravity loads from the column to the walls. After construction of these walls, the pedestals of the columns were removed. The gravity loads were transferred to the shear walls through the dowels. The bearings were then installed under the columns. A horizontal saw cut was then made in each wall at the basement level, to separate the wall from its foundation. The loads were then transferred back to the columns and bearings. This sequence of construction reduced installation time considerably.

## Instrumentation (Installed and Maintained by CGS-SMIP)

The utility and need of strong motion data has grown over the years with advances in technology that allow real-time retrieval and processing of data, advances in geological information systems (GIS) and loss estimation methods. The introduction of shake-maps on-line that demarcate ground shaking intensity in affected areas immediately after an earthquake has proved a useful tool to emergency response personnel. These maps are produced using data recorded by sensors located in the affected area in the immediate aftermath of the earthquake. The growing interest in loss estimation and the release of the HAZUS software (funded by FEMA) for use by government agencies, has increased the need for data correlating building damage to ground shaking intensity. These developments have broadened the stakeholder base (engineers and earth scientists) for strong motion instrumentation programs to include government agencies, utilities and insurers, and demonstrate the value of these programs.

An instrumentation program for the building has been developed to comply with the base isolation system design provisions of the Uniform Building Code. The principal objective of this program is to further the understanding of the behavior of the building during a seismic event and to use this knowledge to improve future design and construction practice. The data recorded from these sensors will allow the engineering community to calibrate analytical models and assumptions that were used in the analysis and design of the rehabilitated building. This knowledge will enhance our understanding of how isolation systems, viscous dampers and URM infill behave under seismic loading.

In order to achieve the stated objective, an adequate amount of data needs to be recorded in order to reconstruct the actual response in sufficient detail to compare with the response from analytical models. More robust data also allows the use of system identification techniques to determine dynamic characteristics of the building (periods, mode shapes, damping, etc.). Thirty sensors have been installed throughout the building by CGS-SMIP in conjunction with the City of Los Angeles Bureau of Engineering in December of 2003. This array of sensors significantly exceeds the code requirement of "*horizontal displacement recording devices … installed at the isolation interface*" and represents the "ideal extensive instrumentation scheme".

There are a total of 27 accelerometers and 3 displacement sensors. The accelerometers are distributed throughout the building with 5 sensors at the foundation (below the plane of isolation), 7 at the basement diaphragm (immediately above the plane of isolation), 4 at the 5$^{th}$ and 10$^{th}$ floors, 3 at the 26$^{th}$ floor, and 2 at the 27$^{th}$ and 29$^{th}$ floors *(See Figure 16)*. These locations were selected to optimize the value of the recorded data using the least sensors. The sensors at the foundation and basement levels provide response information above and below the plane of isolation. The sensors at the 5$^{th}$ and 10$^{th}$ floors are located at levels where major transitions (setbacks) in the building configuration occur. The sensors at the upper levels of the tower will provide data on the whiplash effect of the tower and the effectiveness of the viscous dampers at the 26$^{th}$ floor. All of the displacement sensors are located at the plane of isolation. The accelerometers and displacement sensors are also distributed in plan to capture any torsional response at each instrumented floor.

The sensors at the foundation and basement levels were judiciously located near isolators and dampers. Recorded data from these sensors will allow the study of the building response and the behavior of the isolators and dampers *(See Figure 17)*. Sensors that measure vertical motion are located above and below an isolator near the center of the building *(See Figure 18)*. Data from these sensors will provide information on the vertical response of the building and overturning/uplift.

Free field sensors will be installed in the park outside the building in the near future. Soil-structure interaction effects for the building may be investigated using the data recorded at the free-field and foundation.

In the future these sensors may be incorporated into a real time monitoring network that has the ability to detect damage to the building during an earthquake.

## Conclusion

The original Los Angeles City Hall has sustained damage from earthquakes over the past 75 years. In an effort to preserve life safety and mitigate damage, the building was seismically upgraded using base isolation with supplemental damping. This approach was determined to be the most effective strengthening scheme based on performance and cost. Construction was completed in 2001.

As part of the upgrade, seismic instrumentation has been installed throughout the building. The data recorded by these sensors in the future will provide valuable insight on the actual response of the building during an earthquake. This information will aid the structural engineering community to better understand the behavior of base isolated structures with supplemental damping.

**Figure 1: Aerial view of building**

**Figure 2: Historic view of building**

**Figure 3: Courtyard colonnade**

**Figure 4: Rotunda**

**Figure 5: Forced vibration oscillator setup**

**Figure 6: URM in-stu test setup**

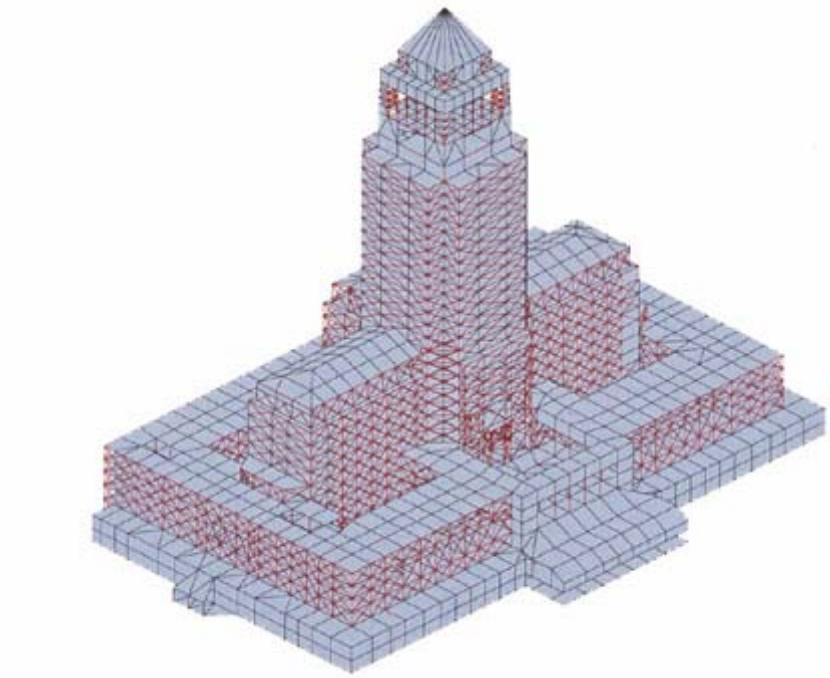

**Figure 7: Plot of 3D computer model**


**Figure 8: High damping rubber bearings installed under tower wall**

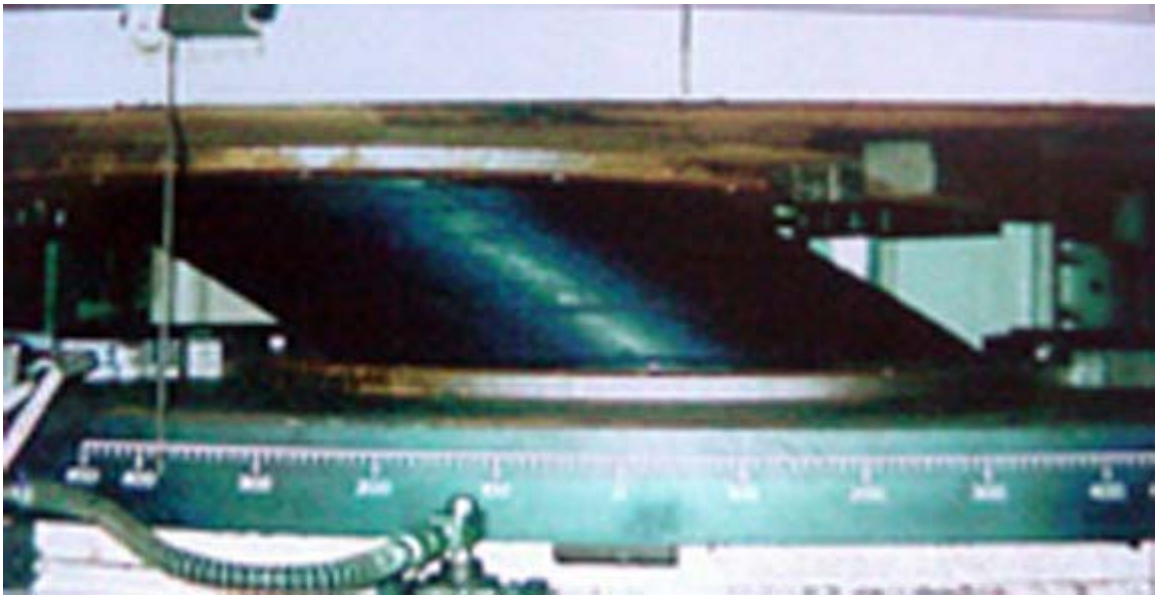

**Figure 9: Shear displacement test of bearing**

**Figure 10: 300 kip damper installed at plane of isolation**

**Figure 11: 225 kip damper installed at 26th floor**

**Figure 12: Rebar for new concrete shear wall at basement level**

**Figure 13: Rebar for new concrete shear wall in tower**

**Figure 14: New basement diaphragm in construction**

**Figure 15: New horizontal steel truss diaphragm at 11th floor**

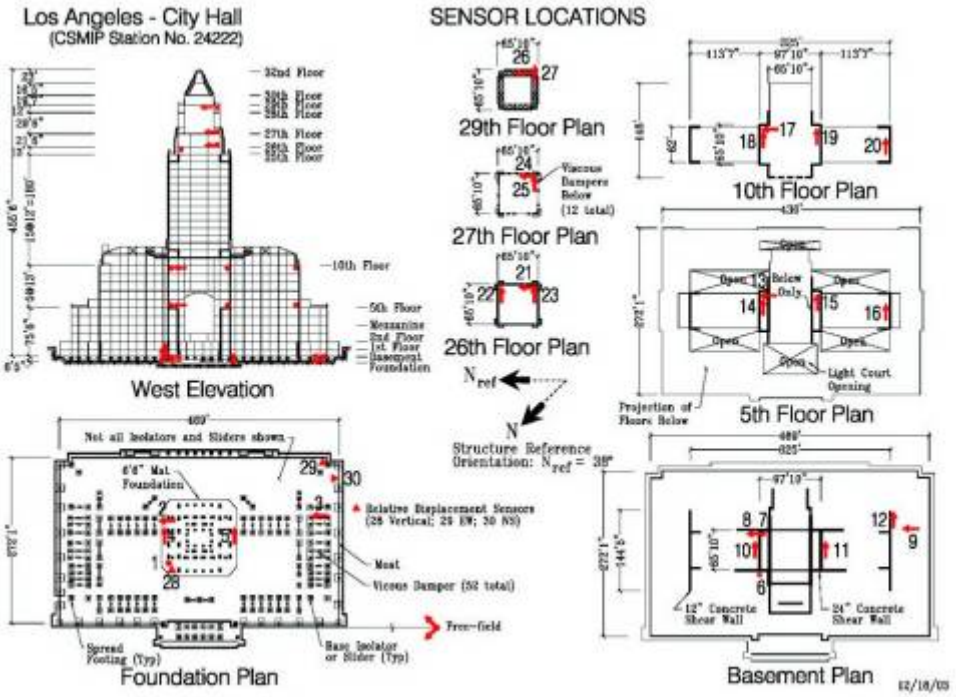


**Figure 16: Sensor layout (from CGS/CSMIP)**

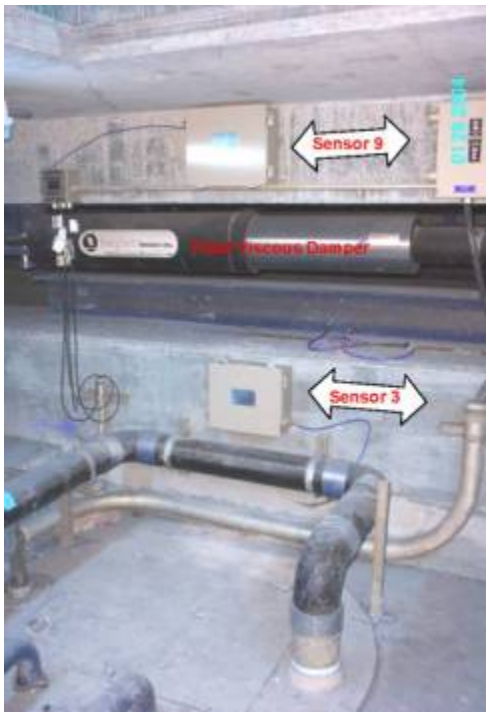


**Figure 17: Sensors installed above and below damper at plane of isolation (from CGS/CSMIP)**

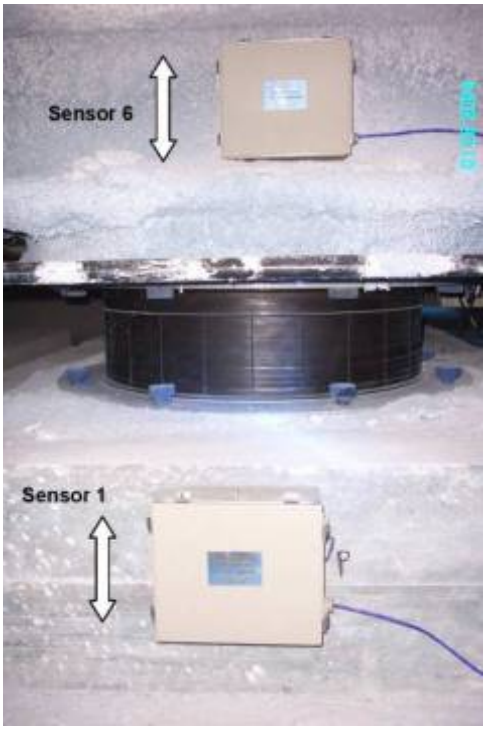


**Figure 18: Sensors installed above and below isolator at plane of isolation (from CGS/CSMIP)**